

**UNIVERSITY OF SALAMANCA**

Instituto de Física Fundamental y Matemáticas  
**Laboratorio de Radiaciones Ionizantes**

**SALSA: A CHARACTERIZATION SYSTEM OF  
THE ELECTRICAL RESPONSE OF HIGH  
PURITY GERMANIUM SEGMENTED  
DETECTORS BASED ON A HIGH  
RESOLUTION  $\gamma$  CAMERA**

PhD Document

Articles Compilation

**ÁLVARO HERNÁNDEZ PRIETO**

Supervisor: Dra. Begoña Quintana Arnés

Salamanca, 2016



---

## Abstract

One of the main goals in modern Nuclear Physics is the comprehension of the structure of the nucleus based on the fact that they are many-body systems. The study of the structure of the nucleus is made by measuring the  $\gamma$  radiation emitted during the decay of excited states. In this task, the  $\gamma$ -ray spectroscopy plays a fundamental role, given that its sensibility determines how far one can go in the detection of low probability nuclear transitions. The  $\gamma$ -ray spectrometers have been evolved during last years in parallel with new nuclear facilities which permits, with the new type of radioactive beams, to reach the farther regions in the nuclei chart. The most relevant examples of such a facilities can be found at FAIR (Darmstadt, Germany) [1], HIE-ISOLDE (CERN, Switzerland) [2], SPIRAL2 (Caen, France) [3] and SPES (Legnaro, Italy) [4]. As said before, the requirements of these new facilities have motivated the development of  $\gamma$ -ray spectrometers more a more complex and, together with them, all the associated software and tooling needed for their correct behaviour. In the last few years a new achievement has arrived with the  $\gamma$ -ray segmented detectors, allowing the  $\gamma$ -ray tracking within them. This technology has allowed to reduce the background of the measurements, increasing the peak-to-total and, therefore, the efficiency. The flagship of this technology is AGATA, *Advanced GAMMA Tracking Array*. This collaboration constitutes the framework of this thesis work. In such a  $\gamma$  spectroscopy systems it is critical the database which owns the relationship between the electrical response of the germanium crystal as a function of the  $\gamma$ -ray interaction position within it. In order to obtain these databases there are two different methods: the first one is based on Monte Carlo Simulations. In this methods the relation between  $\gamma$ -ray interaction position and crystal response is obtained by solving the Poisson equation all around the crystal volume. In order to simplify and speed-up the calculation, the volume of the crystal is divided in voxels. The accuracy of this method is, therefore, strongly dependent on this fact. In this method the same database is used for different crystals, missing the fact that the technique used to grow-up the Ge crystals make them all different one to each other [5]. The second method to get the database which relates  $\gamma$ -ray interaction position with electrical response in Ge crystal is experimental. It utilizes 3D characterization systems where each Ge crystal is individually characterized. Therefore, the obtained database will contain the real electrical response for each crystal, taking into account its individual characteristics.

The thesis work presented in this document is focus on the development of an experimental characterization system for High-Purity Germanium (HPGe) segmented detectors, specially optimized for AGATA detectors. The main goal is to obtain the electrical response as a function of the  $\gamma$ -ray interaction position within its active volume. In order to obtain the  $\gamma$ -ray interaction position we use a high spatial resolution  $\gamma$  camera as it will be explained. This document is a compilation of the

published works during all the thesis period. Papers were published following the work flow during the work and, therefore, they will explain the sequence of events starting from the study devoted to select the best materials for all the elements of the characterization system, following by development, construction and commissioning of our characterization system: SALSA, *Salamanca Lyso-based Scanning Array* and, finally, the validation of SALSA with the first HPGe detector characterization.

# Contents

---

List of Tables	V
List of Figures	VII
<b>1 Introduction</b>	<b>1</b>
1.1 $\gamma$ -tracking: The new Spectroscopy . . . . .	1
1.1.1 Requirements for the new generation of $\gamma$ -ray detectors. . . . .	1
1.1.2 The $\gamma$ -ray tracking concept . . . . .	1
1.1.3 Tracking detectors: characteristics and requirements. . . . .	2
1.1.4 Signal formation in HPGe detectors. . . . .	4
1.1.5 Pulse shape analysis for interaction position determination. . . . .	9
1.2 Experimental characterization systems of the electrical response: state of the art. . . . .	13
1.2.1 Mechanical systems. . . . .	13
1.2.2 Active collimation systems. . . . .	15
<b>Bibliography</b>	<b>19</b>
<b>2 Proceedings. Towards a high resolution <math>\gamma</math> camera.</b>	<b>21</b>
<b>3 Article 1. Characterization of a High Spatial Resolution <math>\gamma</math> Camera   for Scanning HPGe Segmented Detectors</b>	<b>33</b>
<b>4 Article 2. Study of accuracy in the position determination with   SALSA, a <math>\gamma</math>-scanning system for the characterization of segmented   HPGe detectors</b>	<b>43</b>



# List of Tables

---

1.1	AGATA technical specifications. . . . .	7
-----	---	---



# List of Figures

---

1.1	Cross section of $\gamma$ radiation in Ge. (Source: <i>Nist-XCOM: Photon Cross Sections Database</i> ). . . . .	2
1.2	Planar HPGe detector configuration (left) and coaxial (right). . . . .	4
1.3	HPGe detector (left) and the equivalent circuit (right). . . . .	5
1.4	The $4\pi$ set-up of AGATA (left) and one of its capsules with the 36 segments plus the central core (right). . . . .	8
1.5	Pre-amplifiers output for a single event in an AGATA crystal. The segment where the $\gamma$ ray has interacted is indicated in red. Green segments are those where the induced signal is presented. . . . .	9
1.6	Data flow diagram in MGS. . . . .	11
1.7	Potential surfaces and electric field lines in a ZX plane for an AGATA crystal given by MGS. The results show, as expected, how the electric field decreases with the radius from the central anode. . . . .	12
1.8	Drift velocities in electrons and holes (ZX plane) in an AGATA crystal. . . . .	13
1.9	Schematics of the Liverpool's scanning system with an AGATA crystal in place. The red star shows an example of a valid event: The $\gamma$ ray has a Compton scattering of $90^\circ$ in the AGATA crystal and then it is detected by one of the surrounding auxiliary detectors. . . . .	14
1.10	AGATA crystal in place to be scanned with the GSI scanning system. . . . .	16
1.11	AGATA crystal in place to be scanned with the IPHC scanning system. . . . .	17



---

## Chapter 1

# Introduction

---

## 1.1 $\gamma$ -tracking: The new Spectroscopy

### 1.1.1 Requirements for the new generation of $\gamma$ -ray detectors.

The new technology of segmented detector allows to detect the  $\gamma$ -ray emissions coming from decay of very unstable nucleus. From these decays one can expect very low counting rates for the target energies. This is the motivation to develop and optimize new  $\gamma$ -ray detectors with high peak-efficiency, keeping the good energy resolution and peak-to-total, at least comparable with the old systems based on passive anti-Compton systems.

### 1.1.2 The $\gamma$ -ray tracking concept

The  $\gamma$ -ray tracking applied to HPGe segmented detectors consists on the tracking of the path of the  $\gamma$ -rays inside the crystal. This is possible thanks to the contact segmentation which allows to collect the generated charged when the photon hits the semiconductor volume, depositing its energy. The different types of interaction between the radiation and matter and their probability as a function of the photon energy are presented in Figure 1.1. The  $\gamma$ -ray tracking is based on the scattering Compton, which is the main process in the energy region of interest in spectroscopy, except below 100 keV.

In a Compton scattering, the  $\gamma$ -ray energy before  $E_\gamma$  and after  $E'_\gamma$  the interaction, together with the scattering angle  $\theta$ , defined with respect to the incident  $\gamma$ -ray direction, are all related under the Compton formula:

$$E'_\gamma = \frac{E_\gamma}{1 + \frac{E_\gamma}{m_0c^2}(1 - \cos\theta)}. \quad (1.1)$$

Knowing the energies (before and after) and the interaction positions, it is pos-

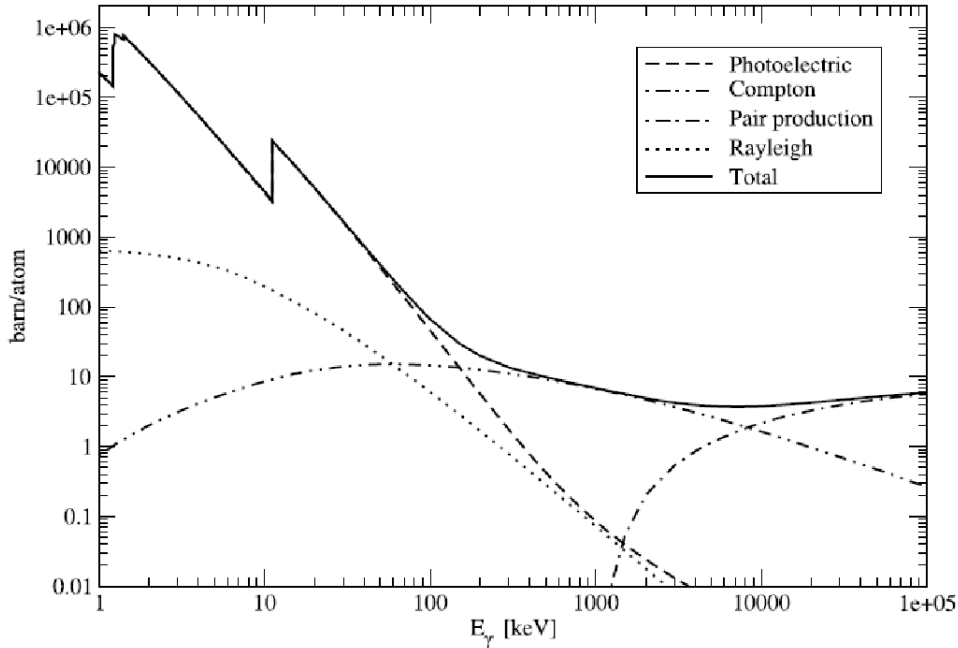


Figure 1.1: Cross section of  $\gamma$  radiation in Ge. (Source: *Nist-XCOM: Photon Cross Sections Database*).

sible to reconstruct the Compton scattering sequence and, therefore, the complete  $\gamma$ -ray path within the crystal from the end-point until the first interaction. This path will normally finish with a photoelectric absorption whether the energy is low enough. A conclusion one can follow is that, the better the  $\gamma$ -ray interaction position is determined, the better the quality of the tracking will be. There are many algorithms to determine the interaction position within the crystal. These algorithms can be grouped in two classes: back tracking algorithms [6] and forward tracking algorithms [7].

### 1.1.3 Tracking detectors: characteristics and requirements.

The tracking concept has allowed the development of  $4\pi$ -type detector systems, based only on HPGe crystals with a high segmentation density. This geometry allows to determine not only the deposited energy in a  $\gamma$ -ray interaction but also the complete path followed by the  $\gamma$ -ray within the crystal. With this combination it is possible to increase the peak-to-total without any anti-Compton shielding, increasing the detection volume and, therefore the efficiency of the system. But all this principle relies on the quality of the algorithm used to determine the  $\gamma$ -ray position

in each interaction within the crystal. This algorithm will depend, at the same time, in the spatial resolution achieved in the detection system.

Given that the tracking detectors allow to determine the  $\gamma$ -ray path within the crystal, it is also possible to detect and to correct the Doppler drift, which becomes relevant when working with high energy beams. Therefore, the energy resolution ( $\Delta E_\gamma$ ) is not only affected by the intrinsic energy resolution of the detector itself but also by the Doppler drift. In consequence, whether we can minimize the Doppler effect, we will increase the energy resolution in the detection system.

Concerning the requirements and taking into account that a tracking detector utilizes the Compton scattering formula as a main asset, the goal when designing such a type of detector is to optimize the capability to measure the magnitudes involved in this formula calculation. They are the energy and the spatial resolution which will determine the uncertainty of the  $\theta$  angle determination.

**Energy resolution.** When performing  $\gamma$ -ray tracking in a HPGe detector, the energy resolution for each  $\gamma$ -ray interaction is a critical parameter. In order to choose the optimum detection material it is necessary to find a compromise between energy resolution and detection efficiency. The easiest way to increase the efficiency is to use a high density, high Z material, as well as to increase the detection volume. But the highest density material has a poor energy resolution. The use of Ge crystals cooled with liquid nitrogen is the best solution found so far. This material offers a relatively high density ( $Z=32$ ), while its high purity allows to have big depleted volume with a moderate bias voltage. This is the key element to obtain high energy resolution. The depleted volume allows the charge carriers produced by the  $\gamma$ -ray interaction to move and be collected in the contacts. In next section the charge generation from a  $\gamma$ -ray interaction will be explained.

**Position Resolution.** A good energy resolution and high efficiency were a key requirement when designing a  $\gamma$ -ray spectrometer. In the new tracking detection systems, together with these two parameters the high spatial resolution requirement has been added. The most direct way to improve the spatial resolution in HPGe detectors is to segment the contacts which to collect the charge generated by the  $\gamma$ -ray interaction. Therefore, the crystal will be divided in cells which will generate charge signal whether the  $\gamma$ -ray has interacted within them or, at least, nearby. A second way to improve the spatial resolution will be to improve the algorithms used to calculate the interaction position from the charge signals following a  $\gamma$ -ray interaction. In the reconstruction algorithm improvement one key factor is the quality of the database generated by the characterization systems like the one developed in this thesis work. This database has the relation between each  $\gamma$ -ray interaction position in the HPGe volume and the corresponding electrical response.

### 1.1.4 Signal formation in HPGe detectors.

**Charge carriers production in semiconductor materials.** The interaction of the  $\gamma$  radiation with matter and more specifically with Ge by photoelectric effect, Compton scattering or pair production produces electrons in the material, so-called photo-electrons. The energy of the generated photo-electrons has the same order of magnitude of the incident  $\gamma$  radiation. These photo-electrons are, indeed, the charge carriers generated by the  $\gamma$  radiation hitting the Ge crystal and, in the presence of an electric field, generated by an external potential bias between the detector contacts, they will move from one contact to the other, allowing their collection. The direction of the movement will depend on the type of particle, electron or hole, and the type of Ge crystal, n-type or p-type.

To evaluate the quality of semiconductor detector, the number of charge carriers generated per unit of energy of the incident  $\gamma$ -ray. The higher the number of charge carriers generated, the better the detector is and the better the energy resolution will be. The parameter which represents the energy needed to generate a pair electron-hole is the electric permittivity,  $\varepsilon$ . In germanium, at 77 K, the value for this parameters is  $\varepsilon = 2.96$  eV.

**Charge carriers dynamic in semiconductor materials.** In order to understand how a charge carrier moves within germanium, let's describe a bit the main properties of such a semiconductor material. The High Purity germanium (HPGe) crystal are produced with an impurity concentration of  $\sim 10^{10}$  atoms $\cdot$ cm $^{-3}$  and they can be p-type or n-type crystals. The electric contacts, which are responsible to collect the charge carriers are made by implantation of boron in one side and lithium on the other. As presented in Figure 1.2, there are two different HPGe geometry configurations: planar and coaxial.

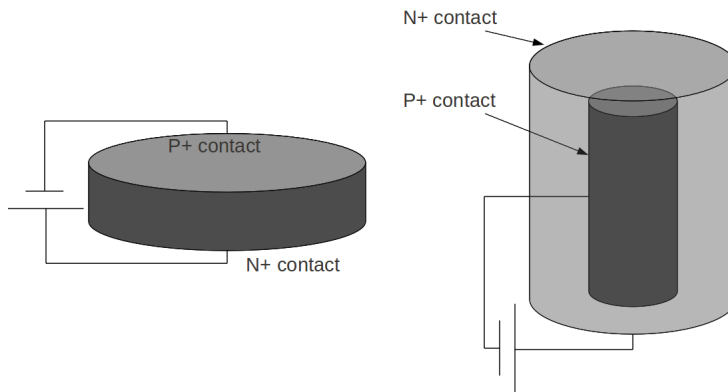


Figure 1.2: Planar HPGe detector configuration (left) and coaxial (right).

Inside the HPGe crystal, generated charge carriers move to the electric contacts thanks to the bias voltage existing between them. This fact generates the charge signal in the detector [8]. Therefore, it is possible to represent the electric behaviour of a HPGe detector with an equivalent circuit consisting on a current source  $i_s(t)$  in parallel with the equivalent capacity of the detector, as showed in Figure 1.3. The equivalent capacity of the detector ( $C_d$ ) is defined by the dielectric material between the two electrodes of the detector. The charge signal  $i_s$  will be proportional to the energy deposited in the interaction of the  $\gamma$ -ray in the HPGe crystal.

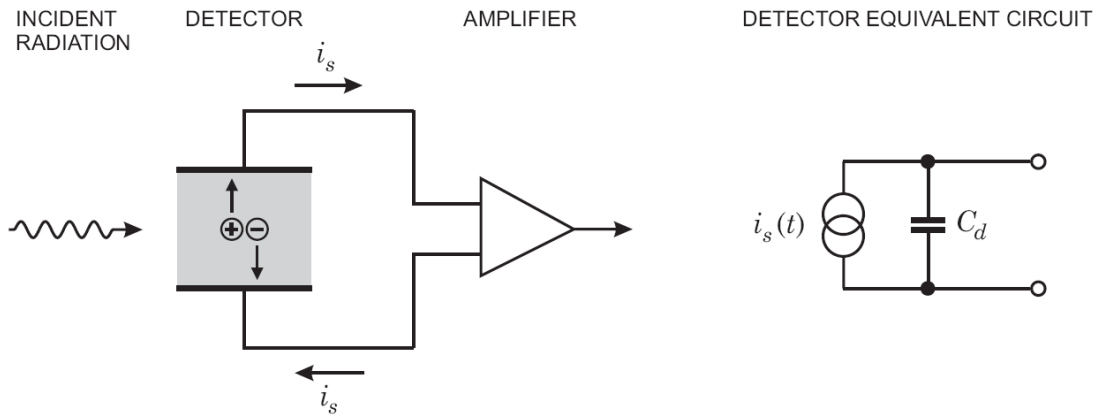


Figure 1.3: HPGe detector (left) and the equivalent circuit (right).

The problem to solve when obtaining the  $\gamma$ -ray interaction position within the volume of the HPGe crystal consists on detect the charge  $q$  generated in such a interaction position  $\vec{x}_0(t)$ . This charge will move under the electric field  $E$  between the two electrodes, each of them with a surface  $S_j$  and potential  $V_j$ . The applied bias between electrodes will generate the depletion zone. In order to evaluate the bias needed to generate a depletion zone in the volume of the crystal, the Poisson equation is applied,

$$\Delta\phi = -\frac{\rho}{\varepsilon}, \quad (1.2)$$

where  $\phi$  is the potential at any point of the crystal,  $\rho$  is the charge density per unit of volume, which depends on the impurity concentration, and  $\varepsilon_0$  is the Ge dielectric permittivity (16). The potential induces an electric field  $\vec{E}$ , which can be calculated using the gradient:

$$\vec{E}(\vec{x}) = -\nabla\phi(\vec{x}). \quad (1.3)$$

The electric field will be present all over the depletion zone, where the potential

has a gradient. For a planar configuration, with a distance  $d$  and a bias voltage  $V$  between the contacts,  $N$  impurity concentration, the electric field in any point located at a distance  $x$  far from the contact is given by the expression [9]:

$$\vec{E}(x) = \frac{V}{d} + \frac{qN}{\varepsilon} \left( \frac{d}{2} - x \right), \quad (1.4)$$

while for a coaxial configuration with an inner radius  $r_1$  and external  $r_2$ , the radial component of the electric field is:

$$\vec{E}(r) = -\frac{qN}{2\varepsilon} r - \frac{V - (qN/4\varepsilon)(r_2^2 - r_1^2)}{r \ln(r_2/r_1)}. \quad (1.5)$$

**Signal induction at detector contacts.** The total induced charge  $Q_i$  in an electrode  $i$  is calculated by integrating the normal component of the electric field  $\vec{E}$  out of the surface (Gauss law)

$$Q_i = \oint_{S_i} \varepsilon \vec{E} d\vec{S}_i. \quad (1.6)$$

On the other hand, by applying the Shockley–Ramo theorem [8], it is possible to calculate the induced charge in an electrode  $i$  provoked by a punctual charge  $q$  located at  $\vec{x}_0$  as:

$$Q_{q_i} = -q\psi_i(\vec{x}_0), \quad (1.7)$$

where  $\psi_i$  is  $\nabla^2\psi_i(\vec{x}) = 0$ . The movement of the charge  $q$  will induce a current  $I_{q_i}$  which is defined as:

$$I_{q_i}(t) = q\vec{E}_{\psi_i}(\vec{x}_0 \cdot \vec{v}(t)) \quad (1.8)$$

where  $\vec{v}(t)$  is the drift velocity of  $q$ ,  $\psi_i$  are the weight potentials and  $\vec{E}_{\psi_i} = \nabla\psi_i$  is the corresponding weight fields. Working under the Shockley–Ramo gives us the possibility to calculate the potentials  $\psi_i$  only once. At this point, it is possible to observe the dependency of charge mobility ( $\mu_{e,h}$ ) through the drift velocity  $v_{e,h}$ :

$$v_{e,h}(r) = \mu_{e,h}\xi(r) \quad (1.9)$$

Therefore, we have demonstrated that the induced charge along time depends on the position where the charge carriers were generated and, in consequence, on the  $\gamma$  ray interaction position, given that is this ray the one which generates the charge carriers. Therefore, by looking at the generated signal after a  $\gamma$  ray interaction within a semiconductor material it is possible to obtain not only the deposited energy in an interaction but its position as well.

Table 1.1: AGATA technical specifications.

Number of clusters	60
Number of crystals per cluster	3
Number of segments per crystal	37
Covered solid angle (%)	82
Number of channels	6660

**Signal Formation.** For each event, depending on the energy of the incident  $\gamma$  ray, more than one interaction can occur within the active volume. For valid events, in most of the cases, they will consist in a superimposition of several single interactions. In such a superimpositions the generated charge signals has a complex temporal dependency. Meanwhile, each single interaction has a temporal dependency which is determined by the instant position  $\vec{x}_e$  of the electrons cloud and the instant position  $\vec{x}_h$  of the holes cloud. Therefore, the generated charge signal, depending on  $t$  and induced in the contact  $i$  is:

$$Q_{q_i}(t) = q[\psi_i(\vec{x}_e(t)) - \psi_i(\vec{x}_h(t))] \quad (1.10)$$

At the time  $t_0$ , when the interaction has occurred,  $\vec{x}_e(t_0) = \vec{x}_h(t_0)$ , and, therefore,  $Q_{q_i}(t_0) = 0$ . In the following nanoseconds, the generated charges break away and travel in the opposite directions towards the corresponding electrodes. In the case of a n-type HPGe segmented detector, the electrons travels towards the core segment and the holes are collected in the closer segment.

When the charges arrive to their corresponding electrode, they recombine with their mirror charges. In that moment, a discontinuity occurs in the current signal. However the charge signals are not affected given that they correspond to the integral of the current flowing towards the electrodes. In a n-type detector, the segments produce negative signals given that they collect holes, while the core generates positive signals after collecting electrons. The segments where the interaction has not occur will only show up induced signals while the charge collection is happening.

**AGATA segmented detector at a glance.** The AGATA collaboration utilizes coaxial segmented detectors. It is composed of a total of 180 coaxial crystals, each one divided in 36 segments plus the core. Table 1.1 shows the main features of AGATA detectors. These specifications allow AGATA to reach 40% peak efficiency, and 60% peak-to-total for events with multiplicity 1, i.e., those which are not emitted in cascade. The geometry of AGATA is presented in Figure 1.4. This set-up allows an angular resolution  $\Delta\theta = 1.25^\circ$ .

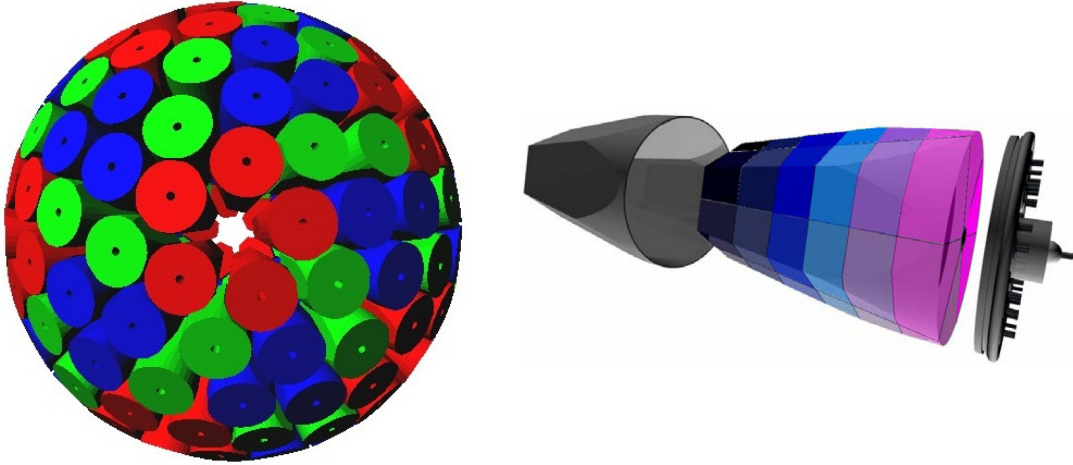


Figure 1.4: The  $4\pi$  set-up of AGATA (left) and one of its capsules with the 36 segments plus the central core (right).

Each AGATA crystal has 90 mm length, 80 mm diameter in the rear side and a hexagonal shape in the frontal side. The detailed view is presented in right part of Figure 1.4. The spatial resolution is 5 mm thanks to the 36 segments. Each segment is individually read by a digital read-out channel in charge of acquire, process and digitize each generated signal. But before going to the digitizer each charge signal is pre-amplified, then it is digitized by an analogue-to-digital converter working 100 Mhz with 14 bits dynamic range. The digitized signals are sent to the pre-processing unit where the energy and the interaction time is determined by applying *Pulse Shape Analysis* (PSA) techniques. After the pre-processing the data is stored in server farms. The data is then analysed with the tracking algorithm which will determine the complete path of each  $\gamma$  ray within the active volume of the HPGe crystal.

When a  $\gamma$  ray interacts in the active volume of AGATA, it generates a charge in the segment where it has been interacted, as above explained. But the interaction also induces signals in the neighbours. The induced signals are proportional to the distance between the segment where the signal has been induced and the  $\gamma$  ray interaction position. This effect is studied by the PSA techniques and, looking at induced charges in the neighbours, it allows to determine not only in which segment a  $\gamma$  ray has interacted but also where inside this segment the interaction has occurred. The Figure 1.5 illustrates what we have explained. A photon interacts in the segment A2 (red) and it generates a charge signal on it. The induced signals in the adjacent segment A1, A3, B1, B2, B3, F1, F2, F3 (green) are used to specify the vertical

position within A2. The radial information is obtained from the collection time of the charge, which depends on the distance between the interaction position and the core. As a last point, the integration of all collected charge signals allows to calculate the energy deposited in the HPGe crystal by the  $\gamma$  ray interaction.

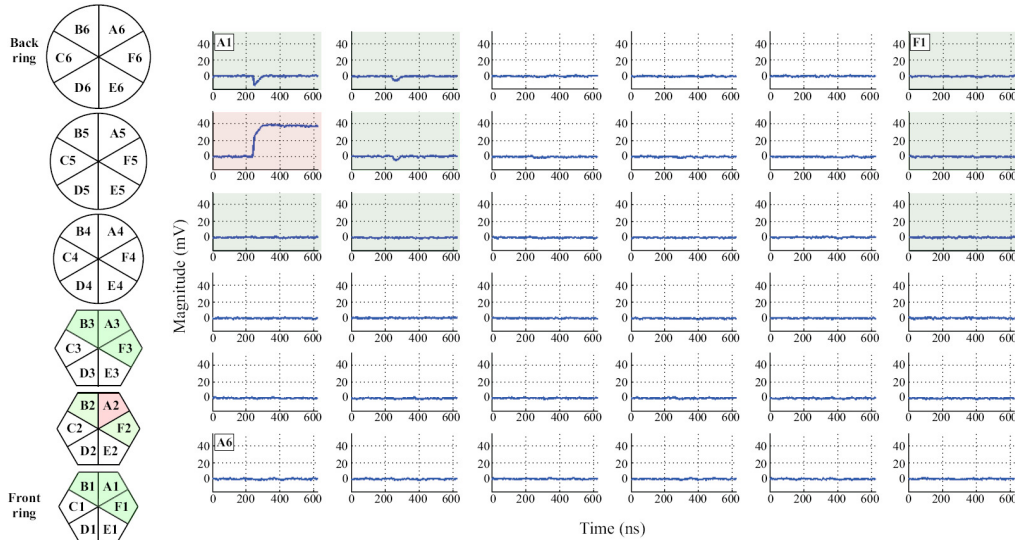


Figure 1.5: Pre-amplifiers output for a single event in an AGATA crystal. The segment where the  $\gamma$  ray has interacted is indicated in red. Green segments are those where the induced signal is presented.

### 1.1.5 Pulse shape analysis for interaction position determination.

As it was demonstrated in the last section, the pulse shape generated by a  $\gamma$  ray interaction within a HPGe crystal will depend on the interaction position. Therefore, in principle, it would be possible to know the interaction position by making a pulse shape analysis. The question now is: how that is done?. The answer to this question is by using algorithms which compare the pulses generated during the measurement with a database which has a map of interaction position within the detector volume and the associated electrical response. This method has two weak points: on one hand the algorithm utilizes simulated databases and, on the other hand it compares simulated pulses with experimental ones, which have certain statistical noise. At this moment, the most used algorithms are the Adaptive Grid Search (AGS) [10, 11], genetic algorithms [12] and matrix methods [13, 14]. In the AGATA collaboration,

the method used is AGS, where the pulse shape comparison is based on the *figure of merit* given by the expression:

$$FOM = \sum_{j \in N} \sum_{i=T_0}^{T_{end}} (S_{ij}^m - S_{ij}^c)^p, \quad (1.11)$$

where  $S_{ij}^m$  and  $S_{ij}^c$  are the, respectively, the experimental and simulated pulses. Indexes  $j$  and  $i$  represent the different segments within the HPGe crystal. As an alternative to this method, in our group we have developed an algorithm to compare signals which has into account the different statistical noise sources, including the main one coming from the electronic noise. These source are taken into account by our algorithm when doing the comparison between pulses [15]. At this moment, we can figure out that one critical point when comparing pulses to obtain the  $\gamma$  ray interaction position in HPGe detectors is the quality of the database used in the figure of merit. As mentioned before, this database contains the electrical response of the crystal for each photon interaction and, therefore, its spatial resolution will limit a lot the quality of the figure of merit. Also it is important to remark that each crystal is unique. The fabrication process of the HPGe crystal, where the crystal is grown up by deposition, gives to each crystal a unique characteristics and, in consequence, a unique electrical response for each  $\gamma$  ray interaction position. The simulations do not take this fact into account and it makes necessary to use high resolution experimental characterization system when one wants to elaborate a reliable database for each crystal. The main goal of this thesis work is to develop and validation of a characterization system of the electrical response for HPGe detectors.

All tracking algorithms at that moment utilize simulated databases to determine the  $\gamma$  ray interaction position. This is due mainly to two factor. On one hand the large number of existing crystals and the long time it takes to experimentally characterize each one makes impossible to individually characterize each one. On the other hand, there is no rigorous validation for most of the experimental characterization method. This makes impossible to apply the results obtained from a experimental characterization to real measurements without a proper validation of the characterization system used to obtain the database.

The simulation algorithms used offer the possibility, by using mathematical models of the electric field within the Ge crystal, to generate a complete database of  $\gamma$  ray interaction positions with the corresponding electrical response. The most used one is the Multi Geometry Simulation (MGS) [16] code. It is developed by the *Institut de Recherche Subatomique* (IRes) in Strasbourg and it is currently the one used by the AGATA collaboration. MGS uses a multi-step algorithm as presented in Figure 1.6.

It generates the pulse shape database by using a grid of points within a cubic network with 1 mm step. The simulated data is stored in matrix. The value of

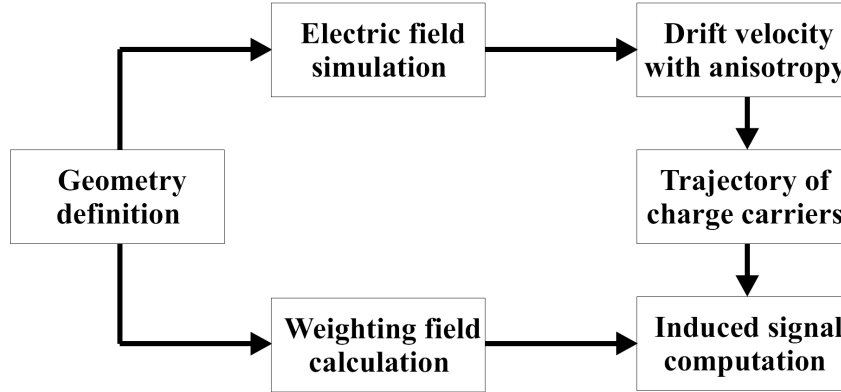


Figure 1.6: Data flow diagram in MGS.

each matrix point is used at the end of the process to generate the electrical pulse shapes, determined by the path of the charge carriers through the mean electric field. In consequence, electrical response of the simulated detector is calculated for each position of the grid by following the charge carriers through the electric field and evaluating at each moment their drift velocity from the electric matrix.

Following the flow diagram of Figure 1.6, MGS needs a set of parameters that user must define, such as the crystal size, the bias voltage, the impurity concentration, the operational temperature, the detector geometry, etc. Having this parameters, MGS evaluates the potential surface and the electric field lines all around the active volume of the crystal, by applying the Poisson equation (1.2). Due to the complex geometry of AGATA crystals, MGS utilizes some simplifications to solve the Poisson equation. Once the equations are solved all around the volume, the potential and electric field are evaluated and the user can look at them. The final result for a complete simulation of an AGATA crystal with MGS is presented in Figure 1.7.

When the potential surfaces are solved, an algorithm is in charge to reproduce the charge carrier transport within a semiconductor material, taking into account the anisotropy in the electrons and hole mobility. This allows to evaluate the paths of such charge carriers for any arbitrary point within the active volume of the HPGe crystal. An example for drift velocities for electrons and holes in AGATA is presented in Figure 1.8.

The combination of the paths obtained allows to calculate the induced charge in the detector contacts by applying the Shockley–Ramo theorem [17, 8], i.e., the generated pulse will depend on the trajectory of the charge carriers when they move within the electric field existing in the active volume of the detector:

$$Q = -q \int_{x_2}^{x_1} \xi_Q dl = q[V_Q(x_1) - V_Q(x_2)] \quad (1.12)$$

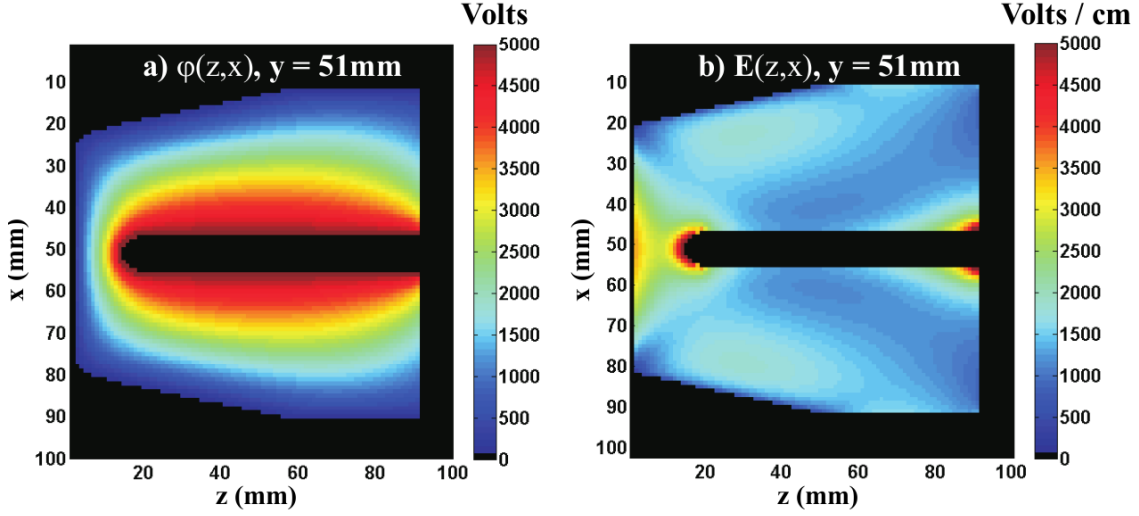


Figure 1.7: Potential surfaces and electric field lines in a ZX plane for an AGATA crystal given by MGS. The results show, as expected, how the electric field decreases with the radius from the central anode.

where  $x_1$  and  $x_2$  are the positions before and after of the charge  $q$ ,  $V_Q$  is the potential existing between the contacts and  $\xi_Q$  is the electric field.

The main drawback of the simulation codes when obtaining the database of pulses within a HPGe crystal is that they do not have into account, in a realist manner, the inhomogeneities in the impurity concentrations and in the mobility of the charge carriers in the different parts of the active volume. Other source of error comes from the fact that the size of the crystal is not necessary an exact multiple of the grid size used by the code. Therefore, in the edges of the crystal, the code has to interpolate the results causing errors in the signal generation at these points. Finally, the MGS code does not implement the transfer function of the pre-amplifiers which normally goes together with the HPGe detectors. The bandwidth of the pre-amplifier limits and makes slower the electrical response of the detector. This fact is not taken into account by the code when generating the final results for a detector.

Given the lack of precision introduced by the simulation codes in the pulses, it is necessary to review the method used to characterize the electrical response in the HPGe detectors. With this goal, we have developed and high precision experimental system which gives a reliable database within a reasonable period of time. This system will allow on one hand to improve the results given by the simulated methods, by comparing and cross-check both results for a particular crystal and, on the other hand, in the same electronics is used, to apply the experimental database characterization results in the tracking algorithm when AGATA works in real experiments.

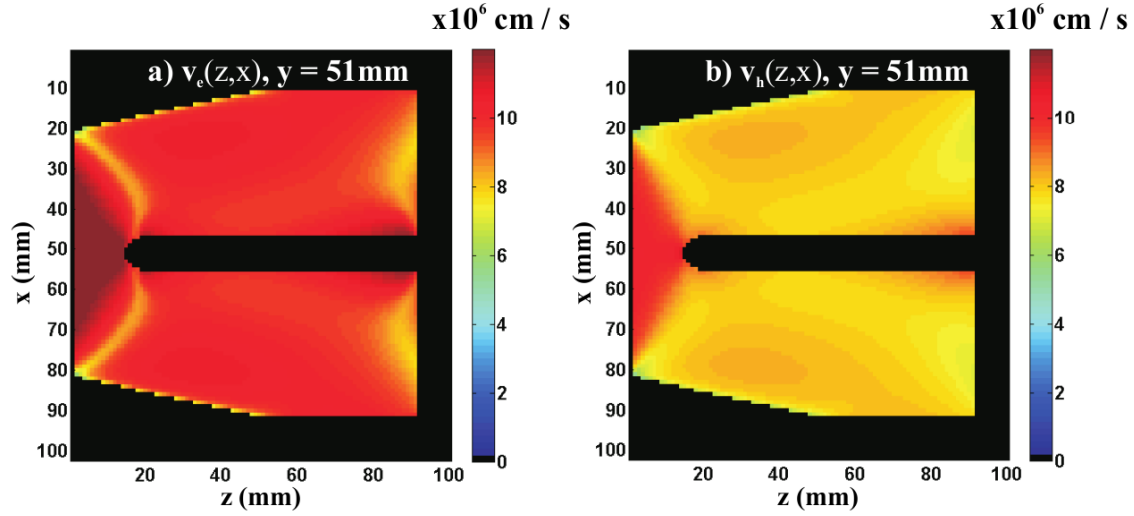


Figure 1.8: Drift velocities in electrons and holes (ZX plane) in an AGATA crystal.

## 1.2 Experimental characterization systems of the electrical response: state of the art.

### 1.2.1 Mechanical systems.

The experimental characterization for HPGe detectors is a much more accurate method to get the electrical response database. In this method, the database having the relation between  $\gamma$  ray interaction position and the associated electrical response is made for each crystal individually. These type of characterization systems utilize analogue-to-digital converters (ADC) to digitize and analyse the generated charge signal for each  $\gamma$  ray interaction within the HPGe crystal. Therefore, the most critical point in these systems is the accurate determination of the interaction position of each  $\gamma$  ray. In the mechanical system, a collimated radioactive source is moved, by using a high precision mechanics, along one the sides of the crystal under characterization until all the side is well covered. An example of mechanical characterization system is in the Nuclear Physics group of the University of Liverpool, in UK [18, 19].

In such a systems, the valid events are ones which have a  $90^\circ$  Compton scattering in the HPGe crystal and, then, are detected in one of the surrounding auxiliary detectors. As presented in Figure 1.9, where the Liverpool scanning system is shown, the collimated source moves in in the plane XY, parallel to the front face of the AGATA crystal. Two step-by-step motors with a precision of 0.5 mm are in charge to

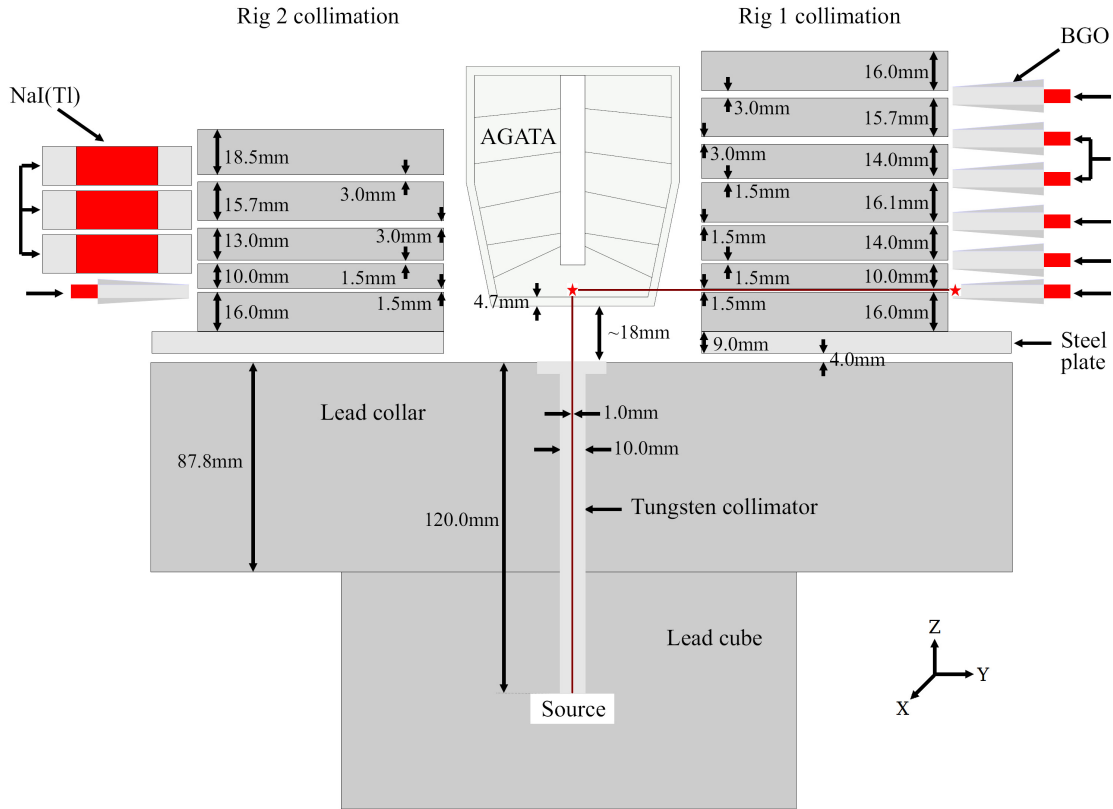


Figure 1.9: Schematics of the Liverpool's scanning system with an AGATA crystal in place. The red star shows an example of a valid event: The  $\gamma$  ray has a Compton scattering of  $90^\circ$  in the AGATA crystal and then it is detected by one of the surrounding auxiliary detectors.

move the collimator containing the source. For some  $\gamma$  rays, with a well known  $(x,y)$  position given that it corresponds with the position of the collimator, a Compton scattering can occur in the HPGe crystal. Some of the Compton scattering will have a scattering angle of  $90^\circ$  and they will be detected by the auxiliary detectors. In such a cases, the collimating rings surrounding the HPGe crystal will allow to determine (purely mechanically) the  $z$  coordinate. The electrical response for all the events fulfilling all these conditions will be recorded together with the  $(x,y,z)$  interaction position within the crystal, obtaining this way the desired database. An extra element to ensure that the recorded elements are the correct ones comes from the data acquisition system. Only the event in coincidence between the HPGe and the auxiliary detectors can be recorded.

The drawback of such a systems is the strong dependency with the mechanics of

the system. For instance, the collimator rings surrounding the HPGe detectors do not allow to have events all along the  $z$  component of the crystal (see Figure 1.9). Also the beam divergence due to the finite size of the collimator hole is a source uncertainty in these systems. As a consequence, the spatial resolution expected in these systems is about 4 mm when determining where the  $\gamma$  ray has interacted in within the HPGe crystal. Finally, the needed time to fully characterize a crystal can be up to six months given the low statistics due to the collimation rings. For all these reasons, many AGATA groups, like ours, are trying to develop new type of experimental characterization systems which can improve the listed problems.

### 1.2.2 Active collimation systems.

As an alternative to the mechanical characterization systems, a new type of experimental characterization systems have arrived with the ones based on the combination of two concepts: the first one is the Pulse Shape Analysis Comparison (PSAC) [20]. The PSAC technique can be combined both with the precise positioning of the HPGe crystal in front of a collimated source which is moved all around the detector volume [21] or with the annihilation  $e^-e^+$  in a source of positrons to obtain collinear  $\gamma$  rays which are used to scan the complete crystal volume [22]. Two groups are working in characterization systems based on the active collimation right now.

**GSI - Darmstadt. Germany.** The characterization system of the *Gesellschaft für Schwerionenforschung* (GSI) in Darmstadt, Germany, is based on a  $^{22}\text{Na}$  source of positrons which delivers two collinear  $\gamma$  rays with 511 keV energy each. The two  $\gamma$  rays travel in opposite directions. The second element of this system is the PSAC used to compare and group the pulses generated by the  $\gamma$  rays arriving to the HPGe crystal. The source is placed between the HPGe detector and a Position Sensitive Detector (PSD) as presented in Figure 1.10. The PSD allows to determine the paths of the  $\gamma$  rays hitting in the HPGe detector. Each path is stored together with the electrical response of the HPGe detector. Then, the set PSD+source are rotated  $90^\circ$  with respect to the HPGe detector axis in order to obtain a second set of  $\gamma$  ray paths and the corresponding electrical response of the HPGe detector from a second perspective. After the two set of data is obtained, they are compared and, whether a pair of electrical responses in the HPGe are compatible under the PSAC, the interaction point is determined (if it exists) from the two associated  $\gamma$  paths.

**IPHC - Strasbourg. France.** The characterization system of the *Institut Pluridisciplinaire Hubert CURIE* (IPHC) in Strasbourg, France, is based in the high-precision positioning of the HPGe crystal in front of a collimated  $^{137}\text{Cs}$  source. The positioning of the crystal is accomplish thanks to a laser. Then, the movement of the source for each scanning step varies between 50 and 100  $\mu\text{m}$ . With the source facing one side of the crystal, a first scan is performed. The collimator position

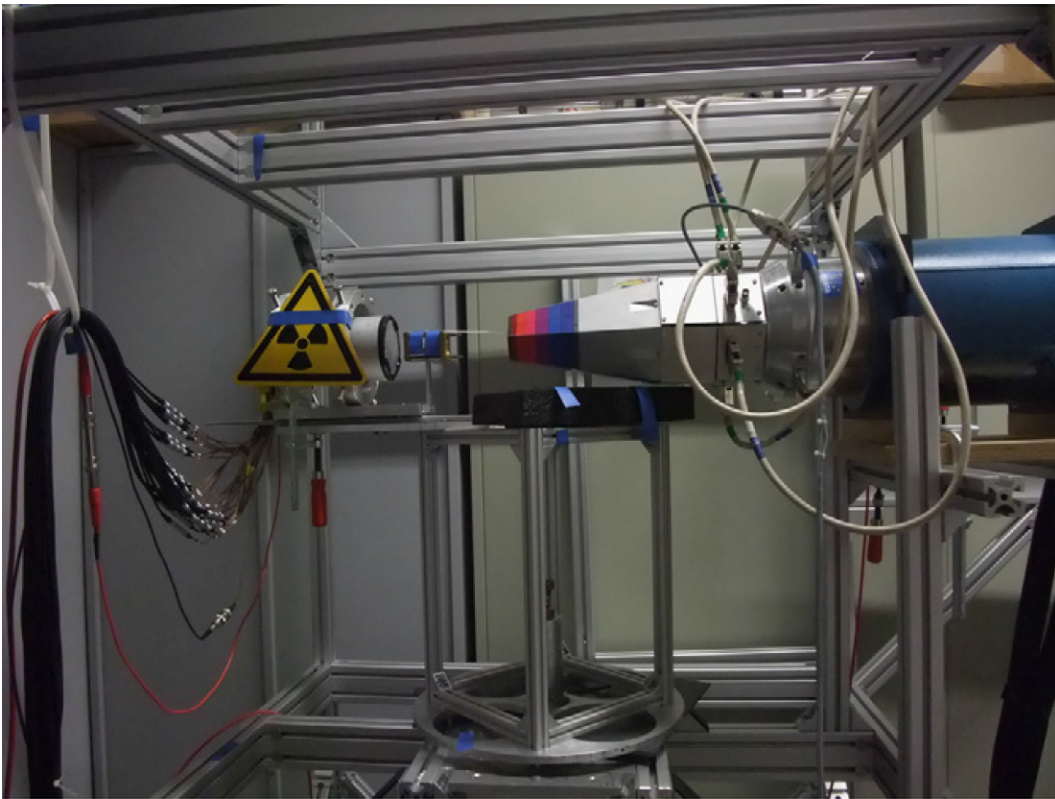


Figure 1.10: AGATA crystal in place to be scanned with the GSI scanning system.

together with the electrical response of the HPGe crystal. Then the HPGe crystal is rotated  $90^\circ$  and the process happens again. With this scanning principle the geometrical problem does not exist given that the  $\gamma$  ray paths are well known and, therefore, it is possible to determine which paths are going to intersect in a point. After both sides are scanned, the PSAC is applied to the paths that are geometrically intersected. The compatible points are added, together with the electrical response of the crystal to the database. In Figure 1.11 shows an AGATA crystal in the Strasbourg scanning system. There are not publications concerning the total spatial resolution of this scanning system.

At this point, it is important to note that, up to now, the experimental characterizations are very limited and the obtained databases have never been applied to AGATA when it works in a real experiment. For that reason, there is still a big path to investigate in that sense.

Along this document, all the conference proceedings and articles published during the conception process, development and validation of SALSA are included. Since they were published in chronological order, they are coherent by themselves and



Figure 1.11: AGATA crystal in place to be scanned with the IPHC scanning system.

nothing further is needed. Only a brief introduction to each one will precede each publication in order to contextualize it.



# Bibliography

---

- [1] Official FAIR homepage: <http://www.gsi.de/portrait/fair.html>
- [2] Official HIE-ISOLDE homepage: [isolde.web.cern.ch/](http://isolde.web.cern.ch/)
- [3] Official SPIRAL2 homepage: <http://www.ganil-spiral2.eu/spiral2>
- [4] Official SPES homepage: <http://www.lnl.infn.it/spes/>
- [5] ORTEC. High-Purity Germanium (HPGe) Detector Manufacturing.
- [6] J. van der Marel, B. Cederwall, Nuclear Instruments and Methods in Physics Research Section A 437 (1999) 538.
- [7] G.J. Schmid, et al., Nuclear Instruments and Methods in Physics Research Section A 430 (1999) 69.
- [8] H. Spieler. Semiconductor Detector Systems. Oxford Science Publications
- [9] Radioisotopes and Radiation Methodology. Med Phys 4R06/6R03
- [10] R.Venturelli,D.Bazzacco, LNL Annual Report 2004, INFN-LNL, Legnaro, Italy, 2005,p.220
- [11] M.Schlarb,Simulation and Real-Time Analysis of Pulse Shapes from Highly Segmented Germanium Detectors,Ph.D.thesis,Technical University Munich,2008
- [12] T.Kröll, D.Bazzacco, Nucl. Instrum. Meth. Phys. Res. A565 (2006) 691
- [13] A.Olariu, Pulse Shape Analysis for the Gamma-ray Tracking Detector AGATA, Ph.D.thesis,Université Paris-Sud 11,Orsay France, 2007
- [14] A.Olariu, et al., IEEE Transactions on Nuclear Science NS-53 (2006) 1028
- [15] S. Martin et al. Nucl. Instrum. Meth. Phys. Res. A 32-40 (2016) 823
- [16] A simple method for the characterisation of HPGe detectors, P. Medina, C. Santos, Di Villaume, Istr. Meas. Tech. Conf (2004).

- [17] Glenn F. Knoll. Radiation Detection and Measurement. JW Editions
- [18] M.Descovich,et al.,Nuclear Instruments and Methods in Physics Research Section A 553 (2005) 535
- [19] Matthew R. Dimmock, el al.,IEEE Transactions on Nuclear Science, VOL. 56, NO. 4, AUGUST 2009
- [20] F.C.L. Crespi, F. Camera, Nucl. Inst. and Meth. A 593 (2008) 440-447
- [21] M. Ginsz et al., IPHC scanning table status. Ganil Internal report 18-10-14.
- [22] César Domingo-Pardo, Namita Goel., IEEE Trans. on Med. Imaging, 28, 12 (2009) 2007-2014

---

## Chapter 2

# Proceedings. Towards a high resolution $\gamma$ camera.

---

The first work when starting the development of SALSA was to optimize one of the key elements of the system: The  $\gamma$  camera, in charge to determine the  $\gamma$  ray paths coming from the  $^{22}\text{Na}$  source, as explained in the introduction of both proceedings.

In the first proceeding different algorithms were testes in order to evaluate the quality that they offered together with our  $\gamma$  camera. The results were presented in the second edition of the *International Conference on Advancements in Nuclear Instrumentation Measurement Methods and their Applications (ANIMMA), 2011*. It is important to point that, even if these algorithms were not the ones finally used in SALSA, they motivated us to make the set-up of all the electronics of SALSA which, by itself, was a big milestone in the SALSA development.

In the second proceeding the preliminary results of the final reconstruction algorithm used by SALSA, based on the Gaussian fit of the light distribution generated in the scintillator crystal of the  $\gamma$  camera, were presented in the *IEEE Nuclear Science Symposium Conference Record, 2011*.



# Towards a Deep Characterization of a 64-fold-pixelated Position Sensitive Detector for a New $\gamma$ -Scanning System of HPGe Segmented Detectors

A. Hernández-Prieto and B. Quintana

**Abstract**—Characterization of the electrical response of the HPGe segmented detectors is one of the current goals for the Nuclear Physics community in order to perform  $\gamma$ -ray tracking or even imaging with these detectors. For this purpose, scanning devices have to be developed to achieve the signal-position association with the highest precision. In this laboratory, a new scanning system, SALSA (SALamanca Lyso-based Scanning Array), consisting on a high spatial resolution  $\gamma$  camera, is under development. In this work the whole scanning system is presented and first results for the characterization of the  $\gamma$  camera are shown.

**Index Terms**—Position Sensitive  $\gamma$ -ray scintillator Detector (PSD), Pixelated Position-Sensitive PhotoMultiplier Tube (PSPMT), Maximum Pixel Charge Analysis (MPCA), SALamanca Lyso-based Scanning Array (SALSA)

## I. INTRODUCTION

**T**he new nuclear experiments in the new Radioactive-Ion Beam (RIB) facilities which require more efficient and sensitive  $\gamma$ -spectroscopy devices. With this objective a new development has been achieved with  $\gamma$ -ray tracking Ge detectors by segmenting the electrical contacts, responsible for collecting the charge carriers released in each photon interaction. The most relevant examples of these detectors can be found in AGATA [1] or GRETA [2] collaborations. This makes it feasible the determination of the interaction point which enables for tracking the  $\gamma$ -ray. But as intermediate step it is necessary to characterise the electrical response of the Germanium crystals with respect to the interaction point of the photon within the crystal. At the same time, to explore in deep the capabilities of Ge segmented detectors it is mandatory to reach the maximum precision in their characterisation. To perform this task, scanning systems which use a radioactive source and ancillary detectors devoted to detect in coincidence with the Ge detector the  $\gamma$  products of the disintegration are used. The most extended systems are based on the mechanical movement of the collimated source with respect to the detector. Their main drawbacks are the long time needed to scan the whole detector and the high activity of the source required. As alternative to this method, the PET principle [3] can be used, for which a Position Sensitive  $\gamma$ -ray scintillator Detector

(PSD) capable of determining the 511keV  $\gamma$ -ray directions is needed.

The organization of this article is the following: in section II the principles of our scanning system and its set-up are presented. Several algorithms and their results for reconstructing the interaction position are showed in section III. In section IV firsts results of linearity and spatial resolution in the centre of the PSD are exposed.

## II. SCANNING PRINCIPLE

The set-up of SALSA is made up of a  $^{22}\text{Na}$  source, which provides two simultaneous 511 keV gamma-rays in opposite directions, a set of four PSDs and the HPGe detector to scan. The PSD consists in a lutetium yttrium oxyorthosilicate (LYSO) scintillating crystal, read-out by a pixelated position-sensitive photomultiplier tube (PSPMT) H10966A-100 from Hamamatsu [4]. Each PSPMT has an output of 64 channels, one per pixel, plus the last dynode signal. This leads to a total of 260 electronic signals in the system. The charge signals from the PSPMT are integrated and digitized by eight V792 charge-to-digital conversion QDC VME modules from CAEN [5]. They have an input range from 0 to 400pC and a digital resolution of 12 bit. In order to read out the 256 QDC channels, the standard acquisition system from GSI, the MultiBranch System (MBS) [6] is used. This system runs under the Lynx real-time operative system in a VME PowerPC platform RIO4-8072RE 1GHz, from CES [7]. The online and offline were performed via the GSI Object Oriented Online Offline system Go4 [8], based on the ROOT package of CERN [9].

A complete explanation of the electronics used in the system will be given in a separate publication. Schematic for whole SALSA system is shown in Figure 1.

Among all the couples of  $\gamma$ -rays produced by the  $^{22}\text{Na}$  source, some of them will be detected in the PSD and in the Ge detector in coincidence. Assuming that the  $\beta^+$  annihilates at rest, the direction of both  $\gamma$ -rays in the lab frame is opposite. Therefore, knowing where the  $\gamma$ -ray impacts on the PSD, it is possible to know the direction of the  $\gamma$ -ray which impacts in the Ge detector. But to know the interaction position in the Ge detector another scan in a different geometrical configuration of the system has to be performed. By comparing the Ge electric pulses corresponding to crossing directions, one is able

A. Hernández-Prieto and B. Quintana are with the Laboratorio de Radiaciones Ionizantes, University of Salamanca, 37007 SPAIN

A. Hernández-Prieto contact e-mail: alvaro.prieto@usal.es

Manuscript received May 19, 2011; revised --.

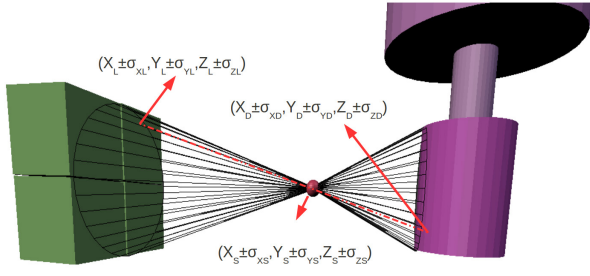


Fig. 1. Schematics for SALSAs. The HPGe detector to scan is presented in purple, whereas the PSDs are in green. the point-like  $^{22}\text{Na}$  source is drawn red, and the  $\gamma$ -cones generated are placed in black

to determine the precise point of interaction associated to the pulse. Once we have a set of interaction points covering the Ge crystal together with their corresponding electric pulses, Pulse Shape Analysis (PSA) techniques [10] are used in the characterization. For this purpose a high position resolution is needed in the system, in order to know accurately the direction of the  $\gamma$ -ray and, after the characterization process, the interaction point in the Ge detector.

### III. IMAGE RECONSTRUCTING ALGORITHMS

The individual gain in each pixel in the PSPMT varies very much, as one can see in [4]. Since our system is based on an Individual MultiAnode Readout (IMAR), we can adjust in advance the gain of each pixel in order to reduce the image distortion. Once this is done, The following image reconstruction algorithms were tested in the central part of the PSD.

#### A. Anger Centroid Algorithm

Assuming  $n_j^i$  charge signal from the PSPMT anode corresponding to  $k$ -th row and  $j$ -th column, the centroid coordinate along the  $x$  direction taking the Anger logic [11] classical algorithm can be written as follows:

$$X_C = \frac{\sum_j n_j x_j}{\sum_j n_j} \quad (1)$$

where  $n_j = \sum_i n_j^i$  is the projection of the charge collected along the  $j$ -th column with  $x_j$  coordinate along  $x$ -direction. The same is applied along  $y$ -direction.

#### B. Algorithm for SMALL Devices

Based on the idea of Anger logic, one can modify the centroid expression as follow [12]:

$$X_C = \frac{\sum_j n_j' x_j}{\sum_j n_j'} \quad (2)$$

where now, the centroid calculation is made taking the square of the charge collected in each pixel  $n_j' = \sum_i (n_j^i)^2$ . This improvement allows us to narrow the light Point Spread Function of the image ( $PSF_{image}$ ) and consequently the spatial resolution increases.

#### C. Maximum Pixel Charge Analysis (MPCA)

In this method, we explore the same principle as Pulse Shape Comparison used in AGATA collaboration [10]. Taking this principle, we select the pixel with maximum charge event by event and then its neighbours are analyzed. Assuming a starting reconstructed position in the centre of the pixel with maximum charge (mpc), one can move within that pixel along the directions (X,Y) a positive or negative distance and more or less in function of weights given by charges of neighbouring pixels normalized. The pattern of these movements are expressed as follows, corresponding to the values shown in Figure 2.

$$X_{reconstructed} = X_{mpc} + \frac{L}{2} \frac{1}{n_{i,j}} \times (n_{i+1,j} - n_{i-1,j} + n_{i+1,j-1} - n_{i-1,j+1} + n_{i+1,j+1} - n_{i-1,j-1}) \quad (3)$$

$$Y_{reconstructed} = Y_{mpc} + \frac{L}{2} \frac{1}{n_{i,j}} \times (n_{i,j+1} - n_{i,j-1} + n_{i-1,j+1} - n_{i+1,j-1} + n_{i+1,j+1} - n_{i-1,j-1}) \quad (4)$$

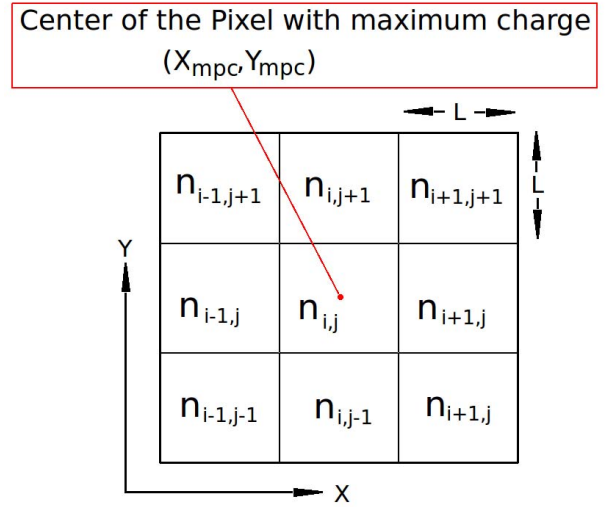


Fig. 2. Charge distribution pattern around the maximum pixel charge (mpc)

### IV. LINEARITY AND SPATIAL RESOLUTION

In order to study the different algorithms for position reconstruction presented in the last section, a collimated  $^{22}\text{Na}$  source, using 5cm of lead with a hole of 1mm, has been used. Sixteen sets of data corresponding to different positions along the centre PSD were taken, as shown in Figure 3.

The collimated positions correspond to one pixel in the centre of the PSD. The values for the coordinates of these positions are shown in Table 1 ( $X_{Mec}$ ,  $Y_{Mec}$ ). The linearity of the system is defined by the following equation:

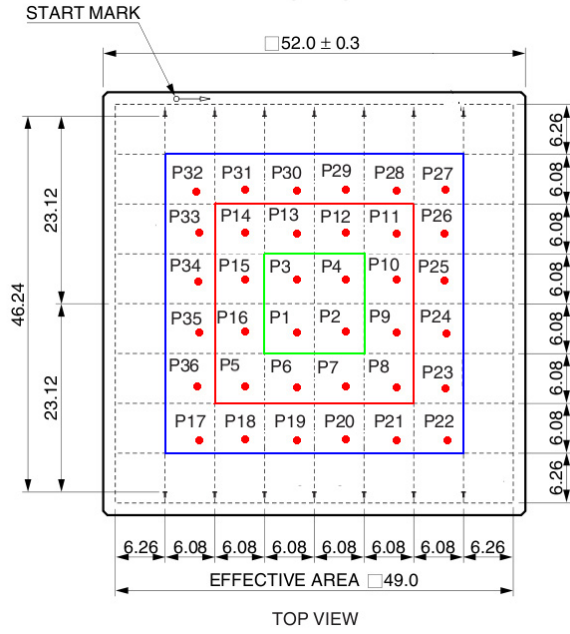


Fig. 3. Pattern of positions where the collimated source was placed. The corresponding values for  $(X_{Mec}, Y_{Mec})$  values are shown in Table 1

$$L = \frac{\Delta X_{measured}}{\Delta X_{mechanical}} \quad (5)$$

for the X component, and in the same way for the Y component. The linearity represents the angular coefficient of linearity curve at each measured point. With this definition, the linearity of the central part of the PSD is calculated using the method developed in our laboratory, the MPCA. The results are shown in Figure 4.

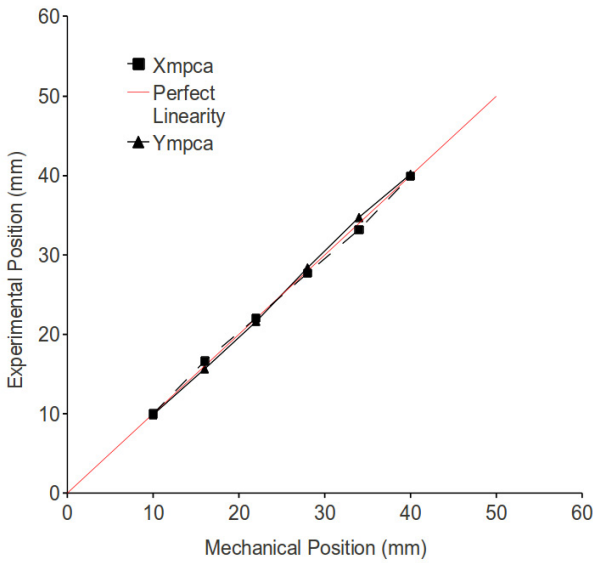


Fig. 4. Linearity of the PSD along the two main axis when the MPCA technique is used. The red line illustrates the linearity of the system with an ideal PSD

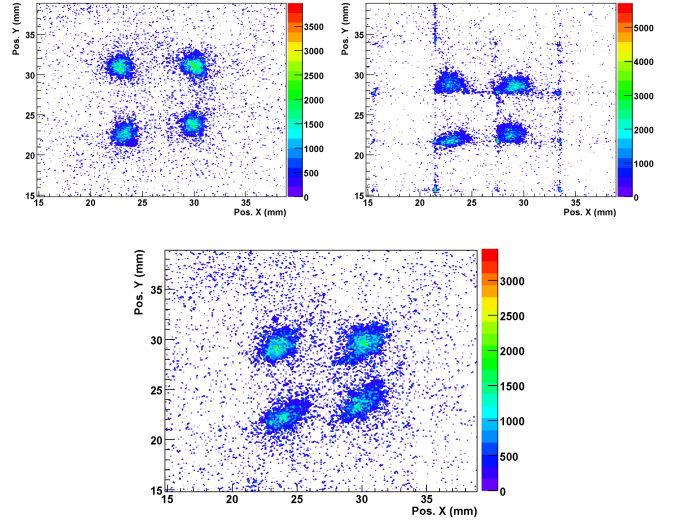


Fig. 5. Contour plots of the central positions measured when the collimated source was placed at the location given in Fig. 3. (Top left) Anger Logic algorithm. (Top right) Square Anger Logic approach. (Bottom) the MPCA method developed in our laboratory

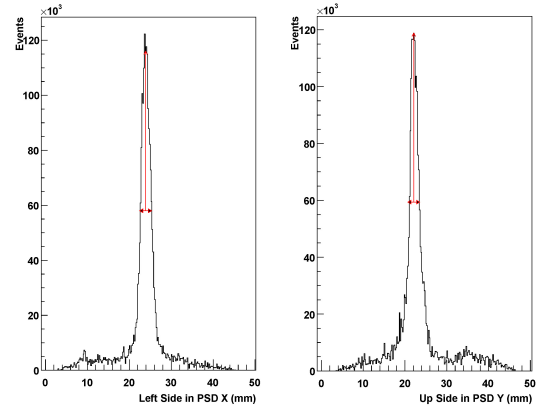


Fig. 6. Position distribution on X (left) and Y (right) for 1mm collimated source placed in the centre of the PSD

If we compare the results obtained with MPCA method with the ideal case, it can be concluded that our PSD behaves linear ( $L=1$ ) in both X and Y main axis. With this good linearity value, the expression for the Spatial Resolution can be simplified:

$$SR = \frac{PSF_{image}}{L} \quad (6)$$

and now, the spatial resolution can be assumed as the FWHM of the  $PSF_{image}$ .

In order to determine that spatial resolution, the collimated positions shown in Figure 3 were reconstructed with the algorithms under study, the results for the four central collimated positions are presented in Figure 5 and the analysis of the whole data is shown in Table 1. The uncertainties are calculated taking the FWHM of the  $PSF_{image}$  in X and Y

TABLE I  
POSITION VALUES OBTAINED WITH DIFFERENCES IMAGE RECONSTRUCTION METHODS

Position	$X_{Mec}$ (mm)	$Y_{Mec}$ (mm)	$X_{MPCA}$ (mm)	$Y_{MPCA}$ (mm)	$X_{Anger}$ (mm)	$Y_{Anger}$ (mm)	$X_{Square}$ (mm)	$Y_{Square}$ (mm)
1	22±1	22±1	23.75±1.35	22.25±1.20	23.45±1.05	22.75±0.60	22.75±1.75	21.75±0.60
2	28±1	22±1	29.85±1.40	23.45±1.35	30.15±0.80	23.35±0.90	28.95±1.25	22.55±1.20
3	22±1	28±1	23.75±1.35	29.45±0.45	22.95±0.40	30.95±1.05	23.05±1.20	28.55±1.10
4	28±1	28±1	30.15±0.50	29.75±1.20	29.95±1	30.95±1.05	29.15±0.80	28.55±1.10
5	16±1	16±1	16.25±1.20	16.85±0.75	15.05±1.05	16.35±0.50	16.25±1.05	15.95±0.70
6	22±1	16±1	21.35±0.90	16.25±1	19.65±1.20	16.25±1.20	21.45±0.30	15.95±0.40
7	28±1	16±1	28.15±0.60	16.35±0.60	27.95±0.60	16.25±1	27.55±0.50	16.15±0.70
8	34±1	16±1	33.75±0.90	16.75±0.70	34.75±1.50	16.55±1.05	33.55±0.20	16.35±0.90
9	34±1	22±1	32.65±1.20	23.15±1.20	33.35±0.90	23.85±1.20	33.35±0.45	22.75±0.60
10	34±1	28±1	34.25±1.40	29.15±0.90	35.35±1	30.75±1	33.65±0.75	28.55±1.20
11	34±1	34±1	35.75±0.75	35.15±2.10	36.15±0.80	36.35±0.90	34.55±0.75	34.25±1.05
12	28±1	34±1	28.65±1.80	35.35±1.80	29.45±0.90	36.35±0.60	28.25±1.50	34.55±0.90
13	22±1	34±1	23.05±1.40	36.05±1.35	23.45±1.20	37.25±0.60	21.75±1	34.45±1.20
14	16±1	34±1	19.05±1.20	36.75±1.25	16.75±0.70	37.25±0.90	17.75±1.20	35.75±1.25
15	16±1	28±1	17.45±1.05	29.75±1.05	16.55±0.90	31.45±0.80	16.25±1.20	29.15±1.05
16	16±1	22±1	17.15±1.20	21.95±0.75	15.75±1.20	22.25±1.20	15.85±1.20	21.75±0.60
17	10±1	10±1	11.75±1,35	11,15±0,9	9,35±1,2	9,95±0,9	11,45±1,65	9,95±1,05
18	16±1	10±1	17.75±1,35	11,45±1,4	16,65±0,9	10,65±1	16,65±1,35	10,25±1,2
19	22±1	10±1	23,75±1,35	11,05±1,4	23,35±0,9	10,15±0,6	53,35±1	10,65±1
20	28±1	10±1	29,15±1,2	10,95±1,35	29,35±1,2	9,95±1,2	28,25±1,35	9,95±0,9
21	34±1	10±1	33,35±0,9	10,75±1,35	34,15±1,5	9,65±1,2	33,45±0,6	10,25±1,05
22	40±1	10±1	39,95±1,05	9,95±1,35	41,65±1,6	8,95±1,5	39,65±0,6	9,85±1
23	40±1	16±1	40,25±1,2	16,65±1,4	42,25±1,8	16,85±1,2	39,75±0,6	15,95±0,8
24	40±1	22±1	41,45±1,65	22,55±1,05	43,75±1,5	23,25±1,6	40,65±1,4	21,75±0,6
25	40±1	28±1	41,15±1,2	29,45±0,9	42,25±1,5	30,65±1	40,35±0,9	28,55±1,2
26	40±1	34±1	41,35±1,3	35,75±1,35	42,65±1,05	37,55±1,05	40,25±0,9	35,15±1,05
27	40±1	40±1	41,45±1,2	40,85±1,2	40,85±1,8	42,65±1,05	40,25±1,05	39,95±0,6
28	34±1	40±1	35,45±1,2	40,85±1,2	35,45±1,2	43,25±1,05	35,25±1,5	40,05±1,05
29	28±1	40±1	26,75±1,2	41,45±1,2	27,05±1,2	43,75±1	26,75±0,8	40,25±1,05
30	22±1	40±1	22,65±1,05	41,45±1,05	22,15±1,2	43,75±1	31,85±1	40,35±0,7
31	16±1	40±1	18,05±1,3	41,45±1,35	16,55±0,9	43,35±0,8	17,75±1,25	40,25±0,9
32	10±1	40±1	11,75±1,2	41,05±1,2	11,05±1,2	42,55±0,9	11,45±1,4	40,25±1
33	10±1	34±1	10,95±0,9	35,45±1	8,90±1,7	36,45±1	9,95±0,4	33,85±0,9
34	10±1	28±1	10,30±1	28,75±1	9,25±1,8	29,10±1	10,05±0,6	28,15±1
35	10±1	22±1	10,65±1	22,25±1	8,95±2,1	23,15±1,05	9,85±0,8	21,95±0,9
36	10±1	16±1	10,55±0,9	16,95±0,8	9,15±2,1	23,05±1,05	9,85±0,75	16,75±1

TABLE II  
POSITION RESOLUTION (FWHM) FOR DIFFERENT RECONSTRUCTION METHODS AND SECTORS. SECTOR 1 CORRESPONDS TO GREEN PART IN FIG. 3, SECTOR 2 TO RED AND SECTOR 3 TO BLUE PART. BOTTOM PART OF THE TABLE SHOWS THE RESULTS FOR WHOLE PSD

Sector	$X_{MPCA}$ (mm)	$Y_{MPCA}$ (mm)	$X_{Anger}$ (mm)	$Y_{Anger}$ (mm)	$X_{Square}$ (mm)	$Y_{Square}$ (mm)
1	1,15±0.08	1,05±0.08	0,81±0.08	0,90±0.08	1,25±0.08	1±0.08
2	1,13±0.08	1,15±0.08	0,99±0.07	0,91±0.08	0,81±0.08	0,89±0.08
3	1,17±0.08	1,17±0.08	1,42±0.08	1,05±0.08	0,99±0.07	0,95±0.08
PSD	1,15±0.08	1,15±0.08	1,21±0.08	0,99±0.08	0,95±0.08	0,93±0.08

coordinates. The results for this adjustes are shown in Figure 6. The tail in Y profile corresponds to one wrong pixel in this direction.

The average value obtained for both coordinates are  $FWHM_X = 0.95±0.08\text{mm}$  and  $FWHM_Y = 0.93±0.08\text{mm}$  with the best method. This spatial resolution is 5% better than other systems already working with the same aim of SALSA [13] and it is around 30% more than conventional

Resistor-Network systems available now to make medical imaging [14]. Although the best results are obtained for the algorithm for small devices Eq. (2), we emphasize in the MPCA method Eqs. (3,4) since it allows to determine the interaction position without any need of making a projection of the charge distribution inside the PSD. The spatial resolution is not as different as others methods and can be increased with future improvements. The fact of making an individual study

of the charge per pixel is mandatory if a deep study of the scintillator crystal has to be done and if all the features that the IMAR method gives have to be explored.

## V. CONCLUSIONS

We have developed a high spatial resolution  $\gamma$  camera devoted to characterization of electrical response in HPGe segmented detectors. Different algorithms for image reconstruction have been tested obtaining very good spatial resolution values of  $0.95\pm 0.08$  mm for X coordinate and  $0.93\pm 0.08$  mm for Y. Finally, it is noteworthy that this system, given the principle on which it is based, may have promising applications in medical physics.

## ACKNOWLEDGEMENT

The authors would like to thank Dr. César Domingo Pardo for his support during the PSD characterization stage and Diego Barrientos for his work in our laboratory in the beginning of SALSA.

This work has been partially supported by the grants FPA2008-06419, FPA2008-03774 and Consolider CSD2007-00042 by MICINN Spain and GR12 by the Junta de Castilla y León.

## REFERENCES

- [1] Official AGATA homepage: <http://www-w2k.gsi.de/agata>
- [2] Official GRETA homepage: <http://greta.lbl.gov>
- [3] M. Gimnez, J.M Benlloch, et al., Nucl. Inst. Meth. A 525 (2004) 298-302
- [4] Hamamatsu Photonics K.K. [Online]. Available: [http://sales.hamamatsu.com/assets/pdf/parts\\_H/H10966\\_TPMH1319E01.pdf](http://sales.hamamatsu.com/assets/pdf/parts_H/H10966_TPMH1319E01.pdf)
- [5] CAEN S.p.A. [Online]. Available: <http://www.caen.it/>
- [6] R. Barth, Y. Du, H. Essel, R. Fitzsche, H. Gringer, J. Hoffmann, F. Humbert, N. Kurz, R. Mayer, W. Ott, and D. Schall, GSI Multi-Branch System User Manual, GSI Helmholtzzentrum für Schwerionenforschung GmbH Jan. 2000 [Online]. Available: <http://www.win.gsi.de/daq/>
- [7] Creative Electronic Systems-CES. [Online]. Available: <http://www.ces.ch/>
- [8] J. Adamczewski, M. Al-Turany, D. Bertini, H. Essel, and S. Linev, The Go4 Analysis Framework Reference Manual v4.0 GSI Helmholtzzentrum für Schwerionenforschung GmbH, Feb. 2008 [Online]. Available: <http://www-linux.gsi.de/go4>
- [9] R. Brun and F. Rademakers, ROOT An object oriented data analysis framework, Nucl. Instrum. Meth. Phys. Res. A, vol. 389, pp. 8186, Feb. 1997.
- [10] F.C.L. Crespi, F. Camera, Nucl. Inst. and Meth. A 593 (2008) 440-447.
- [11] H. O. Anger, Rev. Sci. Instrum. 29, 27-33, 1958
- [12] R. Pani et al. Nucl. Phys. B (Proc. Suppl.) 197 (2009) 383-386
- [13] César Domingo-Pardo, Namita Goel., IEEE Trans. on Med. Imaging, 28, 12 (2009 ) 2007-2014
- [14] J.M. Benlloch et al. Nucl. Instrum. Meth. Phys. Res. A vol. 504, 232-233 (2003)



# High Spatial Resolution $\gamma$ -Camera Devoted to Characterization of Electrical Response in HPGe Segmented Detectors.

A. Hernández-Prieto, B. Quintana and D. Barrientos

**Abstract**—Characterization of the electrical response of the HPGe segmented detectors is one of the current goals for the Nuclear Physics community in order to perform  $\gamma$ -ray tracking or even imaging with these detectors. For this purpose, scanning devices have to be developed to achieve the signal-position association with the highest precision. In our laboratory, a new scanning system, SALSA, acronym of Salamanca Lyso-based Scanning Array, consisting on a high spatial resolution  $\gamma$  camera is under development. In this work the SALSA system is presented and the results for the characterization of the  $\gamma$  camera are shown.

**Index Terms**—Position Sensitive  $\gamma$ -ray scintillator Detector (PSD), Pixilated Position-Sensitive PhotoMultiplier Tube (PSPMT), Salamanca Lyso-based Scanning Array (SALSA)

## I. INTRODUCTION

The nuclear experiments in the new Radioactive-Ion Beam (RIB) facilities require more efficient and sensitive  $\gamma$ -spectroscopy devices. With this objective a new development has been achieved with Germanium detectors by segmenting the electrical contacts, responsible for collecting the charge carriers released in each photon interaction. The most relevant examples of these detectors can be found in AGATA [1] or GRETA [2] collaborations. This makes it feasible the determination of the interaction point which enables for tracking the  $\gamma$ -ray. But as intermediate step it is necessary to characterize the electrical response of the Germanium crystals with respect to the interaction point of the photon within the crystal. At the same time, to explore in depth the capabilities of Ge segmented detectors as  $\gamma$ -ray tracking detectors, it is mandatory to reach the maximum precision in their characterization. To perform this task, scanning systems which use a radioactive source and ancillary detectors devoted to detect in coincidence with the Ge detector the  $\gamma$  products of the disintegration are used. The most extended systems are based on the mechanical movement of the collimated source with respect to the detector. Their main drawbacks are the long time needed to scan the whole detector and the high activity of the source required. As alternative to this method, the PET principle [3] can be used, for which a Position Sensitive  $\gamma$ -ray scintillator Detector (PSD) capable of determining the 511keV  $\gamma$ -ray directions is needed.

A. Hernández-Prieto and B. Quintana are with the Laboratorio de Radiaciones Ionizantes, University of Salamanca, 37007 SPAIN

D. Barrientos is with the Instituto de Física Corpuscular (IFIC), Valencia, SPAIN

A. Hernández-Prieto contact e-mail: alvaro.prieto@usal.es

In this paper, we are presenting SALSA, the scanning system based on PET, under development in the Laboratorio de Radiaciones Ionizantes of the University of Salamanca. In section II principles and components of our scanning system are exposed. The position interaction reconstruction algorithm is presented in section III. In sections IV and V results of linearity and spatial resolution are exposed.

## II. SCANNING PRINCIPLE

The SALSA set-up is made up of a  $^{22}\text{Na}$  source which provides two simultaneous 511 keV gamma-rays in opposite directions, PSD and the HPGe detector to scan. The PSD consists in four high spatial resolution  $\gamma$ -cameras with a total area of  $104 \times 104 \text{ mm}^2$ , each based on a lutetium yttrium oxyorthosilicate (LYSO) scintillating crystal of  $52 \times 52 \times 5 \text{ mm}^3$ , read-out by a pixilated Position-Sensitive PhotoMultiplier Tube (PSPMT) H10966A-100 from Hamamatsu [4]. Each PSPMT has an output of 64 channels, one per pixel, plus the last dynode signal. In our setup all the channels from the PSD are read. This leads a total of 260 electronic signals in the system. The charge signals from the PSPMT are integrated and digitized by eight V792 Charge-to-Digital Conversion QDC VME modules from CAEN [5]. They have an input range from 0 to 400pC and a digital resolution of 12 bit. In order to read out the 256 QDC channels, the standard acquisition system, MultiBranch System (MBS) [6] is used. This system runs under the Lynx real-time operative system in a VME PowerPC platform RIO4-8072RE 1GHz, from CES [7]. The online and offline analysis were performed via the GSI Object Oriented Online Offline system Go4 [8], based on the ROOT package of CERN [9]. Schematic for whole SALSA system is shown in Fig. 1.

Among all the couples of  $\gamma$  rays produced by the  $^{22}\text{Na}$  source, some of them will be detected in the PSD and in the Ge detector in coincidence. Assuming that the  $\beta^+$  annihilates at rest, the direction of both  $\gamma$  rays in the lab frame is opposite. Therefore, running the system in coincidence mode between PSD and Ge detector and knowing where the  $\gamma$ -ray impacts on the PSD and the position of the  $^{22}\text{Na}$  source, it is possible to determine the direction of the  $\gamma$  ray which impacts in the Ge detector. But to know the interaction position in the Ge detector another scan in a different geometrical configuration of the system has to be performed. By comparing the Ge electric pulses corresponding to crossing directions, it is possible to determine the precise point of interaction

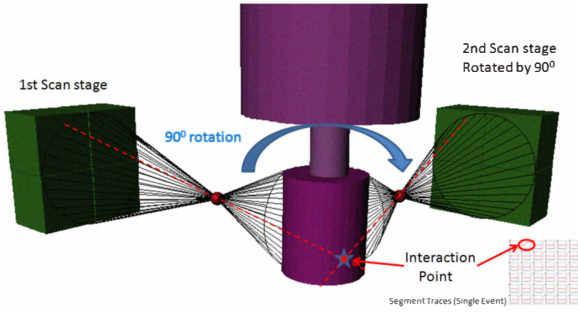


Fig. 1. Schematics for SALSAs. The HPGe detector to scan is presented in purple, whereas the PSDs are in green. the point-like  $^{22}\text{Na}$  source is drawn red, and the  $\gamma$ -cones generated are placed in black

associated to the pulse. Once we have obtained a set of interaction points covering the Ge crystal together with their corresponding electric pulses, Pulse Shape Analysis (PSA) techniques [10] are used in the Ge crystal characterization. For this purpose a high position resolution is needed in the system, in order to determine accurately the direction of the  $\gamma$  ray and, after the characterization process, the precise position of the interaction point in the Ge detector.

### III. IMAGE RECONSTRUCTION ALGORITHM

While the most extended algorithm to reconstruct the image in  $\gamma$  cameras as ours is the one based on Anger's Logic [11], the complete read-out of all the signals in our  $\gamma$  camera allows to explore the possibility of doing a Gaussian fit of the light distribution in the PSD. With this aim, we have developed an algorithm which works in two stages: In the first stage we make a background adjustment and later subtraction in order to remove possible effects of the light reflexion in the edge of the scintillator crystal. Then, we perform a Gaussian fit of the light distribution as shown in Fig. 2. The Gaussian adjustment is performed using linear  $\chi^2$  test algorithm by using the ROOT analysis package [9].

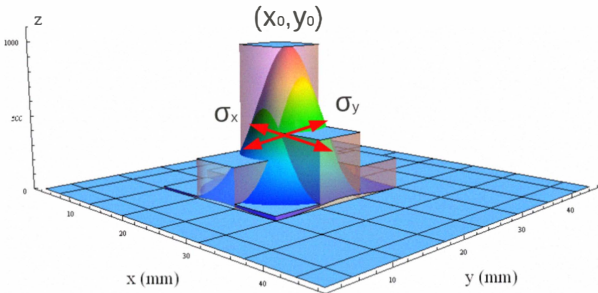


Fig. 2. Light distribution pattern for a particular event in the center of the PSD

In two dimensions, Gaussian equation is as follows

$$f(x, y) = Ae^{-\frac{1}{2}\left(\frac{(x-x_0)^2}{\sigma_x^2} + \frac{(y-y_0)^2}{\sigma_y^2}\right)} \quad (1)$$

This function has five parameters: A,  $x_0$ ,  $\sigma_x$ ,  $y_0$  and  $\sigma_y$ . These parameters correspond with the maximum amplitude

of the light distribution (A), the centroid position in the X direction and the light distribution width in this direction, ( $x_0 \pm \sigma_x$ ) and in Y direction ( $y_0 \pm \sigma_y$ ). As shown in Fig. 2, making the Gaussian fit of the light distribution it is possible to obtain not only the centroid of the Gaussian ( $x_0, y_0$ ), and consequentially the interaction position of one particular event, but also the width of the light distribution ( $\sigma_x, \sigma_y$ ) which is intrinsic to the LYSO crystal. We have performed a set of  $^{22}\text{Na}$  source collimated position measurements around the PSD surface accumulating a set of events and studying the normalized light distribution in different positions. With this information we can obtain a complete characterization of the light response on all the surface of our PSD and, if the light distribution width is constant on it, we can fix  $\sigma_x$  and  $\sigma_y$  values reducing the number of the parameters in the light distribution fit event by event when the system works in a real situation. Fig. 3 shows the impact collimated position in the detector surface. We have analyzed the entire surface of the detector and, in order to know the behavior in problematic pixels such as those placed on edges and corners, we have taken more than one position inside these pixels.

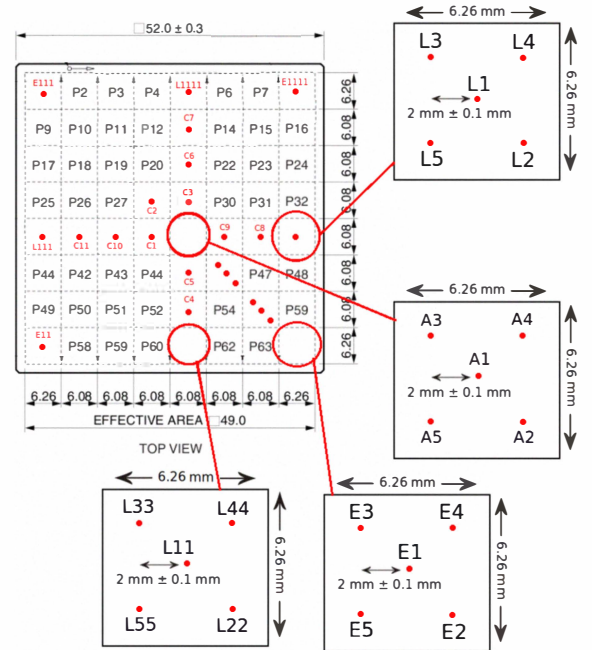


Fig. 3. Pattern of positions where a measurement was made with the collimated source.

### IV. LIGHT DISTRIBUTION CHARACTERIZATION

Making the collimated position adjustment after a set of events, we can evaluate the light distribution width for a particular interaction position. Then if we have several point around the detector surface, and the light distribution width remains constant, we can calculate the main value in order to fix when we make the fit event by event. We show the results obtained in Table I.

TABLE I

TOTAL RESULTS FOR COLLIMATED MEASUREMENTS IN PSD. THE MEAN UNCERTAINTIES ARE CALCULATED WITHOUT CORNER VALUES.

Pos.	$\sigma_X$ (mm)	$\sigma_Y$ (mm)	$\nu$	$\chi^2$
L1111	$3.29 \pm 0.81$	$3.34 \pm 0.94$	2	0.020
C7	$2.98 \pm 0.64$	$3.01 \pm 0.73$	4	0.196
C6	$3.40 \pm 0.75$	$4.13 \pm 1.41$	4	0.246
C3	$3.25 \pm 0.64$	$3.11 \pm 0.67$	4	0.248
A1	$3.31 \pm 0.77$	$2.96 \pm 0.57$	4	0.122
C5	$3.57 \pm 0.81$	$3.39 \pm 0.73$	4	0.238
C4	$3.27 \pm 0.73$	$3.43 \pm 0.98$	4	0.139
L11	$3.91 \pm 1.47$	$3.96 \pm 1.34$	2	0.026
L111	$2.72 \pm 2.16$	$3.49 \pm 0.91$	2	0.117
C11	$3.25 \pm 0.63$	$3.30 \pm 0.65$	4	0.140
C10	$2.85 \pm 0.52$	$2.96 \pm 0.82$	4	0.123
C1	$3.02 \pm 0.57$	$2.84 \pm 0.47$	4	0.227
A1	$3.31 \pm 0.77$	$2.96 \pm 0.57$	4	0.122
C9	$3.41 \pm 0.80$	$2.84 \pm 0.47$	4	0.381
C8	$3.72 \pm 0.73$	$3.08 \pm 0.59$	4	0.384
L1	$2.69 \pm 1.91$	$3.73 \pm 1.13$	2	0.129
C2	$3.61 \pm 1.29$	$3.21 \pm 0.67$	4	0.152
E1	$2.98 \pm 2.91$	$3.18 \pm 3.10$	2	0.088
E11	$3.066 \pm -$	$3.27 \pm -$	2	0.300
E111	$3.18 \pm 1.59$	$3.14 \pm 1.16$	2	0.016
E1111	$3.06 \pm 1.29$	$3.25 \pm 1.62$	2	0.029
Mean Uncertainty	$3.066 \pm 0.941$	$3.279 \pm 0.803$		

We observe an almost constant behaviour of the data on the surface, getting minimum  $\sigma$  values of 2.7 mm and maximum of 3.9 mm with uncertainties of 0.94 mm in X direction and 0.80 mm in Y direction. It is interesting to note that no Depth Of Interaction (DOI) [12] information have been take into account to make this calculation. This will be evaluated on a focused publication. We will use the averaged light distribution width ( $\sigma_x$ ,  $\sigma_y$ ) to fix them in the event fit in order to minimize the centroid calculation uncertainty, and consequential the interaction position for a particular event in the detector.

## V. LINEARITY AND SPATIAL RESOLUTION

Collimated positions have been selected in order to cover the more meaningful locations on the PSD surface, in Fig. 4 we show several reconstructed positions after making Gaussian fit event by event with the light distribution width fixed. This picture shows the capability of our  $\gamma$  camera to reconstruct different positions. The spatial resolution of our  $\gamma$  camera is evaluated from the mean value in the centroid determination uncertainty along the X and Y direction. We have chosen this value because it represents the quality of our fit according to the experimental data given by the  $\gamma$  camera. In Table II, the uncertainty of the centroid determination is presented as minimum, maximum and mean value in both X and Y directions. The main value for the uncertainty in the position determination has a mean value of  $X_{fit} \pm 0.144$  mm in X direction and  $Y_{fit} \pm 0.141$  mm in Y direction. This values are the average ones after several events fit and, as shows in the table, the maximum and minimum values do not keep away from them. It allows us to conclude that the average values are consistent.

The linearity of our PSD is shown in Figure 5 for the collimated measurement. The blue and red points correspond to the linearity values of the system when the read-out of all

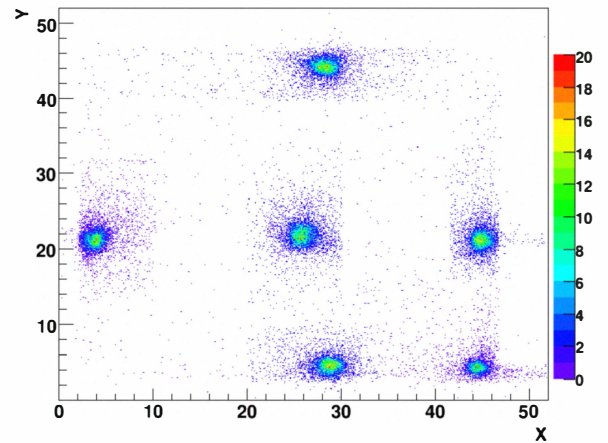


Fig. 4. Contour plots of the positions measured when the collimated source was placed at different locations at the surface of the PSD.

the  $\gamma$  camera signals is used in combination with the light distribution Gaussian fit. When compared with an ideal detector, which is represented in dashed line, it can be concluded that our system behaves linear (1:1) along all the surface of the PSD.

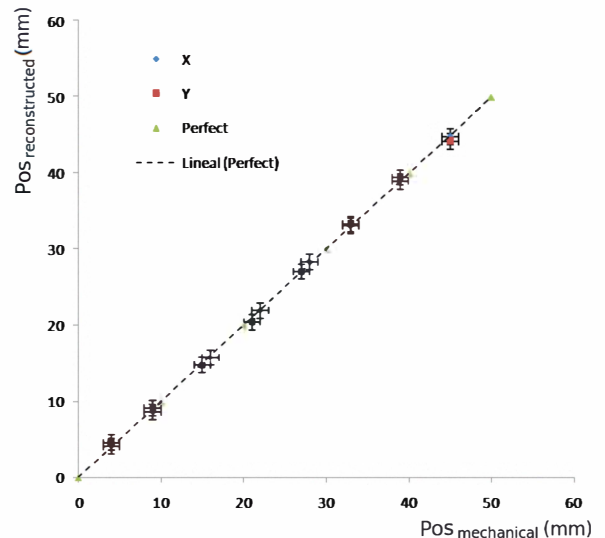


Fig. 5. Linearity of the detection system along the two main axis. The dotted diagonal line illustrates the linearity performance of an ideal detector.

## VI. CONCLUSIONS

We have developed a high spatial resolution  $\gamma$  camera devoted to characterization of electrical response in HPGe segmented detectors. The combination between the read-out of all the  $\gamma$  camera signals and the Gaussian fit of the light distribution gives a very good spatial resolution values of 0.144 mm for X coordinate and 0.141 mm for Y direction. Finally, it is noteworthy that this system, given the principle on which it is based, may have promising applications in medical physics.

TABLE II  
TOTAL RESULTS FOR COLLIMATED MEASUREMENTS IN PSD. THE MEAN UNCERTAINTIES ARE CALCULATED WITHOUT CORNER VALUES.

Pos.	$X_{mec}$ (mm)	$Y_{mec}$ (mm)	$X_{fit}$ (mm)	$Y_{fit}$ (mm)	Min $\sigma_{X_{fit}}$ (mm)	Max $\sigma_{X_{fit}}$ (mm)	Min $\sigma_{Y_{fit}}$ (mm)	Max $\sigma_{Y_{fit}}$ (mm)
L1111	27.0 ± 0.1	45.0 ± 0.1	27.58 ± 0.134	44.34 ± 0.145	0.130	0.138	0.129	0.169
C7	27.0 ± 0.1	39.0 ± 0.1	27.01 ± 0.116	40.41 ± 0.119	0.111	0.119	0.113	0.127
C6	27.0 ± 0.1	33.0 ± 0.1	26.54 ± 0.119	34.04 ± 0.119	0.117	0.123	0.117	0.121
C3	27.0 ± 0.1	29.0 ± 0.1	26.97 ± 0.120	29.11 ± 0.125	0.118	0.123	0.119	0.133
A1	27.0 ± 0.1	23.0 ± 0.1	27.87 ± 0.163	22.69 ± 0.141	0.132	0.194	0.135	0.145
C5	27.0 ± 0.1	15.0 ± 0.1	27.99 ± 0.140	15.79 ± 0.138	0.126	0.154	0.121	0.156
C4	27.0 ± 0.1	9.0 ± 0.1	27.48 ± 0.147	9.75 ± 0.133	0.132	0.161	0.120	0.146
L11	27.0 ± 0.1	4.0 ± 0.1	27.22 ± 0.231	5.27 ± 0.195	0.191	0.268	0.160	0.254
L111	4.0 ± 0.1	22.5 ± 0.1	3.76 ± 0.159	22.64 ± 0.128	0.135	0.182	0.122	0.135
C11	9.0 ± 0.1	22.5 ± 0.1	8.84 ± 0.133	23.02 ± 0.131	0.125	0.145	0.117	0.147
C10	16.0 ± 0.1	22.5 ± 0.1	15.09 ± 0.147	23.10 ± 0.127	0.133	0.163	0.123	0.133
C1	20.0 ± 0.1	22.5 ± 0.1	20.51 ± 0.157	23.51 ± 0.157	0.150	0.162	0.153	0.162
A1	27.0 ± 0.1	23.0 ± 0.1	27.87 ± 0.163	22.69 ± 0.141	0.132	0.194	0.135	0.145
C9	34.0 ± 0.1	22.5 ± 0.1	34.08 ± 0.134	21.79 ± 0.190	0.132	0.136	0.175	0.217
C8	40.0 ± 0.1	22.5 ± 0.1	40.36 ± 0.124	22.09 ± 0.121	0.120	0.128	0.119	0.122
L1	45.0 ± 0.1	22.5 ± 0.1	43.97 ± 0.127	22.47 ± 0.114	0.125	0.128	0.110	0.122
C2	21.0 ± 0.1	28.5 ± 0.1	20.62 ± 0.125	28.69 ± 0.126	0.123	0.127	0.116	0.139
E1	45.0 ± 0.1	4.0 ± 0.1	44.48 ± 0.211	4.73 ± 0.199	0.187	0.219	0.155	0.209
E11	5.0 ± 0.1	5.0 ± 0.1	4.84 ± 0.161	5.53 ± 0.153	0.143	0.190	0.142	0.161
E111	4.0 ± 0.1	45.0 ± 0.1	3.87 ± 0.134	44.01 ± 128	0.131	0.138	0.126	0.129
E1111	45.0 ± 0.1	45.0 ± 0.1	43.39 ± 0.127	44.14 ± 0.131	0.125	0.130	0.129	0.135
Mean			$X_{fit} \pm 0.144$	$Y_{fit} \pm 0.141$				

#### ACKNOWLEDGEMENT

The authors would like to thank Dr. César Domingo Pardo for his advice during the PSD characterization stage of the SALSA system.

This work has been partially supported by the grants FPA2008-06419, FPA2008-03774 and Consolider CSD2007-00042 by MICINN Spain and GR12 by the Junta de Castilla y León.

#### REFERENCES

- [1] Official AGATA homepage: <http://www-w2k.gsi.de/agata>
- [2] Official GRETA homepage: <http://greta.lbl.gov>
- [3] M. Gimnez, J.M Benlloch, et al., Nucl. Inst. Meth. A 525 (2004) 298-302
- [4] Hamamatsu Photonics K.K. [Online]. Available: [http://sales.hamamatsu.com/assets/pdf/parts\\_H/H10966\\_TPMH1319E01.pdf](http://sales.hamamatsu.com/assets/pdf/parts_H/H10966_TPMH1319E01.pdf)
- [5] CAEN S.p.A. [Online]. Available: <http://www.caen.it/>
- [6] R. Barth, Y. Du, H. Essel, R. Fitzsche, H. Gringer, J. Hoffmann, F. Humbert, N. Kurz, R. Mayer, W. Ott, and D. Schall, GSI Multi-Branch System User Manual, GSI Helmholtzzentrum fr Schwerionenforschung GmbH Jan. 2000 [Online]. Available: <http://www.win.gsi.de/daq/>
- [7] Creative Electronic Systems-CES. [Online]. Available: <http://www.ces.ch/>
- [8] J. Adamczewski, M. Al-Turany, D. Bertini, H. Essel, and S. Linev, The Go4 Analysis Framework Reference Manual v4.0 GSI Helmholtzzentrum fr Schwerionenforschung GmbH, Feb. 2008 [Online]. Available: <http://www-linux.gsi.de/go4>
- [9] R. Brun and F. Rademakers, ROOT. An object oriented data analysis framework, Nucl. Instrum. Meth. Phys. Res. A, vol. 389, pp. 8186, Feb. 1997.
- [10] F.C.L. Crespi, F. Camera, Nucl. Inst. and Meth. A 593 (2008) 440-447.
- [11] H. O. Anger, Rev. Sci. Instrum. 29, 27-33, 1958
- [12] J.M. Benlloch et al. Nucl. Instrum. Meth. Phys. Res. A vol. 504, 232-233 (2003)

---

## Chapter 3

# Article 1. Characterization of a High Spatial Resolution $\gamma$ Camera for Scanning HPGe Segmented Detectors

---

Once the reconstruction algorithm to evaluate each  $\gamma$  ray interaction position in the  $\gamma$  camera was decided and SALSA read-out electronics was fully functional, a full characterization of the  $\gamma$  camera used in SALSA was performed. This includes the characterization of the scintillation light shape all around the  $\gamma$  camera, the reconstruction algorithm optimization and the uncertainty in the  $\gamma$  ray interaction position determination in the  $\gamma$  camera detection plane and a final test to test the imaging capability of the camera with one test detector.

Everything was published in the first formal article of this thesis work, so-called *Characterization of a high spatial resolution  $\gamma$  camera for scanning HPGe segmented detectors*. The paper was approved to be published in the journal *IEEE Transactions for Nuclear Science*, volume 60, pages 4719-4726, year 2013).



# Characterization of a High Spatial Resolution $\gamma$ Camera for Scanning HPGe Segmented Detectors

A. Hernández-Prieto, *Student Member, IEEE*, and B. Quintana

**Abstract**—Characterization of the electrical response of HPGe segmented detectors as a function of the interaction position is one of the current goals for the Nuclear Physics community in order to perform  $\gamma$ -ray tracking or even imaging with these detectors. For this purpose, scanning devices must be developed to achieve the signal-position association with the highest precision. With this aim, SALSA, a  $\gamma$ -camera-based scanning system, is under development at our laboratory. In this work, the optimization study aimed to obtain the best spatial resolution in the position-sensitive detectors employed as  $\gamma$  camera is described.

**Index Terms**—LYSO crystal, position sensitive detector (PSD).

## I. INTRODUCTION

THE nuclear experiments to be performed in the new Radioactive-Ion Beam (RIB) facilities require the development of more efficient and sensitive  $\gamma$ -spectroscopy devices. With this objective, coaxial HPGe detectors with highly segmented electrical contacts, which are responsible for collecting the charge carriers released in each photon interaction, are used. Some relevant examples of these detectors can be found in international collaborations such as AGATA [1] or GRETA [2]. Contact segmentation enables us to determine the interaction points of a  $\gamma$  ray inside the Ge crystal, thus providing the data needed to reconstruct the  $\gamma$ -ray track. However, as an intermediate step, it is necessary to characterize the electrical response of the Ge crystal with respect to the position of the interaction point. At the same time, in order to explore in depth the Ge segmented detector capabilities, we have to reach the maximum precision in its characterization. To carry out this task, scanning systems are used. These are based on the measurement of a radioactive source with ancillary detectors devoted to detecting in coincidence those photons which generate a signal in the Ge detector to be characterized. Most scanning systems use the mechanical movement of a collimated source with respect to the detector to determine the  $\gamma$ -ray interaction position in the Ge crystal [3]. Their main drawbacks are the long time needed to scan the whole detector, the high activity required in the source and the

precision limited by the mechanics. However, a virtual collimation [4] becomes an alternative by employing the two co-linear 511-keV photons emitted in the annihilation of the positron [5]. Then, the photon direction must be determined with a Position Sensitive Detector (PSD).

A PSD can be built, for instance, with a scintillator crystal coupled to a Position Sensitive PhotoMultiplier Tube (PSPMT). With such a device, the interaction position of the photon at the scintillator can be determined by using the appropriate algorithm. This type of PSD was originally developed by H. O. Anger [6], whose work is considered as the starting point of modern  $\gamma$  cameras. Concerning his approach, a new milestone was reached with the commercial introduction of small PSPMTs, which enabled the development of very compact miniature gamma cameras [7]. However, other options based on gas-filled detectors have also been studied and proposed for a wide range of applications [8], [9], [10].

Since the original work of H. O. Anger, the readout techniques and the associated image reconstruction algorithms used with scintillators have evolved significantly. A new multi-anode readout method, together with a suitable image reconstruction algorithm, was investigated by Bird *et al.* [11] by using a multi-channel very-large-scale integration (VLSI) charge-sensitive amplifier array. In the same year, Truman *et al.* [12] applied the position-sensitive PMT readout as well as the peak-fitting algorithm, both proposed by Bird *et al.* to pixelated CsI(Tl) arrays, obtaining improved resolutions. Recently, this readout method has been applied to a scanning system based on a virtual collimation, such as the one presented in this paper [13]. Finally, the arrival of the flat-panel-type multi-anode photomultiplier tube [14] afforded large detection areas, allowing new image reconstruction algorithms to be explored by applying neural networks [15] or simply by narrowing the PSPMT signal readout [16].

In the scanning system proposed here, the PSDs are made of continuous lutetium yttrium oxyorthosilicate (LYSO) scintillating crystal [17] and flat-panel PSPMTs, which provide full acquisition of the light distribution produced by the interacting  $\gamma$  rays in the scintillator crystal. Our objective is to improve the accuracy of the interaction position obtained with a large detection area  $\gamma$  camera. With this aim, the algorithms employed to obtain this position are investigated.

Currently, the most common algorithms to determine the  $\gamma$ -ray interaction position in commercial  $\gamma$  cameras are based on the original Anger's Logic [6] or its later improvement [16]. When applied to PSDs using PSPMTs with 64 pixels, such as the ones used in this work, this method enables a reduction in the PSPMT outputs, usually from 64 to 4 outputs per PSPMT.

Manuscript received July 10, 2012; revised January 14, 2013; accepted October 16, 2013. Date of publication November 20, 2013; date of current version December 11, 2013. This work was supported in part by Grants FPA2008-06419 and FPA2008-03774, in part by Consolider CSD2007-00042 by MICINN Spain, and in part by GR12 from the Junta de Castilla y León.

The authors are with the Laboratorio de Radiaciones Ionizantes, University of Salamanca, 37007 Spain (e-mail: alvaro.prieto@usal.es).

Color versions of one or more of the figures in this paper are available online at <http://ieeexplore.ieee.org>.

Digital Object Identifier 10.1109/TNS.2013.2287252

This requires special hardware in the readout stage, consisting of a matrix of resistances. The reduction in the number of outputs is possible because the Anger's Logic works with the signal projections on the X- and Y-axes. However, when 64 outputs are available, calculation of the interaction position using the X- and Y-projections leads to a loss of information regarding the light distribution, which is particularly critical at the edge of the crystal. This effect, associated with the use of Anger's Logic, spoils the resolution of our system, which is actually based on four coupled PSDs.

In this work, we aim to improve the behaviour and the resolution of the four optically coupled PSDs employed in SALSALSA, which work together. This objective requires a study to optimize both the PSPMT readout electronics and the position location algorithm. Regarding the latter, we propose in Section III the application of a Gaussian peak-fitting algorithm to the full experimental light distribution of LYSO crystals based on Least Squares. A similar solution was previously explored by Bird *et al.* [11] and Truman *et al.* [12] but using CsI(Tl) and NaI(Tl) scintillator crystals. Before Section III, our scanning system, together with the details of its  $\gamma$  camera and associated readout electronics, are presented in Section II. Section IV describes the experimental measurements carried out with the scope to characterize the PSDs. In Section V, we examine the results obtained regarding the light distribution response all over the PSD surface. The better we reproduce the light distribution numerically, the lower the uncertainty in the position determination and, therefore, the better the PSD capability to discern different  $\gamma$ -ray interaction points. We also apply these results to evaluate the linearity of the PSD that enables us to offer the obtained resolutions in terms of geometrical distances into the LYSO crystals. In Section VI, some conclusions are given.

## II. DESCRIPTION OF THE $\gamma$ CAMERA

The operation of the SALAMANACA Lyso-based Scanning Array (SALSALSA) is based on the determination of the spatially correlated directions of the two photons following a  $\beta^+\beta$  annihilation. For this purpose, a PSD is needed to detect one of the two photons and to disentangle its interaction position in the PSD, bearing in mind that the lower the position uncertainty, the higher the resolution of the scanner. There is also a contribution to the position determination uncertainty in the PSD which comes from the finite size of the  $^{22}\text{Na}$  source and from the non-collinearity of the two generated 511 keV photons. These two effects are negligible in our system given the short distances between the elements of SALSALSA and the point-like  $^{22}\text{Na}$  source with only 0.25 mm diameter [18]. Accordingly, a  $^{22}\text{Na}$  source that provides two simultaneous 511-keV  $\gamma$  rays in opposite directions and a large detection area PSD with scintillators capable of determining the directions of the 511-keV photons form part of SALSALSA. The  $\gamma$  camera developed to achieve high performance consists of four high-spatial-resolution sets, each one made up of continuous LYSO crystals,  $52 \times 52 \times 5 \text{ mm}^3$  in size. LYSO crystals have a high self activity, mainly from the  $\beta$  decay of the  $^{176}\text{Lu}$  isotope, which represents 2.6% of natural Lu. The usual LYSO intrinsic backgrounds are around  $260 \text{ counts s}^{-1} \text{ cm}^{-3}$ , as can be seen, together with the specific characteristics of LYSO crystals, in the work of Pídol *et al.* [17].

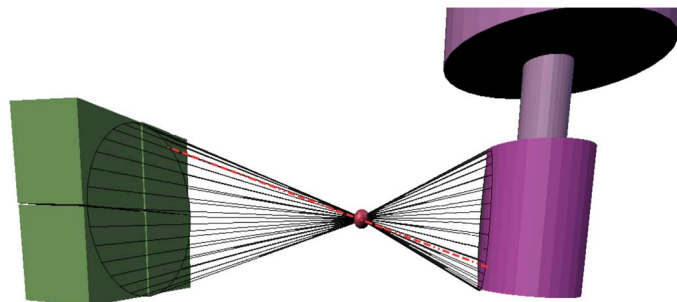


Fig. 1. Schematics for SALSALSA. The HPGe detector to be scanned is shown in purple, whereas the  $\gamma$  camera is depicted in green. The point-like  $^{22}\text{Na}$  source is drawn red.

The choice of the crystal thickness was done by performing a Monte Carlo simulation, looking for a balance between high peak-to-total ratios at 511 keV and low probability of full photon-energy absorption by multiple interactions at 511 keV, which enhances the signal of interest against the ones due to multiple interactions that spoil the position resolution of the LYSO crystals. Thicknesses from 3 mm up to 10 mm were implemented in the MC simulations. A thickness of 5 mm is considered a good agreement, providing a peak-to-total ratio (P/T) at 511 keV of 16% and a peak efficiency at 511 keV of 12.8%, both calculated from the simulated total spectrum corresponding to a  $^{22}\text{Na}$  source. The readout of the crystal is performed with a position-sensitive photomultiplier tube (PSPMT) model H10966A-100 by Hamamatsu. Each PSPMT has an output of 64 channels, one per pixel, plus an additional channel corresponding to the last dynode signal. In our configuration, all channels coming from each PSPMT are read. This affords 260 electronic signals, providing a  $104 \times 104 \text{ mm}^2$  total detection area. The optical coupling of the four LYSO-PSPMT sets is made in the same X-Y plane, as shown in Fig. 1. In SALSALSA, the  $^{22}\text{Na}$  source is located between the PSDs and the HPGe detector, as also shown in Fig. 1.

In order to integrate and digitize the 260 electronic signals coming from the PSDs, they were AC-coupled into eight model V792 charge-to-digital conversion (QDC) VME modules from CAEN, having an input range from 0 to 400 pC and a digital resolution of 12 bits. The readout of the 260 QDC channels from the PSPMT anodes and dynodes is achieved via the MultiBranch System (MBS) [19]. This system runs under the Lynx-real-time operative system in a VME PowerPC platform RIO4-8072RE 1 GHz from CES [20]. The online and offline analyses are performed using the Object Oriented Online Offline system Go4 [21], based on the ROOT package of CERN [22]. Other modules are fast leading-edge discriminators (LED) model N840 from CAEN, timing-filter amplifiers TFA-474 from ORTEC and gate-and-delay generators model GG8020 also from ORTEC. The schematic of the electronics is shown in Fig. 2, where the logic process aimed at ensuring the coincidence between the PSDs and the scanned detector is also indicated.

Although the same high voltage is applied to all the anodes of a PSPMT, a different response is obtained in terms of signal amplification. This causes distortions in the image reconstruction algorithm. To solve this problem, the individual anode readout is

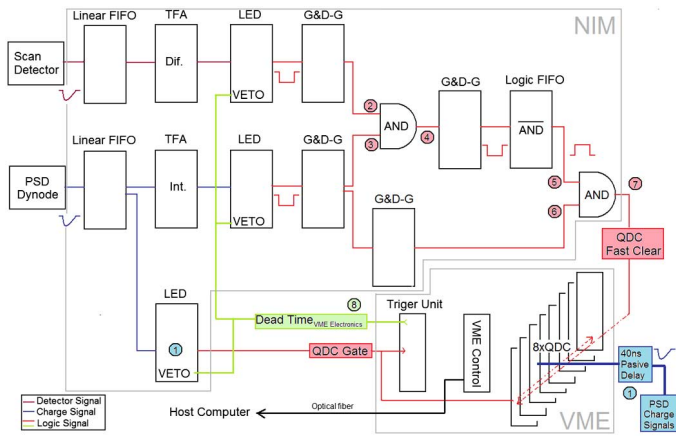


Fig. 2. Schematics for SALSA electronic set-up.

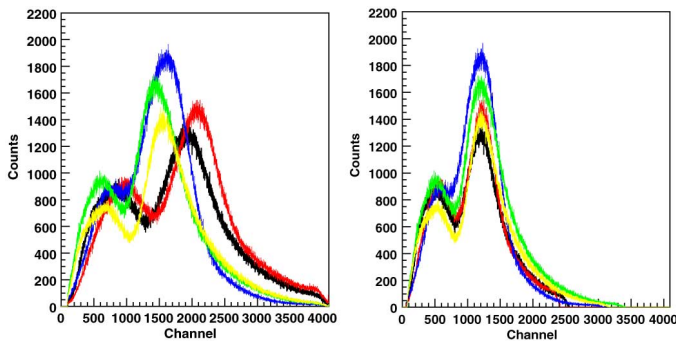


Fig. 3. On the left, the raw QDC pulse height spectra for five representative anodes. On the right, the pulse height spectra after calibration.

used in order to correct the gain deviation between anodes. The required adjustment will ensure a homogeneous response along the whole  $\gamma$  camera surface, as can be seen in Fig. 3, where only 4 channels are shown in order for the graphics to be more understandable.

To perform the anode gain matching, the  $\gamma$  camera was fully illuminated using the same 1-MBq  $^{22}\text{Na}$  source as the one used in the scanning measurements. In this way, no additional source is needed to carry out the procedure. Measurements were performed with the source placed between the PSD and a NaI(Tl) detector, the PSD-to-source and source-to-NaI(Tl) distances being 72.4 mm and 75.0 mm, respectively. The purpose of the NaI(Tl) detector is to perform measurements with the system's coincidence electronics (Fig. 2), taking advantage of the optimization already performed for the scanning measurements. The fact that the  $\gamma$ -camera's data acquisition runs in coincidence with the NaI(Tl) detector also reduces background due to the LYSO self-activity peak at 508.66 keV. This peak is due to the true-coincidence summing of two in-cascade emissions from  $^{176}\text{Lu}$ : the 201.83-keV and 306.82-keV ones. As far as the scanning procedure is concerned, these events are measured by the  $\gamma$  camera in the same energy window as the 511-keV ones, spoiling the reliability of the characterization. Count rates at 508.66-keV of 0.87 counts  $\text{s}^{-1}$  are obtained in the  $\gamma$  camera with the coincidence electronics against a count rate of 66 counts  $\text{s}^{-1}$  without coincidences. Presumably, the use of coincidences brings some disadvantages to the

anode gain matching procedure because of the reduction of the 1274.57-keV peak area. However, this peak is not even observed in the anode spectra without coincidences, which let us match the anode gains just with the 511-keV peak. The count rate at 1274.57 keV recorded at the dynode without coincidences is 0.11 counts  $\text{s}^{-1}$ , which gives rise to a number of counts in the anodes lower than the detection limit at this energy. The count rate at 1274.57 keV in the  $\gamma$  camera dynode spectrum measured in coincidence is 0.05 counts  $\text{s}^{-1}$ , which causes count rates in the anodes lower than the detection limit. The 1274.57-keV peak is seen just in the dynode in ideal conditions. A peak efficiency at 1274.57 keV of 1.1% is obtained against a value of 11.9% at 511 keV when the  $^{22}\text{Na}$  source is collimated and its emissions impinge in a central anode of the PSD. Therefore, only the 511-keV peak was used to determine the gain factor corresponding to each anode. Taking into account that the 511-keV peak is the one used in the image reconstruction, this did not represent a severe setback. Gain factors were obtained relative to a reference value, given by one of the anodes. After the anode gain matching has been accomplished, the  $\gamma$  camera is ready to operate. The right part of Fig. 3 shows the calibrated spectra.

### III. POSITION LOCATION ALGORITHM

SALSA takes advantage of both the continuous scintillator crystals of the  $\gamma$  camera and the complete readout of all the signals coming from the scintillators. By exploring the two-dimensional (2D) shape of light distribution in the PSDs, the later determination of the position interaction event by event can be achieved by performing a fit to a parametric shape function with an optimized number of parameters. To reduce the number of fitting parameters, a previous characterization of the light distribution is done. To characterize the light distribution of our  $\gamma$  camera, an algorithm was developed, which proceeds as follows:

- In a first stage, a background fit and its further subtraction from the experimental data is performed in order to remove possible effects due to both the light reflectivity on the edges of the scintillator crystal and the electronic noise.
- In a second stage, a fit of a parametric Gaussian function to the net experimental distribution is carried out. The selection of the Gaussian function is purely empirical, based on the observation of the experimental light distribution provided by each of the pixels. Then, a statistical test is applied to check if the model and experimental data differ. The fitting was accomplished using ROOT's implementation of the TMinuit minimization algorithm [23].

The Gaussian function used to shape the light distribution is as follows:

$$f(x, y) = Ae^{-\frac{1}{2} \left( \frac{(x-x_0)^2}{\sigma_x^2} + \frac{(y-y_0)^2}{\sigma_y^2} \right)}. \quad (1)$$

This function has five parameters:  $A$ ,  $x_0$ ,  $\sigma_x$ ,  $y_0$  and  $\sigma_y$ . These parameters correspond, respectively, to the maximum amplitude of the light distribution, the  $x$  coordinate of the centroid position, the light distribution width in the  $x$  direction, the  $y$  coordinate of the centroid position and the light distribution width along the  $y$  direction. With the Gaussian function given in (1),

the light distribution is assumed to have X- and Y- axes as symmetry axes, both being parallel to the crystal edges and each one orthogonal with respect to the other. By using this Gaussian function, it is possible to obtain not only the centroid of the Gaussian,  $(x_0, y_0)$  and, as a consequence, the interaction position in the  $\gamma$ -camera plane, but also the light distribution width  $(\sigma_x, \sigma_y)$ .

The output of the fit consists of the parameter values together with their uncertainties. The uncertainties are obtained from the parameter covariance matrix,  $\{c(a_i, a_j), i, j = 1, \dots, n\}$ , where  $a_i$  and  $a_j$  are, respectively, the  $i$ th and  $j$ th fitting parameter and  $n$  is the total number of parameters. The covariance matrix's diagonal terms corresponding to the parameters  $x_0$  and  $y_0$  provide the uncertainty in the  $\gamma$ -ray interaction position in the  $\gamma$  camera. This uncertainty, together with the uncertainty in the  $\beta^+$  annihilation position within the  $^{22}\text{Na}$  source, determines the total uncertainty of the position inside the HPGe segmented detector.

Since the method described in this work allows us to obtain not only shape but also light distribution width, it is possible to study, after a set of events for different positions, whether width remains constant over all the  $\gamma$ -camera surface or not. If so, the  $\sigma_x$  and  $\sigma_y$  values can be fixed, reducing the number of parameters in the light distribution fit of an individual event. Position determination is done event by event when the characterization system scans a HPGe detector; therefore, such a reduction contributes to decreasing uncertainty in the position parameters.

#### IV. EXPERIMENTAL METHOD

The  $^{22}\text{Na}$  source was placed in different collimated positions in order to acquire the set of measurements needed to characterize the light distribution response in the  $\gamma$  camera. For this task, a 1-mm-hole and 50-mm-length lead collimator coupled to a high precision X-Y support, which allows the entire surface of each PSD to be covered, was used. The distance between the face of the collimator and the PSD was 12 mm, affording a 1.48-mm spot due to the divergence of the beam. The collimated position pattern employed in the measurements of each individual PSD is shown in Fig. 4. Pixels are identified by the row and column labels shown in this figure. Note that at this stage each PSD has been characterized independently. In order to clarify the results presented in this work, the serial number of the PSDs: ZK0021, ZK0084, ZK0065 and ZK0079, are used to identify each of them independently.

Measurements in each collimator position were carried out by running the system in coincidence mode between the PSD and a NaI(Tl) detector. Once a set of  $10^6$  events have been accumulated, the normalized light distribution corresponding to each position was obtained, together with the associated standard deviation.

#### V. RESULTS

##### A. Light-Distribution Characterization

The Gaussian function of Eq. (1) is fitted to the normalized light distributions obtained at each collimator position. Fig. 5

	C1	C2	C3	C4	C5	C6	C7	C8
R1	*	*	*	* *	*	*	*	*
R2	*	*	*	*	*	*	*	*
R3	*	*	*	*	*	*	*	*
R4	*	*	*	*	*	*	*	*
R5	* *	*	*	* * * *	*	*	*	* *
R6	*	*	*	*	*	*	*	*
R7	*	*	*	*	*	*	*	*
R8	*	*	*	* *	*	*	*	* *

Fig. 4. Pattern of positions where a measurement was made with the collimated source.

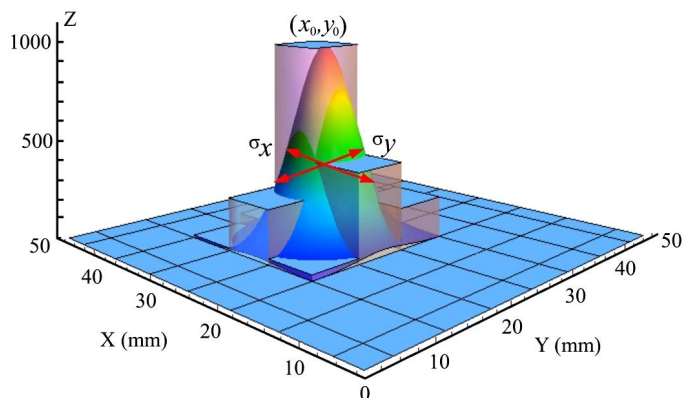


Fig. 5. Experimental light distribution represented by cuboids corresponding to a particular position on the X-Y plane of the ZK0021 PSD. The fitted distribution is also shown by a smooth Gaussian shape.

shows an illustrative Gaussian fit for a particular position in the centre of one the PSDs.

With all the fits done to the light distributions measured at different pixels, the assumption that the X- and Y-axes are the symmetry axes can be checked. In Table I,  $\sigma_x$  values are given for positions (pixels) with constant values of the Y-coordinate (see Fig. 4). In Table II, the  $\sigma_y$  values are shown corresponding to pixels with a constant X-coordinate (see also Fig. 4). The values given in Table I do not differ statistically. The same is the case of the values given in Table II. Therefore,  $\sigma_x$  and  $\sigma_y$  kept constant along the X- and Y-axes which shows that they can be taken as symmetry axes of the light distribution. If light distribution had other symmetry axes, the distribution width projected on X- and Y-axes should change gradually.

Given that the method proposed to obtain the interaction position relies on the light-distribution fit to a Gaussian function in which  $\sigma_x$  and  $\sigma_y$  are constant, it is necessary to select the best estimation of these widths. Therefore, a statistical study is required to decide what values to take. We constructed the experimental probability distribution of both  $\sigma_x$  and  $\sigma_y$  by taking their values from the the light-distribution fits corresponding to

TABLE I  
VALUES FOR  $\sigma_x$  WHEN THE X-COORDINATE ( $22.0 \pm 0.1$  MM) REMAINS  
CONSTANT AND THE Y-COORDINATE VARIES

Pixel	Y-coordinate (mm)	$\sigma_x$ (mm)
R8C4	4	$3.71 \pm 0.11$
R7C4	10	$3.62 \pm 0.49$
R6C4	16	$3.25 \pm 0.86$
R5C4	20	$3.35 \pm 0.11$
R4C4	28	$3.55 \pm 0.91$
R3C4	34	$3.23 \pm 0.72$
R2C4	40	$3.85 \pm 0.99$
R1C4	46	$3.27 \pm 0.20$
MEAN VALUE		$3.45 \pm 0.73$

TABLE II  
VALUES FOR  $\sigma_y$  WHEN THE Y-COORDINATE ( $22.0 \pm 0.1$  MM) REMAINS  
CONSTANT AND THE X-COORDINATE VARIES

Pixel	X-coordinate (mm)	$\sigma_y$ (mm)
R5C1	4	$3.69 \pm 0.10$
R5C2	10	$3.02 \pm 0.81$
R5C3	16	$3.64 \pm 0.13$
R5C4	20	$3.47 \pm 0.06$
R5C5	28	$3.11 \pm 0.76$
R5C6	34	$3.09 \pm 0.86$
R5C7	40	$3.44 \pm 0.71$
R5C8	46	$3.66 \pm 0.38$
MEAN VALUE		$3.38 \pm 0.29$

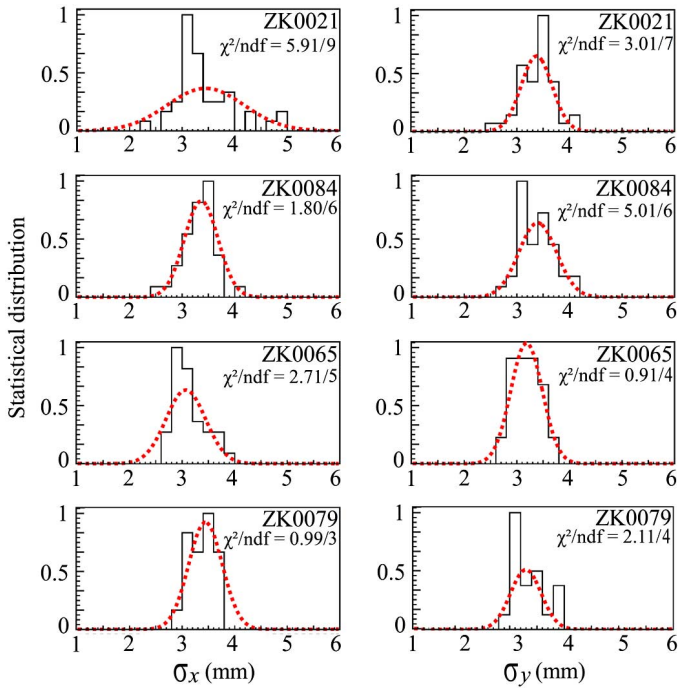


Fig. 6. Frequency diagrams corresponding to the light distribution width in each PSD for the different collimator positions. On the left, the  $\sigma_x$  component and, on the right, the  $\sigma_y$  component.  $\chi^2/\text{ndf}$  represents the  $\chi^2$  statistic value per degrees of freedom.

all the collimated positions for each PSD. The values are represented in a histogram grouping all the  $\sigma$  values in 0.2-mm intervals. The number of bars depends on the data dispersion. To characterize this statistical distribution, we compared it, by a  $\chi^2$  test, with a Gaussian function because in this case the average

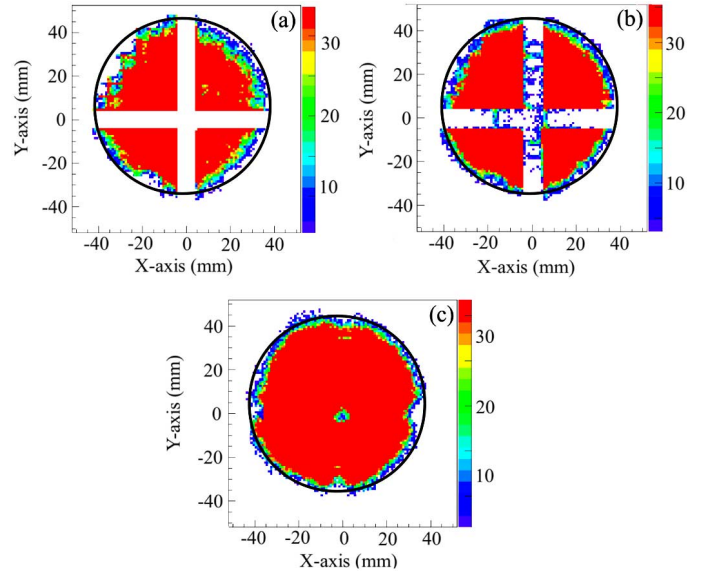


Fig. 7. Images of the coincidence NaI(Tl) detector using our four PSDs as  $\gamma$  camera obtained when the position interaction in the NaI(Tl) X-Y plane is calculated with (a) the Anger's Logic algorithm, (b) the Gaussian fit without fixing the light distribution width and (c) the Gaussian fit fixing the light distribution width. The real outline of the NaI(Tl) detector is drawn in black.

TABLE III  
MEAN LIGHT-DISTRIBUTION WIDTHS FOR EACH PSD

$\gamma$ -camera	$\sigma_x$ (mm)	$\sigma_y$ (mm)
ZK0021	$3.45 \pm 0.73$	$3.38 \pm 0.29$
ZK0084	$3.36 \pm 0.32$	$3.39 \pm 0.36$
ZK0065	$3.07 \pm 0.37$	$3.18 \pm 0.30$
ZK0079	$3.44 \pm 0.32$	$3.30 \pm 0.28$

value corresponds to the maximum likelihood value. Additionally, with this test we check the random nature of the fluctuation of the  $\sigma_x$  and  $\sigma_y$  widths. If the fluctuation was random, the distribution mean value would correspond to the most probable value. The results are shown in Fig. 6.

The mean values associated with the statistical distributions for each  $\sigma_x$  and  $\sigma_y$  component together with their uncertainties are given in Table III. These values will be fixed in order to reduce the number of free parameters in the light distribution Gaussian fit when performed event by event, i.e. with SALSA working in a real situation. This allows not only a reduction in the uncertainty of the centroid determination but also an increase in the useful field of view in the PSD, which becomes a solution for the blind zones that appear in the junctions between each PSD.

Fig. 7 shows the images corresponding to the X-Y plane of the NaI(Tl) detector when it is fully illuminated with the  $^{22}\text{Na}$  source and compares them with the real outline. These images were acquired with the four PSDs working together as a  $\gamma$  camera. In (a) the data acquired were treated with Anger's Logic algorithm. The blind zone is clearly visible between the PSDs due to the poor behaviour of the algorithm at the edge of the scintillator crystal. Blind zones start being filled and the field of view increases in (b), where the Gaussian fit of the light distribution is applied event by event without fixing the light distribution width with respect to (a). In (c) the blind zone is

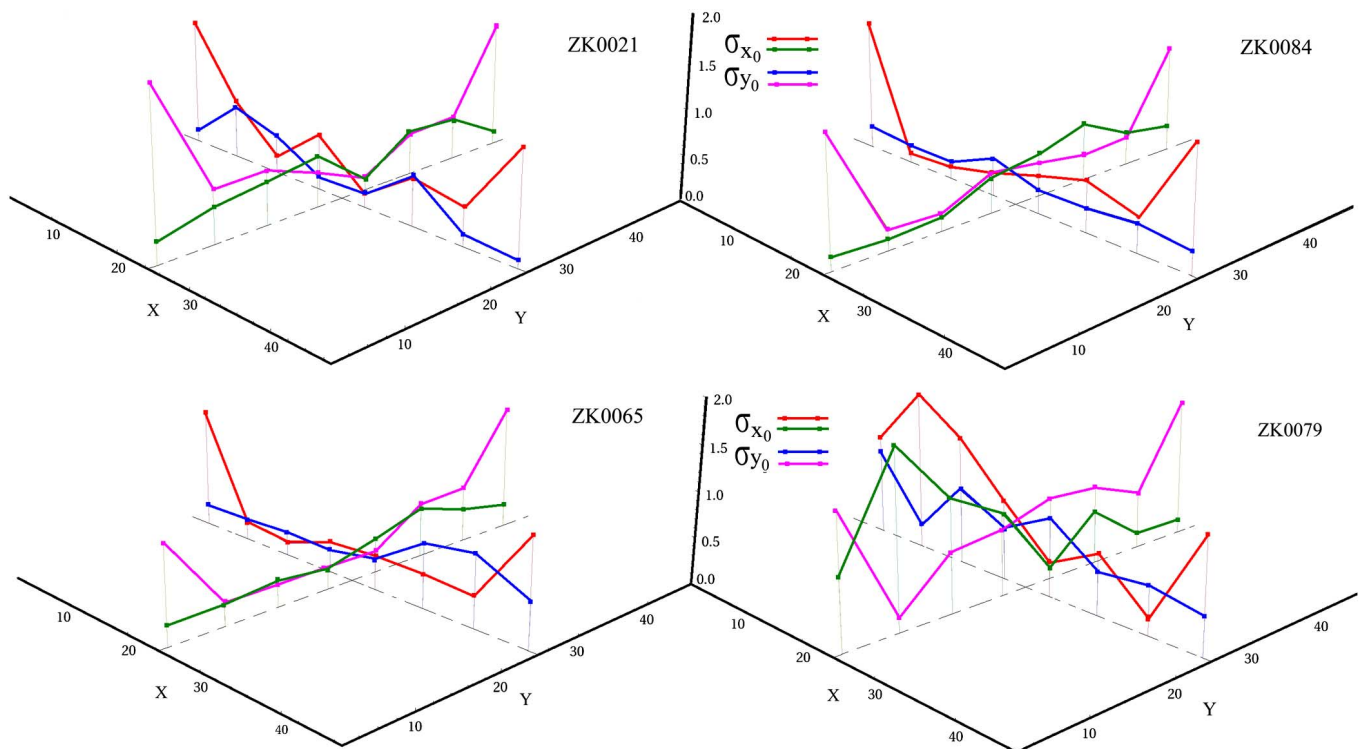


Fig. 8. Experimental uncertainties in the centroid determination  $\sigma_{x_0}$  (purple) and  $\sigma_{y_0}$  (blue) obtained for each PSD versus the collimated positions for a particular scanning direction in which the Y-coordinate is kept constant. The same uncertainties but for a scanning direction in which the X-coordinate is now kept constant are depicted in green for  $\sigma_{x_0}$  and brown for  $\sigma_{y_0}$ .

strongly suppressed when the light distribution width is fixed in the Gaussian fit with the values given in Table III, and the field of view is maximum.

### B. Spatial Resolution

The uncertainty values for the centroid determination of the normalized light distribution,  $\sigma_{x_0}$  and  $\sigma_{y_0}$ , in the four PSD surfaces provide the spatial resolution of the  $\gamma$  camera. The ensemble of values obtained for the different collimated interaction positions on the X-Y plane of the  $\gamma$ -camera were studied.

As seen in Fig. 8, we observe that the uncertainty  $\sigma_{x_0}$  worsens when approaching the edge of the  $\gamma$  camera for a scanning direction in which the Y-coordinate of the collimated points is kept constant and the X-coordinate varies between the two edges of the crystal. However,  $\sigma_{y_0}$  remains almost constant. This situation can be understood graphically in Fig. 9(a) which shows that when approaching the X edge the experimental data set corresponds to a light distribution partially acquired for the X component. The same effect, but for a scanning direction in which the X-coordinate of the collimated points is kept constant and the Y-coordinate varies from one edge of the crystal to the other, is observed for  $\sigma_{y_0}$ . As shown in Fig. 8, the  $\sigma_{x_0}$  values remain almost constant while the  $\sigma_{y_0}$  ones worsen when reaching the edge of the Y-coordinate of the crystal. Fig. 9(b) shows how that light distribution is incompletely acquired for the Y component.

The mean values and, therefore, the spatial resolution of each PSD are shown in Table IV. The goodness-of-fit parameter remains constant at  $\simeq 1$  throughout the central regions of the

TABLE IV  
MEAN VALUES FOR THE UNCERTAINTIES IN THE LIGHT DISTRIBUTION CENTROID DETERMINATION ALL OVER THE SURFACE OF EACH PSD

$\gamma$ -camera	X-axis		Y-axis	
	$\sigma_{x_0}$ (mm)	$\sigma_{y_0}$ (mm)	$\sigma_{x_0}$ (mm)	$\sigma_{y_0}$ (mm)
ZK0021	0.65	0.36	0.28	0.73
ZK0084	0.59	0.33	0.27	0.56
ZK0065	0.54	0.32	0.42	0.58
ZK0079	0.95	0.74	0.61	0.87

PSDs, and rises consistently to  $\simeq 1.5$  in the corner and edge regions. In Table V the  $\sigma_{x_0}$  and  $\sigma_{y_0}$  averaged values are presented separately for the central and edge zones in the PSDs. The uncertainties remain practically constant over the whole surface of the PSD except in the problematic edges, the X-axis for the  $\sigma_{x_0}$  component and the Y-axis for  $\sigma_{y_0}$  one, as shown in Fig. 8.

### C. Linearity

Linearity allows us to check what the final quality of our images will be, since we relate the real positions to the reconstructed ones through linearity. From the measurements acquired at the collimated positions, we tested the linearity of each PSD. In Fig. 10, mechanical positions are plotted versus the reconstructed ones, together with the line representing the ideal behaviour. One can see that the behaviour of our  $\gamma$  camera is practically ideal since the reconstructed positions are in very good agreement with the mechanical ones. The mean and maximum deviations for X- and Y-coordinates and for each PSD are listed in Table VI.

TABLE V  
AVERAGED VALUES IN THE CENTRAL AND EDGE AREAS OBTAINED IN THE LIGHT DISTRIBUTION CENTROID DETERMINATION FOR EACH PSD

$\gamma$ -camera	X-axis (Centre)		X-axis (Edges)		Y-axis (Centre)		Y-axis (Edges)	
	$\sigma_{x_0}$ (mm)	$\sigma_{y_0}$ (mm)						
ZK0021	0.43	0.42	1.32	0.19	0.33	0.44	0.11	1.61
ZK0084	0.31	0.36	1.40	0.22	0.28	0.31	0.25	1.31
ZK0065	0.30	0.34	1.25	0.24	0.43	0.37	0.37	1.22
ZK0079	0.71	0.66	1.18	0.48	0.58	0.67	0.69	1.49

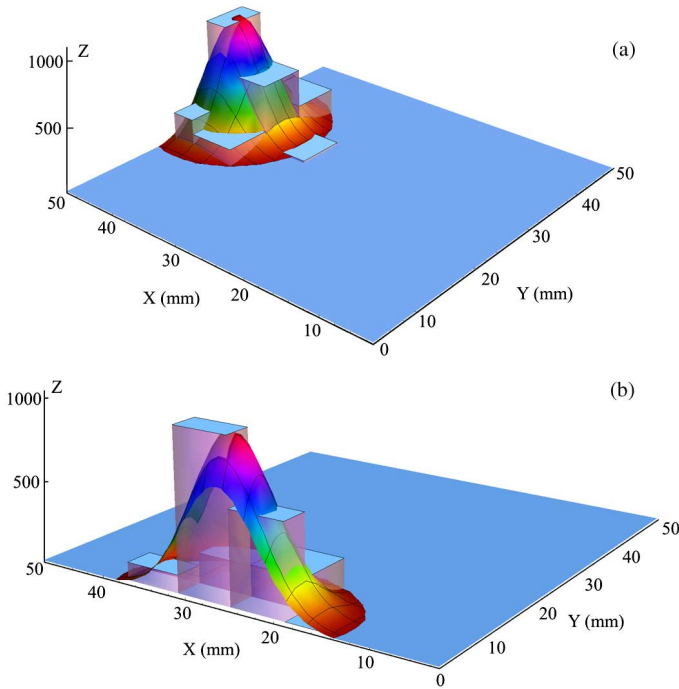


Fig. 9. Light distribution Gaussian fit with an incomplete set of experimental points when the interaction position is close to the edge of the PSD; (a) at the X-axis border and (b) at the Y-axis border.

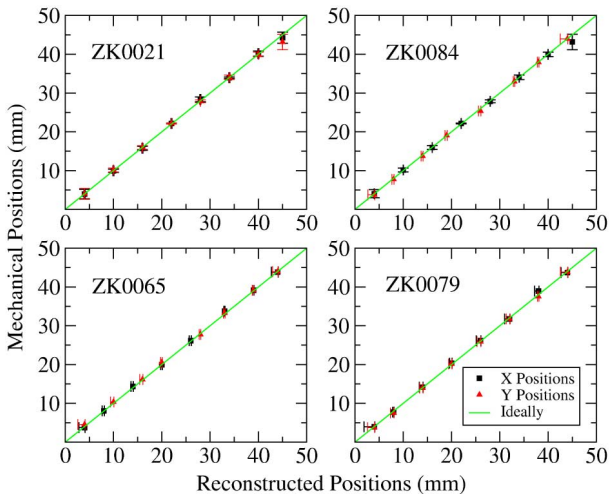


Fig. 10. X- and Y-coordinates of the mechanical positions versus X- and Y-coordinates of the reconstructed ones for the four PSDs. The green diagonal line illustrates the linearity performance of an ideal detector.

#### D. Point Spread Function

Another discussion concerning the spatial resolution of our detector is the Point Spread Function (PSF) [24], measured as

TABLE VI  
MEAN AND MAXIMUM DEVIATION VALUES BETWEEN THE MECHANICAL AND RECONSTRUCTED POSITIONS FOR EACH PSD

$\gamma$ -camera	Mean deviation (mm)		Maximum deviation (mm)	
	X-coord.	Y-coord.	X-coord.	Y-coord.
ZK0021	0.28	0.31	0.75	1.35
ZK0084	0.31	0.20	1.25	0.65
ZK0065	0.24	0.29	0.75	0.55
ZK0079	0.30	0.23	0.95	0.45

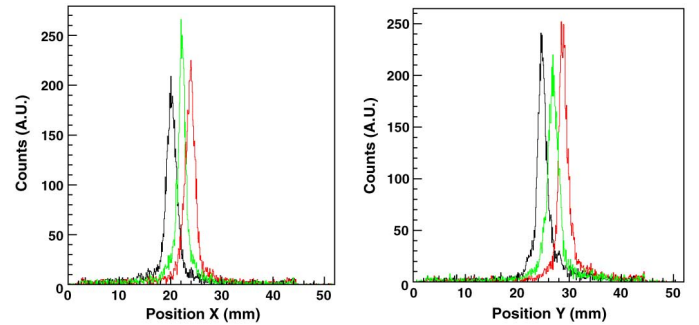


Fig. 11. On the left the distribution of positions  $x$  for the three positions inside the pixel. On the right the distribution of positions  $y$  for these three positions. A set of  $10^6$  events are used for each position.

the FWHM of the distribution of positions  $x$  and  $y$ . This quantity measures the ability of the system to distinguish between closely spaced centroids. In order to determine this value we used the collimated measurements described in Section IV. Fig. 11 shows an example of the distribution of positions  $x$  and  $y$  obtained from the Gaussian fit when we move the collimated source in 2-mm steps inside a single central pixel. The response to these movements can clearly be seen, both, along X- and Y-directions.

On average, we measured position distributions with a FWHM = 1.8 mm and FWHM = 1.9 mm for positions along the X- and Y-axis, respectively. A preliminary study concerning this topic can be found in a previous reference [25]. It is important to indicate that the results presented in this section correspond to the FWHM of the projection along the X and Y axes of the Point Spread Function. In this case we determine the interaction position event by event in the  $\gamma$  camera plane, obtaining one spot per collimated position after a set of events. The projection of this spot along the X and Y axes is the one shown in Fig. 11. We then calculate the FWHM and these are the results described in this section. This concept is different to the one presented in Table III, where we are talking about the light distribution width. As explained in Section V.A, in that case we accumulated the light distribution shapes of  $10^6$  events

and we normalized it afterwards. From this normalized light distribution we calculated the light distribution width from the Gaussian fit. This value is then fixed when the system works in a real situation, determining the interaction position event by event, such as for instance the situation presented here or in Fig. 7(c).

## VI. CONCLUSION

In the current work, the study carried out on the performance of a  $\gamma$  camera made up of four PSDs with an individual anode readout proves that the light distribution has a Gaussian shape over the whole surface of the system with a constant width. The algorithm developed, based on the Gaussian fit to the experimental light distribution, provides sub-milimetric precision in the determination of the interaction position. In comparison to Anger's Logic, our algorithm enhances the field of view area, improving the quality of the image and maintaining a high performance even at the edges of the object to be scanned. We consider it to be shown as an alternative to Anger's Logic when a pixelated  $\gamma$  camera is used.

## ACKNOWLEDGMENT

The authors would like to thank Dr. C. Domingo Pardo for his support during the development stage and D. Barrientos for his work at our laboratory at the beginning of SALSA.

## REFERENCES

- [1] AGATA, "Advanced gamma tracking array," *Nucl. Instrum. Meth. Phys. Res. A*, vol. 668, pp. 26–58, 2012.
- [2] Official GRETA homepage [Online]. Available: <http://greta.lbl.gov>
- [3] M. Dimmock *et al.*, "Validation of pulse shape simulations for an AGATA prototype detector," *IEEE Trans. Nucl. Sci.*, vol. 56, no. 4, pp. 2415–2425, Aug. 2009.
- [4] P. Suetens, *Fundamentals of Medical Imaging*. Cambridge, U.K.: Cambridge Univ. Press, 2009, ch. 5.
- [5] C. Domingo-Pardo *et al.*, "A novel gamma-ray imaging method for the pulse-shape characterization of position sensitive semiconductor radiation detectors," *Nucl. Instrum. Meth. A*, vol. 643, pp. 79–88, 2011.
- [6] H. O. Anger, *Rev. Sci. Instrum.*, vol. 29, pp. 27–33, 1958.
- [7] N. J. Yasillo, R. N. Beck, and M. Cooper, "Design considerations for a single tube gamma camera," *IEEE Trans. Nucl. Sci.*, vol. 37, no. 2, pp. 609–615, Apr. 1990.
- [8] G. Charpak and F. Sauli, "Multiwire proportional chambers and drift chambers," *Nucl. Instrum. Meth.*, vol. 162, pp. 405–428, 1979.
- [9] R. A. Boie *et al.*, "High resolution X-ray gas proportional detectors with delay line position sensing for high counting rates," *Nucl. Instrum. Meth.*, vol. 201, pp. 93–115, 1982.
- [10] B. Yu *et al.*, "Position sensitive gas proportional detectors with anode blades," *IEEE Trans. Nucl. Sci.*, vol. 46, no. 3, pp. 338–341, Jun. 1999.
- [11] A. J. Bird, Z. He, and D. Ramsden, "Multi-channel readout of crossed-wire anode photomultipliers," *Nucl. Instrum. Meth. Phys. Res. A*, vol. 348, pp. 668–672, 1994.
- [12] A. Truman and A. J. Bird *et al.*, "Pixelated CsI(Tl) arrays with position-sensitive PMT readout," *Nucl. Instrum. Meth. Phys. Res. A*, vol. 353, pp. 375–378, 1994.
- [13] C. Domingo-Pardo *et al.*, "A position sensitive GAMMA-Ray scintillator detector with enhanced spatial resolution, linearity, and field of view," *IEEE Trans. Med. Imag.*, vol. 28, no. 12, pp. 2007–2014, Dec. 2009.
- [14] R. Pani *et al.*, "Recent advances and future perspectives of position sensitive PMT," *Nucl. Instrum. Meth. Phys. Res. B*, vol. 213, pp. 197–205, 2004.
- [15] R. J. Aliaga *et al.*, "Corrected position estimation in PET detector modules with multi-anode PMTs using neural networks," *IEEE Trans. Nucl. Sci.*, vol. 53, no. 3, pp. 776–783, Jun. 2006.
- [16] R. Pani *et al.*, "High spatial and energy resolution gamma imaging based on LaBr3(Ce) continuous crystals," presented at the IEEE Nuclear Sci. Symposium Conference Record NM2-7, 2008.
- [17] L. Pidol *et al.*, "High efficiency of lutetium silicate scintillators, Ce-doped LPS, and LYSO crystals," *IEEE Trans. Nucl. Sci.*, vol. 51, no. 3, pp. 1084–1087, Jun. 2006.
- [18] Eckert and Ziegler, Co. Sources for Medical Imaging [Online]. Available: <http://www.ezag.com/home/products/isotope-products>
- [19] R. Barth, Y. Du, H. Essel, R. Fitzsche, H. Gringer, J. Hoffmann, F. Humbert, N. Kurz, R. Mayer, W. Ott, and D. Schall, "GSI multi-branch system user manual," *GSI Helmholtzzentrum Schwerionenforschung GmbH*, Jan. 2000 [Online]. Available: <http://www.win.gsi.de/daq/>
- [20] Creative Electronic Systems-CES [Online]. Available: <http://www.ces.ch/>
- [21] J. Adamczewski, M. Al-Turany, D. Bertini, H. Essel, and S. Linev, "The Go4 analysis framework reference manual v4.0," *GSI Helmholtzzentrum Schwerionenforschung GmbH*, Feb. 2008 [Online]. Available: <http://www-linux.gsi.de/go4>
- [22] R. Brun and F. Rademakers, "ROOT. An object oriented data analysis framework," *Nucl. Instrum. Meth. Phys. Res. A*, vol. 389, pp. 81–86, 1997.
- [23] [Online]. Available: <http://root.cern.ch/root/html/TMinuit.html>
- [24] W R. Hendee and E. Russell, *Medical Imaging Physics*, 4th ed. ed. Hoboken, NJ: Wiley, 2003.
- [25] A. Hernandez-Prieto *et al.*, "Towards a deep characterization of a 64-fold-pixelated position sensitive detector for a new scanning system of HPGe segmented detectors," presented at the 2nd Int. Conf. Advancements in Nuclear Instrumentation Measurement Methods and their Applications (ANIMMA), 2011.

---

## Chapter 4

# Article 2. Study of accuracy in the position determination with SALSA, a $\gamma$ -scanning system for the characterization of segmented HPGe detectors

---

The last step, when both, the  $\gamma$  camera and its reconstruction algorithm were fully characterized and optimized, was to characterize all the sources of uncertainty in SALSA. All of them will contribute to the total uncertainty of SALSA. The total uncertainty of SALSA is the uncertainty when SALSA determines the  $\gamma$  ray interaction position within the HPGe crystal volume during an experimental characterization of the electrical response of such a detector.

The optimization of this total uncertainty was the main goal of this thesis work and the obtained results for different type of HPGe detectors were presented in the last article published during the thesis, so-called *Study of the accuracy in the position determination with SALSA, a  $\gamma$ -scanning system for the characterization of segmented HPGe detectors*. It was published in the journal *Nuclear Instruments and Methods in Physics Research A*, volume 823, pages 98–106, year 2016.

This article also includes the results of the validation of SALSA, made with an alternative method in order to compare the results obtained during the first characterization of a HPGe detector with SALSA.





Contents lists available at ScienceDirect

# Nuclear Instruments and Methods in Physics Research A

journal homepage: [www.elsevier.com/locate/nima](http://www.elsevier.com/locate/nima)

## Study of accuracy in the position determination with SALSA, a $\gamma$ -scanning system for the characterization of segmented HPGe detectors

A. Hernandez-Prieto<sup>a,\*</sup>, B. Quintana<sup>a</sup>, S. Martìn<sup>a</sup>, C. Domingo-Pardo<sup>b</sup><sup>a</sup> Laboratorio de Radiaciones Ionizantes, Departamento de Física Fundamental, Universidad de Salamanca, C/Espejo s/n, Salamanca, Spain<sup>b</sup> Instituto de Física Corpuscular, C/Catedrático José Beltrán, 2, Paterna, Spain

### ARTICLE INFO

#### Article history:

Received 19 December 2014

Received in revised form

21 February 2016

Accepted 31 March 2016

Available online 6 April 2016

#### Keywords:

 $\gamma$ -Camera

Virtual collimation

Salamanca Lyso-based Scanning Array

(SALSA)

Segmented HPGe detectors

### ABSTRACT

Accurate characterization of the electric response of segmented high-purity germanium (HPGe) detectors as a function of the interaction position is one of the current goals of the Nuclear Physics community seeking to perform  $\gamma$ -ray tracking or even imaging with these detectors. For this purpose, scanning devices must be developed to achieve the signal-position association with the highest precision. With a view to studying the accuracy achieved with SALSA, the Salamanca Lyso-based Scanning Array, here we report a detailed study on the uncertainty sources and their effect in the position determination inside the HPGe detector to be scanned. The optimization performed on the design of SALSA, aimed at minimizing the effect of the uncertainty sources, afforded an intrinsic uncertainty of  $\sim 2$  mm for large coaxial detectors and  $\sim 1$  mm for planar ones.

© 2016 Elsevier B.V. All rights reserved.

### 1. Introduction

The new  $\gamma$ -ray position sensitive HPGe detectors are essential tools to perform  $\gamma$  spectroscopy at the new Radioactive-Ion Beam (RIB) facilities. The main improvement in these devices is achieved by the high segmentation of their electrical contacts, which are responsible for collecting the charge carriers released in each photon interaction. Some relevant examples of these detectors can be found in international collaborations such as AGATA [1] or GRETA [2]. High-contact segmentation enables the interaction points of a  $\gamma$  ray inside the HPGe crystal to be determined, thereby providing the data needed to reconstruct the  $\gamma$ -ray track. However, as an intermediate step, it is necessary to characterize the electrical response of the HPGe crystal with respect to the position of the interaction point. At the same time, in order to explore in depth the capabilities of segmented HPGe detector, maximum precision in its characterization must be achieved. SALSA, which is the acronym of the Salamanca Lyso-based Scanning Array, was designed specifically to reduce the sources of uncertainty involved in the position determination inside the HPGe crystal. This determination is based on virtual collimation [3], where two collinear 511-keV photons emitted in the annihilation of a positron are

used. This method also needs a Pulse Shape Analysis Comparison (PSAC) algorithm [4] to achieve the three-dimensional (3D) position determination in the HPGe detector to be scanned. Previous characterization devices based in the same principles as SALSA have been developed and tested [5,6].

The optimized design of SALSA, aimed at improving the final accuracy, consists of a high-spatial-resolution  $\gamma$  camera with large field of view and a point-like  $^{22}\text{Na}$  source, both mounted on a high-precision mechanical structure which allows to make  $90^\circ$  rotations of the whole  $^{22}\text{Na}$  source and  $\gamma$  camera around the HPGe detector to scan and also to adjust the distance between  $^{22}\text{Na}$  source and detector in order to reduce the influence of the uncertainty sources in the calculation of position.

Here, we analyse the design of the scanning system in detail, together with its sources of uncertainty and how these determine the total uncertainty of the final position in the HPGe crystal. The effect of distance between detectors and  $^{22}\text{Na}$  source is evaluated through the uncertainty values obtained for different detectors: an AGATA-type highly segmented coaxial HPGe detector and a segmented planar prototype designed for the DESPEC experiment [7]. First, however, in Section 2 we shall describe SALSA, introducing its components. In Section 3, the algorithm utilized to calculate the interaction position inside the HPGe detector as a function of known parameters is discussed. In Section 4 the global system of reference in SALSA is defined and all the elements placed on it.

\* Corresponding author.

E-mail address: [alvaro.prieto@usal.es](mailto:alvaro.prieto@usal.es) (A. Hernandez-Prieto).

In Sections 5 and 6 the uncertainties inherent to both,  $^{22}\text{Na}$  source and  $\gamma$  camera are evaluated. In Section 7, the total uncertainty provided by SALSA in position determination is calculated for the cases of interest. In Section 8, an experimental validation of position determination and its corresponding uncertainty evaluation is performed with a conventional HPGe detector. Finally, in Section 9, we offer some conclusions.

## 2. The SALSA setup

As mentioned above, the main elements of SALSA are a high-spatial-resolution  $\gamma$  camera, a point-like  $^{22}\text{Na}$  source and the mechanical platform supporting these two elements together with the detector to be scanned. All these elements, together with the associated electronics, aim to obtain the HPGe electric signals, each one associated to an interaction point within the HPGe crystal. Therefore, the main challenge of SALSA is to determine the real interaction points with minimum uncertainty. The radioactive source used generates two 511 keV  $\gamma$  rays coming from the annihilation of the  $\beta^+$  emitted in the disintegration of the  $^{22}\text{Na}$  with a nearby electron. The source is provided by Eckert and Ziegler Company [8] and it consists of a  $^{22}\text{Na}$  (0.125-mm-radius spherical active volume) with a nominal activity of 1 MBq, encapsulated in a 25.4-mm-diameter disk made with carbon epoxy fibre. Its small active volume and the encapsulation are suitable for achieving maximum accuracy in the initial positioning of the  $\gamma$  rays generated in the source. The  $\gamma$  camera is placed in front of the  $^{22}\text{Na}$  source to measure one of the 511 keV  $\gamma$  rays generated in each  $e^-e^+$  annihilation. It consists of four high-spatial-resolution detectors coupled optically, each one made up by a continuous lutetium yttrium oxyorthosilicate (LYSO) scintillating crystal [9],  $52 \times 52 \times 5 \text{ mm}^3$  size. The readout of each crystal is performed by a pixelated position-sensitive photomultiplier tube (PSPMT) from Hamamatsu, model H10966A-100. The junction of the four crystals provides a large field of view ( $104 \times 104 \text{ mm}^2$ ) suitable for scanning, in just one shot, large-sized HPGe detectors with no detriment to accuracy. Their role is to provide the interaction point of the 511 keV  $\gamma$  ray in the  $\gamma$  camera detected in coincidence with the other 511 keV  $\gamma$  ray interacting in the HPGe crystal. This point in the  $\gamma$  camera is referred to as  $(X_L, Y_L, Z_L)$ . Subsequently, the direction of the  $\gamma$  ray detected is determined using this point and the generation point of the two  $\gamma$  rays in the  $^{22}\text{Na}$  source. The latter is referred to as  $(X_S, Y_S, Z_S)$  and is generally located inside the  $^{22}\text{Na}$  source, as demonstrated below. Both points correspond to the same reference system, which is placed in the centre of the detector to be scanned.

Assuming that the  $\beta^+$  particle annihilates at rest, the incident direction of the  $\gamma$  ray interacting in the HPGe crystal can be obtained from the direction of the  $\gamma$  ray detected in the  $\gamma$  camera. The non-collinearity of the two photons resulting from the  $e^-e^+$  annihilation has been studied by several authors [10,11]. The dimensions of SALSA, given below, and the high energy resolution of HPGe detectors allow us to disregard its effect. Therefore, the direction of the  $\gamma$  ray interacting in the HPGe crystal will be given by the straight line defined by the two cited points, which are shown in Fig. 1, satisfying the following well-known equation:

$$\frac{X - X_S}{X_L - X_S} = \frac{Y - Y_S}{Y_L - Y_S} = \frac{Z - Z_S}{Z_L - Z_S} \quad (1)$$

The structure that attaches  $^{22}\text{Na}$  source and  $\gamma$  camera, linking one to the other in the same branch and allowing them to be placed in a common reference system, is the SALSA mechanical structure. Fig. 2 shows the complete SALSA setup when scanning a BEGe detector.

This structure enables us to scan a HPGe crystal from two different positions, called  $S_1$  and  $S_2$ . These two positions are needed to obtain a single point of interaction in the HPGe crystal and not just one direction. Fig. 1 graphically shows the two scanning positions of SALSA. All the elements employed in the SALSA support platform were made at high-precision machining workshops. The  $\gamma$  camera housing and the  $^{22}\text{Na}$  source support structure are machined with 0.2 mm and 0.1 mm precision, respectively. The structure to locate the linear and circular motion circuit and the HPGe detector was from Hepcomotion® [12]. For this structure, MCS® aluminium profiles with 0.1 mm precision cuts were employed. In order to construct a motion circuit, the PRT<sup>2</sup> technology also from Hepcomotion® was used. It allows the  $^{22}\text{Na}$  source and  $\gamma$  camera set to be moved around the HPGe detector with high accuracy from the so-called  $S_1$  scan stage to the  $90^\circ$  rotated  $S_2$  one.

Fig. 3 shows the layout of both the linear and circular motion circuits. The mechanical structure enables the distance both between  $^{22}\text{Na}$  source and  $\gamma$  camera and between  $^{22}\text{Na}$  source and HPGe detector to be adjusted.  $^{22}\text{Na}$  source and  $\gamma$  camera are placed on two carriages that can move linearly with respect to each other on the same branch. Once distances are adjusted, the carriages are blocked and the set can rotate ( $90 \pm 0.03^\circ$ ) in order to change the scanner position from  $S_1$  to  $S_2$ . In SALSA,  $^{22}\text{Na}$  source and  $\gamma$  camera have their own relative reference system. The one corresponding to the  $^{22}\text{Na}$  source is defined at the geometrical centre of its active volume and a position located on it is denoted as  $(X_S'', Y_S'', Z_S'')$ . The one corresponding to the  $\gamma$  camera is defined at the geometrical centre of its detection plane and a point located on it is denoted as

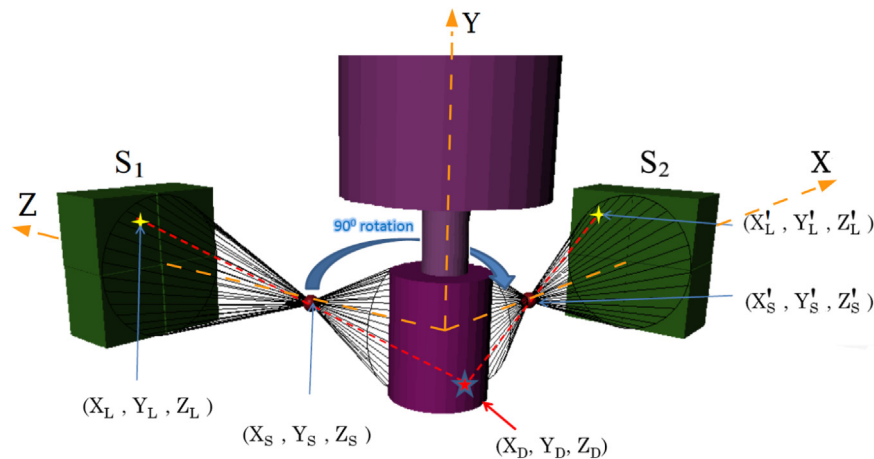


**Fig. 1.** Schematic for SALSA. The HPGe detector to scan is depicted in purple, whereas the  $\gamma$  camera is in green. The point-like  $^{22}\text{Na}$  source is drawn red and the  $\gamma$  cones generated are in black. (For interpretation of the references to colour in this figure caption, the reader is referred to the web version of this paper.)

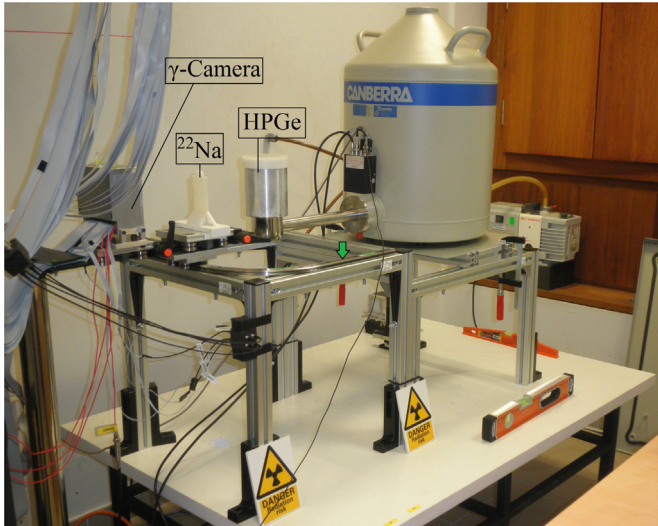


**Fig. 2.** Picture of SALSA with a BEGe detector placed to be scanned. The  $\gamma$ -camera and  $^{22}\text{Na}$  source are set in the scan position  $S_1$ . The second scan stage  $S_2$  is indicated by a green arrow. The rest of the elements of SALSA are also pointed in the picture. (For interpretation of the references to colour in this figure caption, the reader is referred to the web version of this paper.)

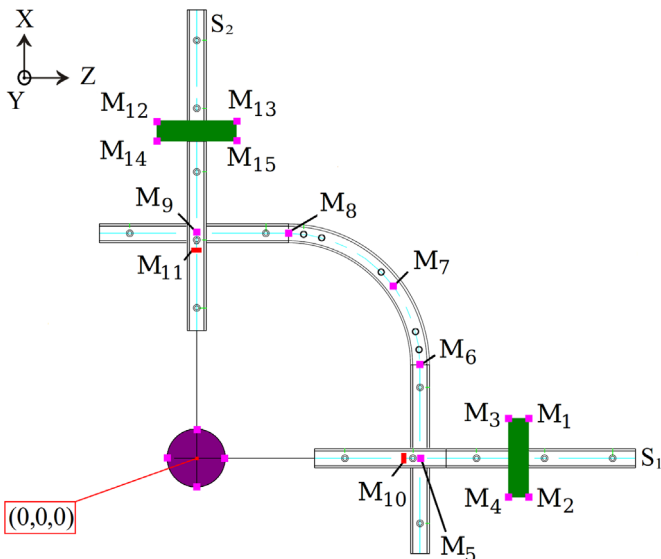


**Fig. 3.** Schematics of the SALSA mechanics. All vertical marks obtained are indicated for both  $S_1$  and  $S_2$  positions. In green the  $\gamma$  camera is represented while the red colour indicates the  $^{22}\text{Na}$  source support. The scanned detector is also placed in the schema. (For interpretation of the references to colour in this figure caption, the reader is referred to the web version of this paper.)

$(X_L^s, Y_L^s, Z_L^s)$ .

However, the positions of interest in these two elements must be referred to the global SALSA reference system. This is achieved by a translation, and hence it is necessary to determine the mechanical positions of  $^{22}\text{Na}$  source and  $\gamma$  camera in the mechanical structure with respect to the global system of reference. At the same time, uncertainties in the positioning of the two elements must be evaluated. These uncertainties correspond both to the mechanical accuracy and to the method employed to measure the absolute positions of the different elements of the mechanics. For the  $Y$  coordinate, a set of measurements of the vertical mark of each SALSA component was done using a Leica Total Station TPS1200, which has a precision of 0.7 mm/km. Since the measurements were taken by looking at a 0.25 mm calibrated rule, this is assumed to be the accuracy of these measurements. The

**Table 1**

Measured vertical dimension mark in different points in SALSA.

Position	Vertical mark (mm)	Mean value (mm)
$M_5$	$395.90 \pm 0.25$	$M_{MEC} = 395.80 \pm 0.25$
$M_6$	$395.80 \pm 0.25$	
$M_7$	$395.80 \pm 0.25$	
$M_8$	$395.80 \pm 0.25$	
$M_9$	$395.70 \pm 0.25$	
$M_1$	$175.80 \pm 0.25$	$M_H = 175.85 \pm 0.25$
$M_2$	$175.90 \pm 0.25$	
$M_3$	$175.80 \pm 0.25$	
$M_4$	$175.90 \pm 0.25$	
$M_{10}$	$238.30 \pm 0.25$	$M_S = 238.30 \pm 0.25$
$M_{11}$	$238.30 \pm 0.25$	
$M_{12}$	$176.00 \pm 0.25$	$M_H = 175.95 \pm 0.25$
$M_{13}$	$175.90 \pm 0.25$	
$M_{14}$	$176.00 \pm 0.25$	
$M_{15}$	$175.90 \pm 0.25$	

different measurements made are shown in Fig. 3 and their results listed in Table 1. With  $M_1$  up to  $M_4$  we refer to the measurements taken on the top of the  $\gamma$  camera housing in  $S_1$ . The measurements taken on several points of the motion circuit go from  $M_5$  to  $M_9$ . With  $M_{10}$  and  $M_{11}$ , we refer to the measurements taken on the  $^{22}\text{Na}$  source support in  $S_1$  and  $S_2$ . Finally,  $M_{12}$ ,  $M_{13}$ ,  $M_{14}$  and  $M_{15}$  correspond to the four vertical marks located on the top of the  $\gamma$  camera housing when placed in  $S_2$ . For every set of measurements the mean value is calculated, being its uncertainty driven by systematic uncertainty introduced by the inaccuracy in the vertical mark measurements. This data is used in Section 4, where the translation from the different coordinate systems to the global one is determined.

### 3. Principles of the position determination in SALSA

The first step in the position determination is to calculate the incident directions of the  $\gamma$  rays in the HPGe crystal, using Eq. (1) together with the interaction position in the  $\gamma$  camera  $(X_L, Y_L, Z_L)$  and the annihilation point in the  $^{22}\text{Na}$  source  $(X_S, Y_S, Z_S)$ . This is performed first in the so-called  $S_1$  configuration, which provides a set of  $\gamma$ -ray tracks, each with a certain associated electrical response in the HPGe crystal. Then, the  $^{22}\text{Na}$  source plus  $\gamma$  camera system is rotated  $90^\circ$  around the HPGe detector axis to the so-called  $S_2$  configuration, where another set of  $\gamma$ -ray tracks is obtained, together with their associated electrical responses in the HPGe crystal. In  $S_2$ , the  $\gamma$ -ray interaction position into the  $\gamma$  camera is denoted as  $(X_L^s, Y_L^s, Z_L^s)$ , while the position of the generation point of the two  $\gamma$  rays is referred to as  $(X_S^s, Y_S^s, Z_S^s)$ , as seen in Fig. 1. Consequently, the direction of the  $\gamma$ -path in  $S_2$  will be defined by a straight line equation given by Eq. (1) but replacing the points corresponding to  $S_1$  by their equivalent ones in  $S_2$ . The electrical response associated to each track correspond to an unknown interaction point in the HPGe placed on the track. In order to obtain this interaction point accurately, two tracks, one in each configuration, that enclose the same interaction point in the HPGe detector must be found by using all the data from  $S_1$  and  $S_2$ . To decide that two tracks correspond to the same interaction point, it is necessary to compare the two electrical responses associated to each track statistically. The design of the HPGe segmented detectors ensures that every position in the crystal will give a unique

electrical response by looking not only at the segment where the gamma has interacted, but also at the surrounding ones. The induced signals in the neighbouring segments allow us to distinguish where the  $\gamma$  ray has interacted within the segment [1]. The statistical comparison is achieved by the PSAC algorithm developed in our laboratory which uses a Wilcoxon signed-rank test [13]. Once checked, the crossing point of the two tracks in  $S_1$  and  $S_2$  corresponding to the same interaction point in the HPGe crystal, which is referred to as  $(X_D, Y_D, Z_D)$ , is obtained from the following two equations:

$$\frac{(X_D - X_S)}{(X_L - X_S)}(Z_L - Z_S) + Z_S = \frac{(X_D - X'_S)}{(X'_L - X'_S)}(Z'_L - Z'_S) + Z'_S \quad (2)$$

$$\frac{(Z_D - Z_S)}{(Z_L - Z_S)}(Y_L - Y_S) + Y_S = \frac{(Z_D - Z'_S)}{(Z'_L - Z'_S)}(Y'_L - Y'_S) + Y'_S. \quad (3)$$

Solving this set of equations, the crossing point is obtained as:

$$X_D = \frac{\frac{X_S(Z_L - Z_S)}{X_L - X_S} - Z_S + Z'_S - \frac{X'_S(Z'_L - Z'_S)}{X'_L - X'_S}}{\frac{(Z_L - Z_S)}{X_L - X_S} - \frac{(Z'_L - Z'_S)}{X'_L - X'_S}} \quad (4)$$

$$Z_D = \frac{(X_D - X_S)}{(X_L - X_S)}(Z_L - Z_S) + Z_S \quad (5)$$

$$Y_D = \begin{cases} \frac{(Z_D - Z_S)}{(Z_L - Z_S)}(Y_L - Y_S) + Y_S & \text{(Line1)} \\ \frac{(Z_D - Z'_S)}{(Z'_L - Z'_S)}(Y'_L - Y'_S) + Y'_S & \text{(Line2)} \end{cases} \quad (6)$$

From Eqs. (4) and (5),  $X_D$  and  $Z_D$  are calculated. Eq. (6) constitutes the geometrical condition to determine the paths from  $S_1$  and  $S_2$  which correspond to the same interaction point inside the HPGe crystal  $(X_D, Y_D, Z_D)$ . Additionally, a further check is made to this solution: the point must be located in the HPGe crystal.

Regarding the uncertainty associated with the position determination of the interaction point in the HPGe crystal, it is assumed that a negligible uncertainty is introduced by the PSAC algorithm as shown in Section 8. Consequently, the uncertainty in the determination of this point will mainly come from the data needed to calculate the two crossing tracks: the position of the interaction point in the  $\gamma$  camera and the position of the annihilation point within the  $^{22}\text{Na}$  source, both in  $S_1$  and  $S_2$ .

#### 4. Determination of the coordinates in the SALSA global reference system

To solve Eqs. (4)–(6), the points corresponding to the interaction point in the  $\gamma$  camera  $(X_L, Y_L, Z_L)$  in  $S_1$  and  $(X'_L, Y'_L, Z'_L)$  in  $S_2$ , and to the  $^{22}\text{Na}$  source emission point,  $(X_S, Y_S, Z_S)$  in  $S_1$  and  $(X'_S, Y'_S, Z'_S)$  in  $S_2$ , must be calculated. The calculation involves the translation of these points initially obtained in the reference systems of the  $\gamma$  camera and the  $^{22}\text{Na}$  source to a common one. The global reference system chosen for SALSA has its origin in the centre of the HPGe crystal and defined by the SALSA mechanical structure (see Fig. 1). The reference system of the  $^{22}\text{Na}$  source has its origin at the geometrical centre of its active volume, which corresponds to  $(X_{S0}, Y_{S0}, Z_{S0})$  in the global reference system. Likewise, the reference system of the  $\gamma$  camera is defined at the geometrical centre of its detection plane and is referred to as  $(X_{CO}, Y_{CO}, Z_{CO})$  in the global reference system. The translation requires the translation vectors from the individual reference systems to the global one to

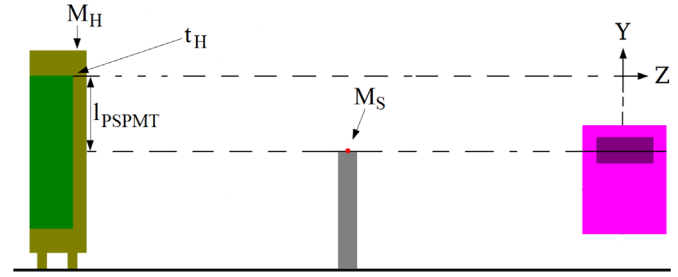


**Fig. 4.** Lateral view of SALSA mechanics. From left to right, the  $\gamma$  camera, the  $^{22}\text{Na}$  source and the HPGe crystal. For the  $\gamma$  camera, the brown colour indicates the housing and the green one the  $\gamma$  camera itself. The red colour is used for the  $^{22}\text{Na}$  source and grey one for its support. (For interpretation of the references to colour in this figure caption, the reader is referred to the web version of this paper.)

be known, but this simply involves calculating the coordinates of the origin of each local reference system in the global one.

Starting with the Y coordinate, a set of measurements was performed with the total station described in Section 2. Since the level measurements are relative to external components, some calculations must be made in order to evaluate the Y coordinate of both the centre of the  $\gamma$  camera and the  $^{22}\text{Na}$  source. In Fig. 4, the position of the marks on the  $\gamma$  camera and  $^{22}\text{Na}$  source are indicated. For the  $\gamma$  camera, the magnitudes that link the marks with its centre are also shown.

As can be seen in Fig. 4, the Y coordinate regarding of the centre of the  $\gamma$  camera ( $Y_{CO}$ ) can be obtained as follows:

$$Y_{CO} = M_H + t_H + l_{PSPMT} \quad (7)$$

where  $M_H$  is the averaged value of the vertical mark given in Table 1 for the  $\gamma$ -camera housing,  $t_H$  is the thickness of the housing, its value being  $(10.0 \pm 0.2)$  mm, and  $l_{PSPMT}$  is the semi-length of the  $\gamma$  camera determined by the PSPMT size, its value being  $(52.00 \pm 0.15)$  mm. Consequently, the position of the centre in the  $\gamma$  camera referred to the SALSA system of reference becomes  $Y_{CO} = (237.85 \pm 0.35)$  mm for  $S_1$  and  $Y'_{CO} = (237.95 \pm 0.35)$  mm for  $S_2$ . The total uncertainties of these values ( $\sigma_{Y_{CO}}$ ) were evaluated by propagating all the components involved in Eq. (7). Regarding the  $^{22}\text{Na}$  source, the position of its active volume centre is matched to the top of the support structure by construction. Therefore, no further calculation is needed to obtain the Y coordinate of the centre of the source, although this is necessary in the case of its uncertainty. This uncertainty is affected by two factors. The first one is the machining of the support structure, which is made with a precision of  $\pm 0.1$  mm. The second one is the vertical dimension mark measurement  $M_S$  for  $S_1$  and  $M'_S$  for  $S_2$ , whose values are shown in Table 1. Therefore, the Y coordinate of the centre of the  $^{22}\text{Na}$  source is  $Y_{S0} = (238.30 \pm 0.27)$  mm for  $S_1$  and  $Y'_{S0} = Y_{S0}$  for  $S_2$ , whose uncertainties are calculated by propagating the two contributions. When the deviation,  $\delta$ , between the centre of the  $^{22}\text{Na}$  source and the position of the centre in the  $\gamma$  camera is calculated for  $S_1$  and  $S_2$ , it is seen that both values do not differ statistically. Therefore, taking into account that  $Y_{S0} = Y'_{S0}$ ,  $^{22}\text{Na}$  source and  $\gamma$  camera rotates in the XZ plane of the global reference system. This fact avoids further corrections in the position calculation. Regarding the X coordinate, in the  $S_1$  scanning position the uncertainty is purely mechanical, because no level measurements are needed to establish their values with respect to the global reference system. Fig. 5 shows a frontal view of the  $\gamma$  camera and  $^{22}\text{Na}$  source system. The high-precision machining allows the absence of systematic deviation to be assumed. Therefore, according to Fig. 5,  $X_{CO} = X_{S0} = 0$ .

For the X coordinate, there are three sources of uncertainty in the determination of the  $\gamma$  camera centre: The first one corresponds to the uncertainty in the positioning of the housing of the  $\gamma$

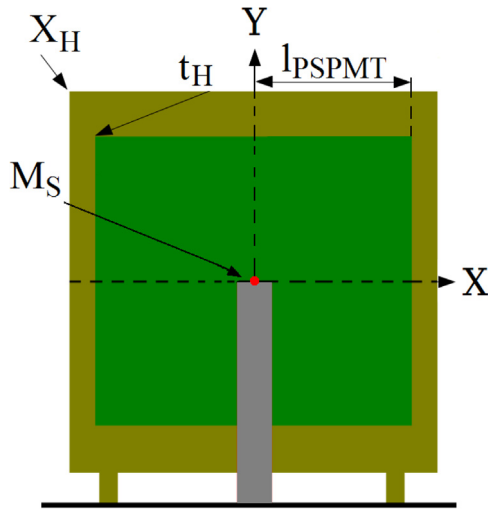


**Fig. 5.** Frontal view of the layout of SALSA mechanics. The brown colour indicates the housing and the green one the  $\gamma$  camera itself, while the red colour is used for the  $^{22}\text{Na}$  source and the grey one for its support. (For interpretation of the references to colour in this figure caption, the reader is referred to the web version of this paper.)

camera in the mechanics. Owing to the high-precision machining, this value is  $\pm 0.2$  mm. The second one comes from the positioning of the four LYSO detectors inside the housing, which is also  $\pm 0.2$  mm. The last one is the semi-length of the PSPMT, with an uncertainty of  $\pm 0.15$  mm given by the manufacturer. By propagation, the uncertainty value for  $X_{CO}$  is  $\pm 0.32$  mm. Therefore, the coordinate of the centre of the  $\gamma$  camera in the global system of reference becomes  $X_{CO} = (0.00 \pm 0.32)$  mm.

Regarding the  $^{22}\text{Na}$  source, the uncertainty in the X coordinate of its centre comes, on the one hand, from the uncertainty of the machining of the support structure, which is  $\pm 0.1$  mm, and, on the other hand, from the uncertainty to position the support structure in the high-precision mechanics, which is  $\pm 0.2$  mm. As a consequence of the uncertainty propagation, the X coordinate of the geometrical centre of the source in the SALSA system is  $X_{SO} = (0.00 \pm 0.22)$  mm.

In the scanning position  $S_2$ , the rigid bar where  $^{22}\text{Na}$  source and  $\gamma$  camera are placed becomes X-axis. Therefore, X becomes Z in the frontal view of Fig. 5. Consequently,  $Z_{CO} = X_{CO}$  and  $Z_{SO} = X_{SO}$  as  $\gamma$  camera and  $^{22}\text{Na}$  source are tightly attached to the rigid bar.

Regarding the third component of  $\gamma$  camera and  $^{22}\text{Na}$  source centres, Z in  $S_1$  and X in  $S_2$ ,  $X'_{CO} = Z_{CO}$  and  $X'_{SO} = Z_{SO}$  because, as said above, both elements are attached to the rigid scanning branch. However, to obtain the precise value of these coordinates it is necessary to take into account that distances between HPGe detector and the elements of the branch are adjusted depending on the size of the detector to be scanned. The distances taken into account in the calculation of  $Z_{SO}$  ( $X'_{SO}$ ) and  $Z_{CO}$  ( $X'_{CO}$ ) are shown in Fig. 6. There are two: the distance  $d$  along Z in  $S_1$  (X in  $S_2$ ) between the centre of the  $^{22}\text{Na}$  source and the centre of our global system

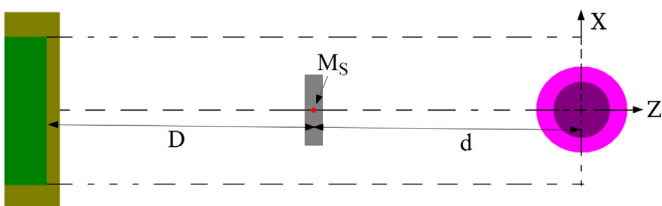


**Fig. 6.** Up view of the layout of SALSA mechanics. The colours to represent the different elements are the same as presented in previous figures. (For interpretation of the references to colour in this figure caption, the reader is referred to the web version of this paper.)

of reference and the distance  $D$  along Z in  $S_1$  (X in  $S_2$ ) between the centre of the  $^{22}\text{Na}$  source and the external surface of the  $\gamma$  camera. Therefore,  $Z_{SO} = d$  and  $Z_{CO} = d + D + w$ , where  $w$  is the distance along Z between the external window surface and the geometrical centre of the  $\gamma$  camera.  $D$  and  $d$  are selected according to the size of the HPGe detector, as mentioned above.

An example is studied in order to show the values, together with their uncertainties, obtained in some relevant cases. One might be the characterization, already performed, of a BEGe detector. In the configuration shown in Fig. 6, a calibrated ruler with 0.5 mm precision was used to determine  $D$  and  $d$  values. The results are  $d = (188.5 \pm 0.5)$  mm and  $D = (188.5 \pm 0.5)$  mm. The quoted uncertainties are obtained by propagating the accuracy of the ruler ( $\pm 0.5$  mm) and the uncertainties both in the machining of the support structure ( $\pm 0.1$  mm) for the  $^{22}\text{Na}$  source and in the machining of the housing ( $\pm 0.2$  mm) for the  $\gamma$  camera. Finally,  $Z_{SO} = (188.5 \pm 0.5)$  mm and  $Z_{CO} = (379.5 \pm 0.7)$  mm, the same values being, respectively, for  $X'_{SO}$  and  $X'_{CO}$  in  $S_2$ .

Now, all the elements of SALSA are referred to a common system of reference and, therefore, any point within these elements can be referred to the global reference system. As a previous step, the points of interest in  $^{22}\text{Na}$  source and  $\gamma$  camera reference system need to be known. This task is explained in the two following sections, also evaluating the intrinsic uncertainty associated with each point.

## 5. The $\beta^+$ annihilation position and its uncertainty

The annihilation position ( $X_S, Y_S, Z_S$ ) is needed to solve Eqs. (4)–(6) and, consequently, to obtain the interaction point ( $X_D, Y_D, Z_D$ ) in the scanned detector. The specific objectives of this section are to reach the best estimation of the annihilation point coordinates for all the  $\gamma$  rays emitted by the source and to estimate the associated uncertainty.

As stated above, the two  $\gamma$  rays from the  $^{22}\text{Na}$  source come from the annihilation of the emitted positron with one surrounding electron. However, prior to this, the positron travels a certain distance through the material. Therefore, the two  $\gamma$ -rays generation point is located at the positron track's end-point. The uncertainty in the determination of its coordinates becomes a degradation factor in the scanning system because these coordinates cannot be known [3]. A Monte Carlo (MC) simulation was performed in order to obtain the spatial distribution of the annihilation points, in which the relevant characteristics of the source were implemented. The statistical distribution corresponding to each coordinate enables us to determine the mean point and the uncertainty of each annihilation coordinate.

The MC simulation was performed using the Geant4 toolkit [14,15]. Its goal is to evaluate the length that the positron coming from the  $^{22}\text{Na}$  decay travels through the source material until it annihilates with one surrounding electron to generate the two collinear  $\gamma$  rays.

A sphere with 0.25 mm diameter of  $^{22}\text{Na}$ , as described in Section 2, with all the processes and decay probabilities inherent to this radionuclide was implemented in the MC code. The annihilation position was recorded event by event, which enables us to know its coordinates ( $X'_S, Y'_S, Z'_S$ ) for each  $\beta^+$  in the reference system of the  $^{22}\text{Na}$  source, obtaining the projection on the XY plane shown in Fig. 7. When representing the probability distribution corresponding to  $X'_S$  coordinate (see Fig. 8) a profile centred at zero was obtained. The same ones were obtained for  $Y'_S$  and  $Z'_S$ , as expected according to the symmetry of the  $^{22}\text{Na}$  source.

In order to calculate the standard deviation of  $X'_S, Y'_S$  and  $Z'_S$  distributions, a numerical calculation was performed by using Mathematica [16]. With this tool, an interpolation was made using

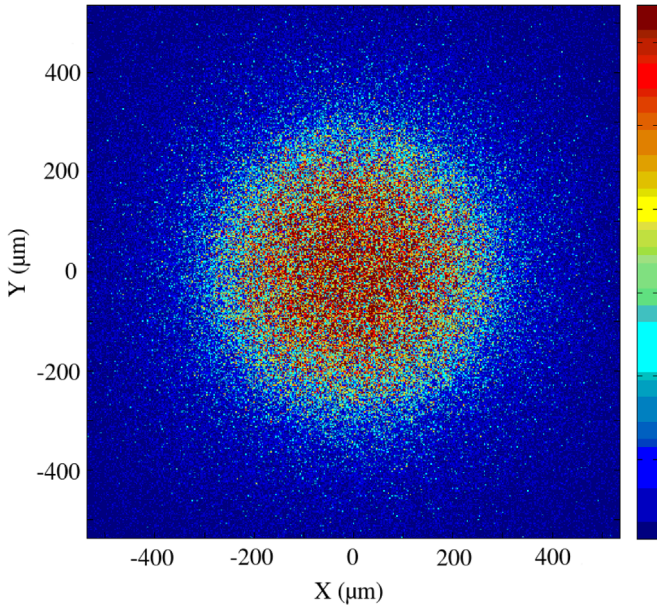


Fig. 7. 2D projection of annihilation position inside the  $^{22}\text{Na}$  source.

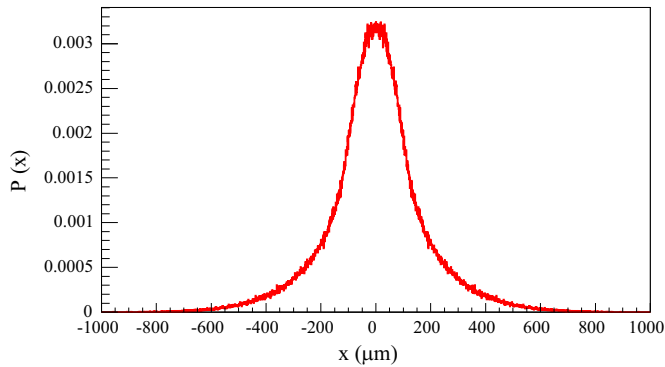


Fig. 8. Histogram of the probability distribution for  $X_S$ . The same one is obtained for  $Y_S$  and  $Z_S$  coordinates.

the statistical distribution data to obtain a functional expression of the probability density,  $P(x)$ , which allowed us to calculate the mean value of  $x$  numerically by the well-known integral definition:

$$\bar{x} = \int_0^\infty xP(x) dx. \quad (8)$$

Its standard deviation was also calculated numerically by using its definition in the descriptive statistics, which has the following formula:

$$\sigma^2 = \int_0^\infty (x - \bar{x})^2 P(x) dx. \quad (9)$$

The results obtained for the probability distributions associated with the coordinates  $(X_S, Y_S, Z_S)$  of the annihilation point are listed

Table 2

Mean ( $\bar{x}$ ) and standard deviation ( $\sigma$ ) values obtained for the coordinates of annihilation point  $X_S, Y_S$  and  $Z_S$ .  $A$  (%) is the relative area comprised in the interval  $\bar{x} \pm \sigma$ .

Coordinate	$\bar{x}$ (mm)	$\sigma$ (mm)	$A$ (%)
$X_S$	0.00	0.19	78.2
$Y_S$	0.00	0.19	77.6
$Z_S$	0.00	0.19	78.1

in Table 2, where the mean is given in the first column, the standard deviation  $\sigma$  in the second one and the percentage area enclosed in the interval  $\bar{x} \pm \sigma$  in the third one.

As observed in Table 2, the best estimation for the annihilation position  $(X_S, Y_S, Z_S)$  is the geometrical centre of the  $^{22}\text{Na}$  source. Therefore, we took  $\sigma_{X_S}'' = \sigma_{Y_S}'' = \sigma_{Z_S}'' = \pm 0.19$  mm as uncertainty in the coordinates  $(X_S'', Y_S'', Z_S'')$ .

Given the non-Gaussian condition of the distribution, the coverage area is 78%. In order to make the result of the uncertainty compatible with the rest of the work presented here, a coverage factor,  $k=1.36$ , is needed to be introduced on the basis of the desired level of confidence of 68%. This coverage factor will allow us to redefine the uncertainty in each coordinate as  $err(\xi_i) = 0.14$  mm, where  $\xi_i$  represents each  $X, Y$  and  $Z$  coordinates. Thus, the annihilation point or  $\gamma$ -ray emission point taken in the calculation of the  $\gamma$ -ray track is  $X_S'' = Y_S'' = Z_S'' = (0.00 \pm 0.14)$  mm.

### 6. The $\gamma$ -camera interaction points and their uncertainty

An interaction point in the  $\gamma$  camera measured during the scanning process,  $(X_L'', Y_L'', Z_L'')$ , is given by the image reconstruction algorithm specifically developed for our  $\gamma$  camera, whose results are shown in a previous work [17]. Actually, the algorithm only determines the components of the plane of the  $\gamma$  camera that faces the  $^{22}\text{Na}$  source, which are  $X_L''$  and  $Y_L''$  in  $S_1$  and  $Z_L''$  and  $Y_L''$  in  $S_2$ , together with their corresponding uncertainties. Although the uncertainty values are estimated event by event, a value of 0.4 mm is taken in this work for estimation purposes. This value was obtained in the work mentioned above. Regarding the third component  $Z_L''$  ( $X_L''$  in  $S_2$ ), no information was obtained from the analysis of the signal measured in the  $\gamma$  camera owing to the reduced thickness of the LYSO crystal. Therefore, a MC simulation was performed with Geant4 to obtain an estimation of the value of this coordinate, together with its uncertainty.

The absorption probability for 511 keV  $\gamma$  rays for the third coordinate versus the  $Z$  coordinate of the interaction position point in the  $\gamma$  camera is shown in Fig. 9. The probability shape is a consequence of the fact that the linear attenuation factor in the LYSO material is  $0.87 \text{ cm}^{-1}$  at 511 keV, which corresponds to a mean free path of 1.15 cm for  $\gamma$  rays at this energy. Accordingly, what is shown in Fig. 9 is a truncated exponential distribution. For this type of distributions the functional expression of the probability density,  $P(x)$ , has been studied in depth in [18,19]. Using it in Eqs. (8) and (9), the mean value for the distribution is  $Z_L'' = (2.31 \pm 1.43)$  mm. This value will be applied to evaluate the total uncertainty in the position determination inside the HPGe crystal. Therefore, the interaction position in  $S_1$  of a particular  $\gamma$  ray in the  $\gamma$  camera plane can be defined as

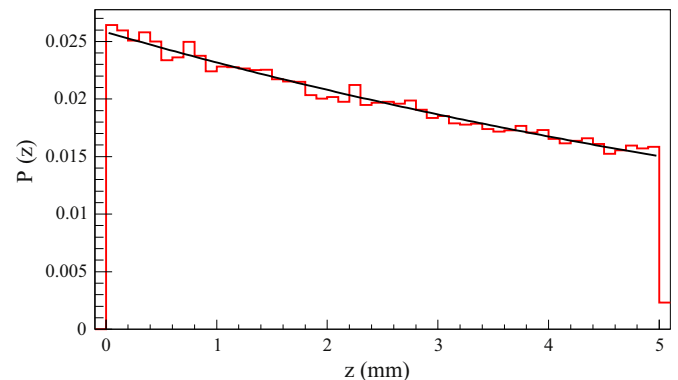


Fig. 9. Histogram of the probability distribution of the absorption position for  $\gamma$  rays along the perpendicular axis in LYSO crystal. In black the exponential fit.

$(X_L'' \pm \sigma_{X_L}'', Y_L'' \pm \sigma_{Y_L}'', Z_L'' \pm \sigma_{Z_L}'')$ , being  $\sigma_{X_L}'' = \sigma_{Y_L}'' \sim \pm 0.4$  mm and  $\sigma_{Z_L}'' = \pm 1.43$  mm in the reference coordinate system centred in the  $\gamma$  camera. The same situation will be seen in  $S_2$ , but in that case  $\sigma_{Z_L}'' = \sigma_{Y_L}'' \sim \pm 0.4$  mm and  $\sigma_{X_L}'' = \pm 1.43$  mm.

## 7. Total uncertainty in SALSA

Once the points needed in the calculation of Eqs. (4)–(6) have been determined in the previous sections and their uncertainties calculated taking into account all the sources of uncertainty, an estimation of the uncertainties corresponding to  $(X_D, Y_D, Z_D)$  can be made. From Eqs. (4)–(6), the uncertainty at a certain point  $(X_D, Y_D, Z_D)$  can be evaluated by doing uncertainty propagation. This uncertainty is affected by the  $\beta^+$  annihilation position in the  $^{22}\text{Na}$  source seen in Section 5, the spatial resolution in the  $\gamma$  camera given in Section 6, and also by the contribution generated by the translation required to transform the reference systems for both elements into the common reference system defined by the SALSA mechanics in Section 4. Accordingly, the calculation of the total uncertainty in  $X_D, Z_D$  and  $Y_D$  can now be done taking into account the uncertainties of all the variables. Regarding the  $Y$  coordinate, the total uncertainty of  $Y_L$  ( $Y$  coordinate of interaction in the  $\gamma$ -camera plane), becomes  $\sigma_{Y_L} = \pm 0.53$  mm after propagation in the translation formula. The total uncertainty of  $Y_S$  ( $Y$  coordinate of the  $^{22}\text{Na}$  source annihilation point) is  $\sigma_{Y_S} = \pm 0.30$  mm.

For the  $X$  ( $Z$  in  $S_2$ ) coordinate, the total uncertainty of  $X_L$  ( $Z_L$  in  $S_2$ ) can be expressed as a propagation of the uncertainty in the position of the centre of the  $\gamma$  camera and its image resolution in this coordinate. Therefore,  $\sigma_{X_L} = \pm 0.51$  mm. For  $X_S$  in  $S_1$  ( $Z_S$  in  $S_2$ ), the uncertainty value  $\sigma_{X_S}$  ( $\sigma_{Z_S}$  in  $S_2$ ) becomes  $\sigma_{X_S} = \pm 0.26$  mm.

With respect to  $Z$  coordinate ( $X$  in  $S_2$ ) the coordinate  $Z_L$  in  $S_1$  ( $X_L$  in  $S_2$ ) of the interaction point has an uncertainty  $\sigma_{Z_L}$  ( $\sigma_{X_L}$ ) of 1.61 mm, obtained after propagating the uncertainty in the position of the centre of the  $\gamma$  camera ( $Z_{Co}$ ) and  $Z_L''$  uncertainties. The  $Z_S$  in  $S_1$  ( $X_S$  in  $S_2$ ) uncertainty of the 511 keV  $\gamma$  emission point is  $\sigma_{Z_S}$  ( $\sigma_{X_S}$  in  $S_2$ ) equal to  $\pm 0.52$  mm, obtained when considering the uncertainty in the position range and in the positioning of the  $^{22}\text{Na}$  source.

Once the uncertainties for all the parameters involved in calculation of the interaction position inside the HPGe crystal had been obtained explicitly in the SALSA reference system, the last step was to perform uncertainty propagation in Eqs. (4)–(6) in order to calculate the total uncertainties for each coordinate. This involves for example to include the uncertainty in the source position even though its position is assumed to be (0,0,0). In this study, the uncertainty propagation was performed for three real cases, corresponding to the three HPGe detector types which SALSA is specifically designed for. The distances  $^{22}\text{Na}$  source–Ge detector ( $d$ ) and Ge detector– $\gamma$  camera ( $d + D$ ) are adjusted depending on the detector size and, therefore, their uncertainties, together with the uncertainty in the estimation of the  $\gamma$  camera interaction point, have a different impact in the HPGe detector interaction point, the objective of SALSA.

The expected spatial resolution inside the HPGe crystal for each coordinate is summarized in Table 3. As expected, total uncertainty is largely driven by the uncertainty in the  $Z$  coordinate ( $X$

in  $S_2$ ), pointing in the direction from HPGe crystal to the  $\gamma$  camera. Therefore, the greater the distance  $D$  with respect to  $d$ , the better the spatial resolution in the position determination in the HPGe crystal. The large detection surface in our  $\gamma$  camera allows us to move it away with respect to the  $^{22}\text{Na}$  source and reduce the distance from the  $^{22}\text{Na}$  source to the HPGe detector ( $d$ ), increasing the spatial resolution of the system.

## 8. Validation of the position determination with SALSA

A test was performed using a conventional Broad Energy HPGe detector, model BEGe 8030 by CANBERRA. A X-ray radiography was taken to this coaxial detector to measure accurately its size, this being 30-mm height and 80-mm diameter. Two scanning setups were used for this purpose: the SALSA scanning table running as explained along this paper (see Fig. 2), this setup being referred to as Imaging mode from now on, and a new setup using the elements of SALSA to calculate interactions positions applying the Compton effect, this one being referred to as Compton mode. The setup corresponding to the Compton mode is made of the  $^{22}\text{Na}$  source described in Section 3, which is collimated with a 50 mm diameter and 50 mm height cylindrical collimator with a 1 mm diameter hole along its central axis. This collimator is positioned by means of a 0.1 mm precision  $XZ$  positioning system on the centre of the detector window. The  $\gamma$  camera is facing the detector on the  $YZ$  plane, as shown in Fig. 10. In both setups, the BEGe detector position is checked with a 1-mm-dot laser. Measurements were acquired in coincidence between  $\gamma$  camera and Ge detector in order to record those events that scatter in the Ge detector and impact afterwards in the  $\gamma$  camera. Together with the readout electronics associated to the  $\gamma$  camera and described in [17], a flash analogue-to-digital converter (FADC) with 12 bits dynamic range and 100 MS/s sampling rate, model SIS3302-ADC, by Struck was used to acquire the digitized BEGe detector pulses in both Imaging and Compton modes. In order to increase the time accuracy, a cubic spline interpolation method was applied to the recorded Ge pulse shapes [20]. FADC sample rates increased from 1 sample each 10 ns to 1 sample per 1 ns by using this mathematical model. The interpolation allows a better time resolution in the validation study presented in this work.

From all the in-coincidence events acquired in the Compton mode, only the ones scattered at  $90^\circ$  in the Ge crystal were selected by making an energy window in the BEGe spectrum at 255.5 keV energy deposited in a  $90^\circ$  scattering of 511 keV photons from  $^{22}\text{Na}$  disintegrations. The 1274.54 keV emission from the  $^{22}\text{Na}$  was not utilized given that there are actually more  $\gamma$  rays that

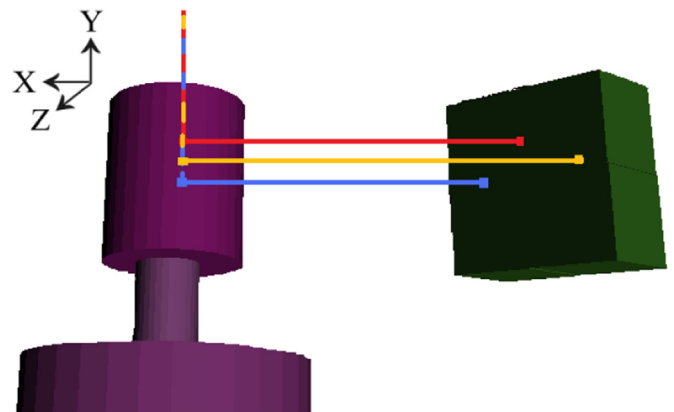


**Fig. 10.** Schematics for SALSA working in Compton mode. The 1-mm-diameter collimated  $^{22}\text{Na}$  source delivers  $\gamma$  rays that are detected in the  $\gamma$  camera after a  $90^\circ$  Compton scattering.

**Table 3**  
Expected spatial resolution for points inside the HPGe crystal.

Detector	$\sigma_{X_D}$ (mm)	$\sigma_{Z_D}$ (mm)	$\sigma_{Y_D}$ (mm)
BEGe	$\pm 1.08$	$\pm 1.08$	$\pm 0.98$
PLANAR	$\pm 0.92$	$\pm 0.92$	$\pm 0.94$
AGATA	$\pm 2.05$	$\pm 2.05$	$\pm 1.84$

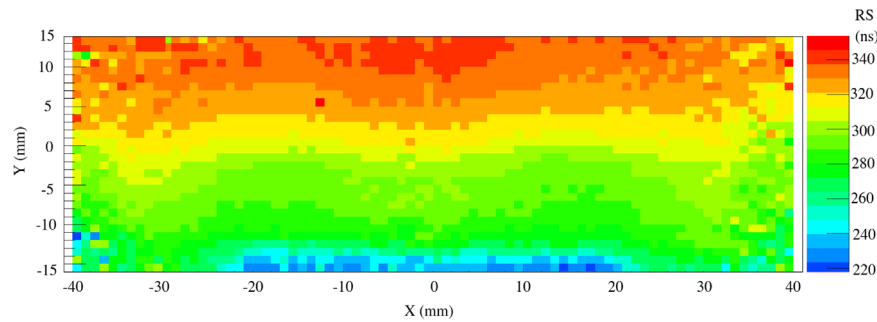


**Fig. 11.** Rise times (RS) of the Ge pulses on the XY projection of the BEGe detector when SALSA works in imaging mode. The rear contact is placed in the  $X=0$  mm,  $Y=-15$  mm position, while the front contact is located along the  $Y=15$  mm line. (For interpretation of the references to colour in this figure caption, the reader is referred to the web version of this paper.)

manage to pass through the collimator and then going to Ge crystal and then to the  $\gamma$ -camera after a Compton scattering than  $\gamma$  rays that pass through the 1 mm collimation hole without interaction with the Pb absorber and then going to Ge crystal and then to the  $\gamma$ -camera after a Compton scattering. For that reason we need to quantify this ratio. With this goal, a Monte Carlo simulation was performed on the basis of the complete setup presented in Fig. 10. In the simulation all the events were tracked in order to know whether they interact with the Pb absorber, with the Ge crystal or with the LYSO crystal. For each event, every interaction position and the deposited energy were recorded. With this information, for 511 keV  $\gamma$ -rays, the simulation has given a result of 59% of the events passing through the collimator hole versus the 41% of the events that manage to pass through the Pb collimator, with and without interaction with the Pb. One conclusion we have got from the simulation is that from the 41% of the events that manage to pass through the Pb collimator, only the ones having a Compton scattering and depositing low energy will disturb our experimental results given that the ones depositing high energy will have bigger Compton angle and the vertical coordinate between  $\gamma$ -camera and Ge crystal will be incoherent. In the case of the  $\gamma$ -rays passing without interaction through the Pb and then having a  $90^\circ$  Compton scattering, the ones that will enter in our energy gate, the situation of the vertical coordinate will be incoherent as well. Therefore, we can reject these events in our analysis increasing our ratio of good events, the ones that has a  $90^\circ$  Compton scattering in the Ge crystal and then travel to the  $\gamma$ -camera, versus the ones that have the same sequence but after a Compton scattering in the Pb collimator, from 59% up to 77% for 511 keV  $\gamma$  rays. For this emission, the energy resolution of our BEGe detector at that energy is 0.81 keV. However, the energy window width is chosen to include events at  $(90 \pm 1)^\circ$  Compton angles in order to get a balance between statistics and reliability. This interval totally comprises the BEGe energy resolution and the uncertainty in the incident photon direction, which comes from the uncertainty in the collimated emission position, the beam divergence resulting from the finite collimator dimensions and the uncertainty in the location of the centre of the detector. Thereby, the energy gate used in the Ge spectrum corresponds to  $\Delta_{511} = 255.5^{+2.2}_{-2.3}$  keV. After the energy gating, data were refined by selecting those events that occurred within the condition of fold-1, i.e., that only one interaction occurred in the Ge crystal. This selection is based on the Pulse Shape Analysis (PSA) of each pulse [21].

The interaction position in the Ge crystal of a particular event was obtained in the Compton mode from the mechanical collimated position of the  $^{22}\text{Na}$  source placed on the plane of the Ge window, which corresponds to the X and Z coordinates as shown in Fig. 10. The interaction point of the  $90^\circ$  scattered  $\gamma$  ray in the  $\gamma$  camera provided the Y coordinate. Thereby, the Compton mode

enabled for determining the Ge interaction position in an alternative way to SALSA and, consequently, provided a suitable validation of the SALSA position determination. In order to proceed with this validation, a comparison between the results obtained with both setups was performed. Specifically, electrical pulses from the BEGe detector corresponding to  $\gamma$  rays interacting within a 2-mm-diameter and 3-cm-long cylindrical column going from the bottom to the top of the Ge crystal and centred on its main axis were taken into account in the comparison. The selection was carried out by taking the positions provided by the PSD in the imaging mode. Actually, the volume of the crystal illuminated in the Compton mode when placing the collimated  $^{22}\text{Na}$  source on the detector window, right in the central position of the crystal, is a cone of 1 mm diameter at the top and 2.2 mm at the bottom where the thick semi-punctual crystal contact is located. But, this cone is almost totally contained within the cylinder, except in the contact zone where the recovered pulses were absent.

Rise times of the Ge pulses obtained from the scanning with SALSA in imaging mode were directly associated to positions in the  $\gamma$  camera. The projection of the BEGe crystal on the XY plane of the PSD in the  $S_1$  scanning position is shown in Fig. 11, where rise times corresponding to each position are given by means of a colour scale. Rise time increases when moving away from the rear contact as seen in Fig. 11. Therefore, it is more influenced by the Y coordinate of the interaction position. The accurate positioning of the BEGe detector was also checked through Fig. 11.

Ninety four pulses of the whole set acquired with SALSA in imaging mode came from the central 2-mm-diameter column of the HPGe crystal, as given by the PSD, their corresponding interaction position coordinates being calculated with the SALSA algorithm described in Section 3. Their shapes, which were also available for the comparison together with the calculated interaction positions, are shown in Fig. 12. In total 13 pulses in turn were available from the Compton mode for the comparison as

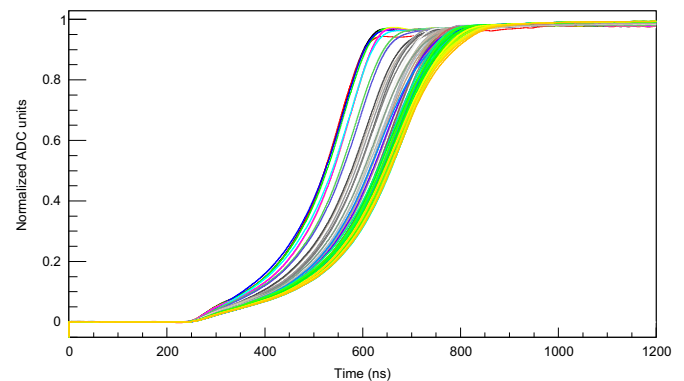


**Fig. 12.** Electrical pulses from the central column in the BEGe detector when SALSA works in imaging mode.

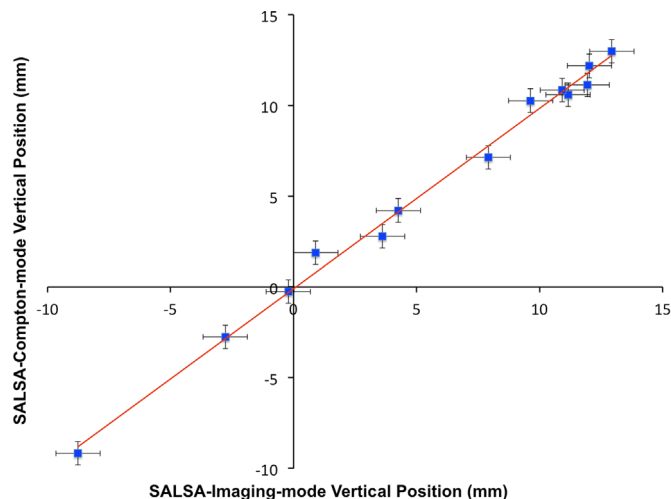


**Fig. 13.** Comparison between SALSAs (imaging mode) and Compton-mode Y positions. The vertical Y coordinate obtained in imaging mode is represented in the X-axis versus the vertical Y coordinate in Compton mode (Y-axis). (For interpretation of the references to colour in this figure caption, the reader is referred to the web version of this paper.)

placed by setup construction into the 2-mm-diameter imaginary cylinder. A statistical comparison was performed between the two set of pulses. But, previously, all the pulses were aligned on an event-by-event basis at 10% of their maximum amplitude ( $t_{10}$ ), as the FADC cards and the  $\gamma$  camera readout electronics did not have a global clock, and just the pulse data from  $t_{10}$  to  $t_{90}$  was kept. Then, each Compton pulse was compared in terms of shape with all the SALSAs pulses, making a pair with the most similar one. The ROOT's Chi2Test method [22] was employed for this task. The matching of the vertical Y coordinates of each pair of pulses obtained from the  $\chi^2$  comparison is shown in Fig. 13, where the reconstructed Y coordinate from SALSAs is plotted versus the corresponding one in the Compton mode. Uncertainties are also represented for each point by means of error bars, SALSAs uncertainties being estimated as explained above and Compton-mode uncertainties being determined from the uncertainty in the position determination with the  $\gamma$  camera. A red line is drawn in Fig. 13 representing the ideal behaviour. It is worth to remark that all the uncertainties embraced the fitted line. This fact tells us the uncertainty estimation to be suitable and, therefore, the assumption to consider negligible the uncertainties introduced by the PSAC algorithm to be proper in the frame of this study. Finally, the mean deviation of the calculated positions was 0.41 mm, while the maximum one corresponds to 0.98 mm, these values being lower than the uncertainty estimated for the Y coordinate with SALSAs, which means the Y coordinate calculated with the SALSAs algorithm do not differ from the reference one.

## 9. Conclusion

The expected spatial resolution in our scanning system for different types of HPGe detectors has been studied. To accomplish this task, we took into account all the sources of uncertainty present in the determination of the interaction position of the  $\gamma$  ray inside the HPGe crystal. The spatial resolution was approximately 1 mm for Ge-planar and BEGe detectors and around 2 mm for AGATA detector. This improves the accuracy of the current scanning systems by a factor of 2, enhancing the scanning capabilities and allowing the relationship between the  $\gamma$ -ray interaction position and the electrical response in this type of detectors to be explored in detail. The position calculation performed by SALSAs has been checked by using the characterization of a non-segmented HPGe crystal, for which rise time of pulses depend mainly on the Y coordinate. Therefore, the results reveal a proper estimation with SALSAs of the Y positions and their uncertainties. Next studies are planned to fully characterize a segmented Ge detector.

## Acknowledgement

This work has been partially supported by MICINN and Mineco through the Grants FPA2008-06419 and FPA2011-03774 and Consolider CSD2007-00042 by the Government of Spain and from Junta de Castilla y Le3n through excellence Grant GR12.

## References

- [1] S. Akkoyun, et al., Nucl. Instrum. Methods A 668 (2012) 26.
- [2] Official GRETA homepage (<http://greta.lbl.gov>).
- [3] P. Suetens, Fundamentals of Medical Imaging, Cambridge University Press, Cambridge, 2009 (Chapter 5).
- [4] F.C.L. Crespi, et al., Nucl. Instrum. Methods A 593 (2008) 440.
- [5] C. Domingo-Pardo, et al., Nucl. Instrum. Methods A 643 (2011) 79.
- [6] N. Goel, et al., Nucl. Instrum. Methods A 700 (2013) 10.
- [7] M. Doncel, et al., J. Instrum. 10 (2015) P06010.
- [8] Eckert and Ziegler Co. Sources for Medical Imaging. Available online at: ([http://www.ezag.de/zentralkatalog/3\\_sources\\_medical\\_imaging\\_equipment.pdf](http://www.ezag.de/zentralkatalog/3_sources_medical_imaging_equipment.pdf)).
- [9] L. Pídol, et al., IEEE Trans. Nucl. Sci. NS-51 (2006) 1084.
- [10] S. De Benedetti, et al., Phys. Rev. 77 (1950) 205.
- [11] K.L. Erdman, Proc. Phys. Soc. A 68 (1955) 304.
- [12] Available online at: (<http://www.hepcomotion.com/>).
- [13] Douglas C. Montgomery, George C. Runger, Applied Statistics and Probability for Engineers, John Wiley and Sons, Inc., 2003 (Chapter 15).
- [14] S. Agostinelli, et al., Nucl. Instrum. Methods A 506 (2003) 250.
- [15] J. Allison, et al., IEEE Trans. Nucl. Sci. NS-53 (2006) 270.
- [16] Wolfram Mathematica™ 8.
- [17] A. Hernandez-Prieto, B. Quintana, IEEE Trans. Nucl. Sci. NS-60 (2013) 4719.
- [18] W.L. Deemer, D.F. Votaw, Ann. Math. Stat. 26 (1955) 498.
- [19] F.M. Al-Athari, J. Math. Stat. 4 (2008) 284.
- [20] William H. Press, et al., Numerical Recipes: The Art of Scientific Computing, 3rd ed., Cambridge University Press, Cambridge, 2007.
- [21] F.C.L. Crespi, et al., Nucl. Instrum. Methods A 570 (2007) 459.
- [22] Available online at: (<http://root.cern.ch/root/html/TH1.html>).